Enhancement of photocatalytic activity of ZnO:
a structural and morphological design

Ph.D. dissertation

Zoltán Kovács

Supervisors:

Prof.Dr. Klára Hernádi

Dr. Zsolt Pap

Doctoral School of Chemistry

Department of Applied and Environmental Chemistry

Faculty of Science and Informatics

University of Szeged

Szeged

2023

Table of contents

List of abbreviations

ANOVA	Analysis of variance
AOPs	Advanced oxidation processes
BBD	Box–Behnken design
CB	Conduction band
CS	Carbon sphere
DEA	Diethanolamine
DRS	Diffuse reflectance spectroscopy
EtOH	Absolute ethanol
FT-IR	Fourier Transformation Infrared Spectroscopy
FWHM	Full width at half maximum
HPLC	High-Performance Liquid Chromatography
HS	Hollow sphere
MNS	ZnO microspheres synthesized using a precursor mixture of $ZnAc_2$ and $ZnAA_2$
MO	Methyl orange
MQ	Ultrafiltered bidistilled water
MS	ZnO microspheres synthesized using only $ZnAc2$
NS	ZnO nanospheres synthesized using only $ZnAA2$
PDE	Photocatalytic degradation efficiency
PL	Photoluminescence
$r_{(002)/(100)}$	The ratio of intensities of X-ray diffraction peaks (002) and (100)
SEM	Scanning Electron Microscopy
SS	Solid sphere
TEM	Transmission Electron Microscopy
UV	Ultraviolet
VB	Valence band
VIF	Variance inflation factor
Vis	Visible light
XRD	X-ray diffractometry
$ZnAA_2$	Zinc acetylacetonate monohydrate
$ZnAc_2$	Zinc acetate dihydrate

List of figures

List of tables

1. Introduction

As the development of human society is believed to be peaking at the start of the 21st century, it has also realized the consequences or rather the cost of becoming a technological species. This development resulted in improved health, life longevity and technology to utilize energy to produce goods and transform our living for the better. The industrial activities enabling us for such growth also produced and continue to produce harmful effects on the environment in the form of pollution. As such, there is no better time than now to dedicate time, effort and ingenuity to the scope of developing green technologies.

Among the major problems stands out that our natural resources are limited and surprisingly, that includes clean water, so water purification and wastewater treatment are of utmost importance. There are existing water treatment methods, which eliminate a significant portion of water pollutants efficiently. However, the mere presence of some pollutants can be detrimental to life due to they are biologically and/or chemically resistant and toxic. The spectrum of water pollutants is wide with an increasing variety. The elimination of these pollutants requires a more general and non-selective solution. In addition, water purification has no strong financial incentive, so more cost-effective technologies are also required to substitute or function along the existing infrastructure.

Advanced oxidation processes (AOPs) offer a suitable and viable alternative in water treatment applications. One discipline in this field is heterogeneous photocatalysis. This method enables the utilization of sunlight for the excitation of a photocatalyst to generate highly reactive radical species, which can eliminate a wide range of harmful chemicals, organic or inorganic. The main goal of such treatment is the complete mineralization of the pollutants into harmless end products. It is easy to see the potential of heterogenous photocatalysis as an alternative green solution, as it can be solar-powered and non-selective. Nonetheless, it is important to highlight that despite the research field has existed for decades, the application for water treatment still falls behind the efficiency of ordinary water treatment methods. Thus, it is imperative to enhance the photocatalytic activity of existing photocatalysts.

In present Ph.D. dissertation, some possibilities and their limitations are investigated in the case of zinc oxide (ZnO) based photocatalysts, also to identify some key factors, which can indicate better performance.

2. Literature review

2.1. Advanced oxidation processes

Advanced oxidation processes are a class of methods, which involve the removal of organic or inorganic compounds from various media (air, liquid or soil) using processes based on the generation of oxidative radical species. Usually, the generated radicals are hydroxyl radicals ($\cdot OH$), superoxide ($\cdot O_2^-$), ozonide ($\cdot O_3^-$) and peroxides (H_2O_2, O_2^{2-}). The main practical incentive of the AOPs is the high reactivity of the generated radical species. This high reactivity is attributed to their energy-dense and unstable chemical state. Once these radicals are formed, they unselectively react with any other chemical species to self-stabilize. This makes the AOPs particularly useful to eliminate biologically toxic or non-degradable compounds, which otherwise would require an elaborate and selective procedure. Through the formation of these oxidative species and their reaction with organic compounds, the final products are less harmful CO_2, H_2O and inorganic ions. The precursors to these radicals are usually O_2 and H_2O, which are activated with a sufficiently intensive energy source and or a catalyst. The energy used to activate can be chemical, photochemical, electrochemical or photoelectrochemical. It comes as no surprise why AOPs came to be one of the most prominent candidates for green technology, as they can be integrated into solar technology. There are various techniques in AOPs for the generation of reactive radicals as follows:

- Radiolysis
- Photolysis
- Fenton reactions
- Heterogenous photocatalysis

The present work focuses on the application of heterogeneous photocatalysis in water treatment.

2.2. Heterogenous photocatalysis

As the name suggests, heterogenous photocatalysis is an advanced oxidation technique based upon a multiphase system, where the energy source for activation is light and the chemical reactions occur in the presence of a catalyst. This consists of the transformation of the energy of light into chemical energy. Consequently, the aim of the field is the efficient utilization of solar energy to induce or accelerate various chemical reactions, in the present case water treatment.

      The key component of heterogenous photocatalysis is the photocatalyst. This material makes possible the utilization of the energy of light for chemical reactions. To understand the role of a photocatalyst, its internal structure and characteristics should be discussed. The most common photocatalysts are semiconductor-based photocatalysts. The conductivity of solid materials is determined by their electronic structure. The energy levels, which an electron can occupy are well quantified. The bonds between atoms are formed by sharing electrons and forming molecular orbitals, which changes the electronic structure of the individual atoms. In solid materials the individual energy levels of atoms form common energy bands. The band, where the outmost electrons are situated, is called the valence band (VB). At ground state, the electrons populate the VB. Here, the electrons are bound to the nuclei of the individual atom. In the conduction band (CB) the electrons are still bound to atoms, but the energy level of the electrons is high enough to freely move around in the solid from atom to atom. The energy difference between CB and VB is called the band gap, where no electron states are allowed. If the VB overlap with CB, the material becomes a conductor. These materials conduct electricity easily as the electrons have intrinsically enough mobility to change the direction of movement according to an external electric field. In the case of a band gap higher than zero, energy equal to or higher than the band gap energy must be transferred to the electron, to jump to the CB. This state is called the excited state. Based on the possibility of inducing and the stability of an excited state in such materials the solids are classified as conductors, semiconductors and insulators. For semiconductors, the excited state is relatively stable and it can be induced with relative ease, due to the lower band gap compared to insulators. In a consequence of the law of conservation of charge, as the negatively charged electron is transferred to the CB, the absence of the electron in the VB leaves behind an uncompensated positive charge, a so-called electron-hole (h^+). These charges are interacting with each other, forming a quasi-particle, the exciton. Here on, the e^--h^+ pair can participate in different charge transfer reactions or recombine transferring the excess energy to the host solid or emitting it as electromagnetic radiation. As suggested before, the band gap energy can be transferred to the electron in various ways and in the case of the photocatalyst, it is through the absorption of electromagnetic radiation (Figure 1).
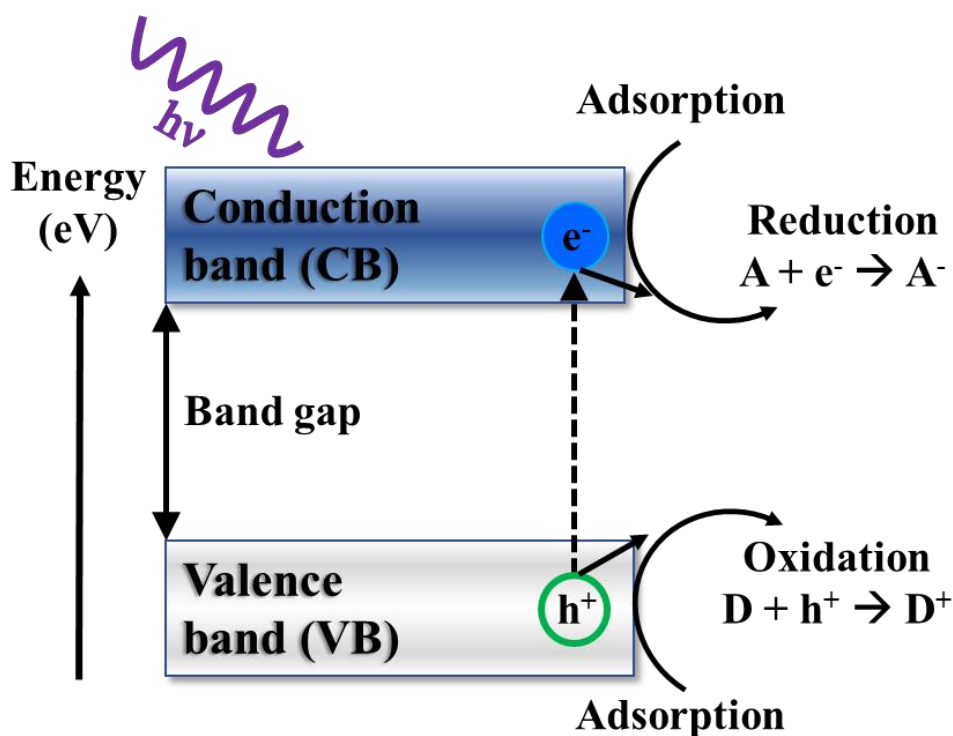
Figure 1 Excitation of the photocatalyst.

If there are electron acceptor (A) and donor (D) molecules on the surface of the excited catalyst and the net activation energy of the reactions is equal to or smaller than the band-gap energy, then initiation of a reaction can occur. This reaction can be summarized as:

$$\text{ZnO} + h\nu \rightarrow \text{ZnO} \ (e^- + h^+) \tag{1}$$

The h is the Planck constant and ν is the frequency of the incident radiation.

The lifetime of an electron-hole pair is short (1 ns to a few hundred ns) [1], so the charge transfer process must occur in a shorter period. The charge transfer reactions are strongly dependent on the adsorbed molecule or atom at the surface. The following possible reaction mechanisms are known for the reactions of the electron-hole pair:

- In the presence of dissolved oxygen, the result is superoxide anions:

$$e^- + O_2 \rightarrow \cdot O_2^- \tag{2}$$

- In presence of water molecules or hydroxide ions, resulting in hydroxyl radicals:

$$h^+ + H_2O \rightarrow \cdot OH + H^+ \tag{3}$$

$$h^+ + OH^- \rightarrow \cdot OH \tag{4}$$

- In the presence of a substrate (e.g. organic molecules), the result depends on the redox characteristics of the substrate:

$$e^- + S \rightarrow \cdot S^- \tag{5}$$

$$h^+ + S \rightarrow \cdot S^+ \tag{6}$$

As mentioned before, the generated radical species can further react to form other radicals or oxidative species [2]:

$$\cdot OH + \cdot OH \rightarrow H_2O_2 \tag{7}$$

$$\cdot O_2^- + H \rightarrow HO_2\cdot \tag{8}$$

$$HO_2\cdot + HO_2\cdot \rightarrow H_2O_2 + O_2 \tag{9}$$

Depending on the material characteristics, the electron can be transferred to a defect state and become "trapped" as a temporary state. It is important to notify that, technically, the utilization of the electron-hole pair for redox reactions is an external pathway of the recombination. Consequently, from an applicative point of view, the actual efficiency of the photocatalytic process is determined by the selectivity of the desired recombination route. This already implies the main aims of research in this field, which are:

- Enhance the light utilization of photocatalysts for electron-hole generation.
- Effective initiation of the charge transfer, rather than recombination.
- Selectivity for the desired reactions.

The mechanism of heterogenous photocatalysis gave rise to a wide variety of applications, which are in continuous expansion and development. They can be used as gas sensors [3–6], for the elimination of NO_x species from the air [7–9], for preparation of self-cleaning and superhydrophilic surfaces [10–14], antimicrobial activity [15–18], for photocatalysis assisted organic synthesis [19,20]. It is important to highlight that the most researched photocatalysts are semiconductors. The expansion of the research field is in direct influence on the other research field related to semiconductors, which represents one of the most basic and important building blocks of modern technology. In consequence, various kinds of research fields are directly influenced by the knowledge obtained through researching photocatalysts such as varistors [21–24], field emission displays [25–28], transparent conducting oxide films [29–31], lasers [32–34], LED [33,35–37], transistors [38–40] and spintronics [41,42]. Heterogenous photocatalysis and the solar energy industry are closely intertwined. One of the most promising applications is the dye-sensitized solar cells, but also conventional solar cells. In these systems, the photogenerated electron migrates to a collector electrode resulting in the generation of electric current [43].

Heterogenous photocatalysis also plays an important role in the development of technologies for the reduction of carbon dioxide, especially considering the 2050 carbon neutrality plan. It is clear to see that the development of the field is necessary not just from environmental protection, and remediation points of view, but for technological advancement itself. The present work is narrowed down to the application of wastewater treatment.

2.3.   Zinc oxide and its photocatalytic applications

First of all, the requirements of a catalyst must be met by a photocatalyst too. Ideally, a catalyst is cheap, easily accessible, chemically inert, selective and should regain its initial physical and chemical state as the catalytic reaction is finalized. As mentioned before, the selectivity in heterogenous photocatalysis can be defined as the selective utilization of the separated charges for the desired chemical reaction, rather than internal recombination. In addition, a photocatalyst should also be biologically inert or at least degradable, non-toxic and photostable. Recently, toxicity and biological inertness are controversial topics in heterogenous photocatalysis, as the method itself is based on the degradation of organic molecules, which are also the main constituents of life. The research on the environmental effects of photocatalysts is still in development [44], but considering the mentioned antibacterial activity, it should be applied with reasonable caution.

In the field of heterogenous photocatalysis, the most researched catalyst so far is TiO_2. In consequence, it is the most widely used reference. Unfortunately, after more than half a century of research, it still falls below the requirements to be feasible in large-scale applications. The recent slow development in the photocatalytic activity of TiO_2 has given rise to interest in alternative oxide semiconductors, such as $BiVO_4$, BiOX (X=Cl, Br, I), Cu_2O, $SrTiO_3$, ZnS, ZnO, to mention a few. In the present work, ZnO and its photocatalytic application for waste water treatment are investigated and will be discussed further in detail.

Zinc oxide is an n-type semiconductor. This means that the charges are transferred via excess electrons. In ZnO, the Zn^{2+} and O^{2-} are in tetrahedral coordination and the bonding is mostly ionic. There is two known crystal structure, the hexagonal wurtzite and the cubic zincblende, corresponding to space groups C6V4 and P63mc (Figure 2). The hexagonal wurtzite structure is more stable under ambient conditions, and it is naturally occurring. A third form also exists, as the hexagonal structure can transform into a rocksalt structure under high-pressure conditions. From a catalytic point of view, the hexagonal wurtzite structure is of interest due to its higher stability and observed activity. It has a relatively large direct band gap of 3.3 eV (equivalent to 375 nm wavelength of radiation), with a relatively large

exciton binding energy of 70 meV. This also makes it possible for long-lived (hundreds of ps) electron-hole pairs to form. Usually, semiconductors' type of conduction can be modified from n to p by doping. In the case of ZnO, this is a controversial topic, as even with or without doping, the material tends to stabilize toward n-type conduction [45]. This can be attributed to oxygen vacancies or non-stoichiometry in the material, as Zn^+ is also can be identified most of the time [46,47]. Due to the polar bonds between Zn and O atoms, the various crystal planes could be electrically charged. Similar wurtzoid structures form crystals with extremely flat surfaces, to minimize the electric inhomogeneity. Yet, in the case of ZnO, it is not completely valid, as some parallel facets tend to have opposite charges. This phenomenon gives rise to the piezoelectric properties of ZnO.
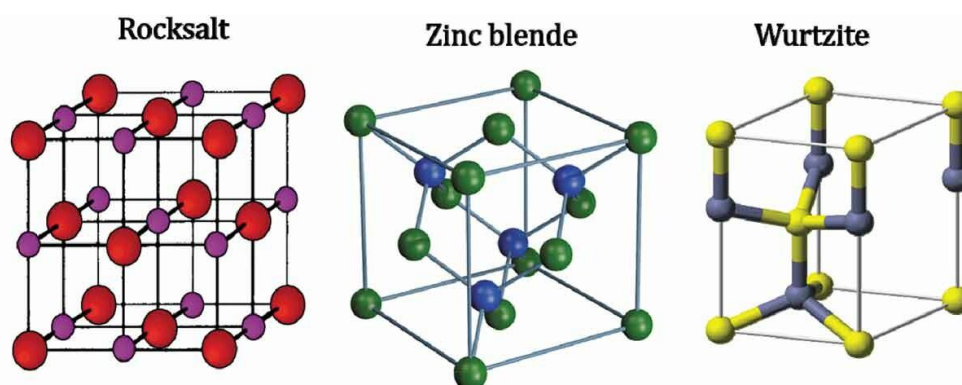
Figure 2 Crystalline structures of ZnO: rocksalt (a), zincblende (b), wurtzite (c) [48].

From the photocatalytic point of view, the hexagonal ZnO attracted great interest as it is highly stable because transformation to other crystal phases does not occur even at high or low temperatures. Visible light activity is also of great interest in the field. Yet, the UV-active photocatalysts have higher performance because of the more stable electron-hole pairs. Although there are prominent results in degrading various harmful chemicals in air and water purification experiments, the quantum efficiency is still low towards degradation. The incident light energy is mostly wasted in the recombination process, so there is still much to improve in effective light utilization.

As mentioned before, ZnO can be used in various applications, but probably its most important field of application is photocatalytic water treatment. Numerous chemicals and pollutants are present and will be present in water due to anthropogenic activity. Some of these chemicals are persistent, bioaccumulative and harmful to the environment and its inhabitants. The presence of these chemicals is the result of the lack of complete understanding of emerging technologies. As industrial development is required for the improvement of the human condition, such effects will most probably remerge. In

consequence, methods like heterogenous photocatalysis are required to be prepared for further deterioration of our environment or even to reform it. Some of these pollutants produce harmful effects even at low concentrations (a few ppm) and can be resistant to conventional municipal wastewater treatments, but by the application of photocatalysis, even these problematic pollutants can be degraded [47,49–51]. The degradation of the various pollutants depends on various factors, such as type, concentration and structure of the photocatalyst, pH of the solution, type and intensity of the light source, structure and concentration of the pollutants and the presence of impurities in the water. There are extensive publications in which zinc oxide was applied for the degradation of various chemicals and pollutants and showed remarkable results: phenols [50,52–55], organic dyes [51,56–59], pesticides and herbicides [50,60,61] and pharmaceuticals [62–66].

Phenols are common chemicals in the aquatic environment, but their concentration is increased in the last decades due to industrial activity [67,68]. It is a main precursor for various plastics (e.g. epoxide resins) and adhesives in the dye industry. Some of them are highly toxic and carcinogenic and received higher regulatory attention in the European Union [69]. The separation of phenol from wastewater is a difficult task at low concentrations, due to its poor adsorbing. The degradation of phenol with photocatalysis is taking place by the attack of hydroxyl radicals formed during the photocatalytic process. Its degradation pathway involves the formation of intermediaries (e.g. resorcinol, catechol, hydroquinone), which could be more or less harmful, so total mineralization is necessary.

Organic dyes are of interest in waste-water treatment too as they are regular pollutants emitted by the textile industry. Their complete long-term effects on the environment are not completely understood, but they or their intermediates are inhibiting microbial growth or even carcinogenic. Their monitoring is also convenient in photocatalytic degradation treatment, due to their visible light absorption. The most commonly used dyes\ molecules as model pollutants are: methylene blue [70,71], methyl orange [72,73], and Rhodamine B [74–76].

Another class of pollutants, which are of high interest is pharmaceuticals. Municipal wastewaters contain these chemicals not just because of the pharmaceutical industry. These chemicals are also persistent and are not biodegraded completely when applied in medicine or on animal farms, such as antibiotics and anti-inflammatories (e.g. ciprofloxacin [77] and ibuprofen [63]). In consequence, their lifetime is long enough to produce effects on the environment. The same is also valid for herbicides and pesticides (e.g. monuron [63], diuron

[78] and carbaryl [79]). It is important to make sure that these chemicals, once applied and fulfilled their purpose, do not prolong their effects undesired. Considering that, these industries are in constant development, new pollutants will emerge, for which a more general solution is required, like heterogenous photocatalysis.

In the present work, the photocatalytic degradation of various model pollutants was investigated by applying ZnO as a photocatalyst: two more common, methyl orange and phenol, but also two less frequently investigated, ibuprofen and diuron.

2.4. Strategies for improving the photocatalytic activity

As mentioned before, despite the potential of ZnO and other semiconductors too, there are a lot of shortcomings in terms of efficiency. There are some drawbacks to application. The first is that the catalyst shows its highest activity when it is in suspension, which requires separation, after treatment, to recover it. In a previous work [80] it was demonstrated that the degradation efficiency is reduced in the case of immobilization of ZnO, due to loss of contact surface, but this aspect is not the main focus of the present work. Second, is the weak adsorption of the pollutants, so direct degradation rarely occurs on the surface. The third is the recombination of the electron-hole pair externally by the reformation of water from hydroxyl radicals or internally. It is not unexpected that the research field aims to enhance photocatalytic activity, so the previous drawbacks would be less consequential in the case of immobilization of the catalyst. Most of the previously mentioned problems are extrinsic properties of the catalytic system. The internal recombination of the electron-hole pair is due to the intrinsic property of the semiconductor. Consequently, if this process is improved towards the generation of reactive species, the initial activity of the catalyst will improve, which makes the efficiency losses, due to the previously mentioned aspects, less detrimental to the applications. In the present research, the structural and morphological modification of ZnO and to a lesser extent the preparation of its composite with noble metals are discussed to enhance the activity.

2.4.1. Structural modification

First of all, it has to be clarified that structural modification encompasses a large variety of possible changes applied to a semiconductor. Some modification includes the introduction of foreign atoms or molecules into the crystal structure or onto its surface, such as self-doping, doping with various atoms (e.g. C, N, S [81]), ions (e.g. Cu^{2+} [81], Mn^{2+}, Co^{2+} [82]), surface functionalization with other inorganic compounds [83] or different

organic molecules [84] or preparation of composite materials. For the discussion of composite materials, a separate section is dedicated. All of these modifications have in common that they are not native to the original crystal structure. Because there is still no complete understanding of the functioning of the hexagonal crystal structure of ZnO concerning its photocatalytic activity, the present work discusses the modifications, which are native to ZnO in the following paragraphs.

As mentioned before the main advantage in the case of ZnO is that the wurtzite structure has high stability. Unfortunately, this is also limiting the possibility of only exploiting the features of this structure. First, to understand the possibilities to modify ZnO, the hexagonal crystal structure has to be discussed in detail. The main characteristic is that it has inversion symmetry, meaning the reflection of a crystal relative to any given point does not transform it into itself. This also has in consequence that the unit cell itself is anisotropic or simply put the properties of the crystal can differ depending on the geometric direction. As the crystal is built up from the unit cell, the Zn and O atoms self-organize in three main crystallographic planes (100), (002) and (101) (Figure 3).
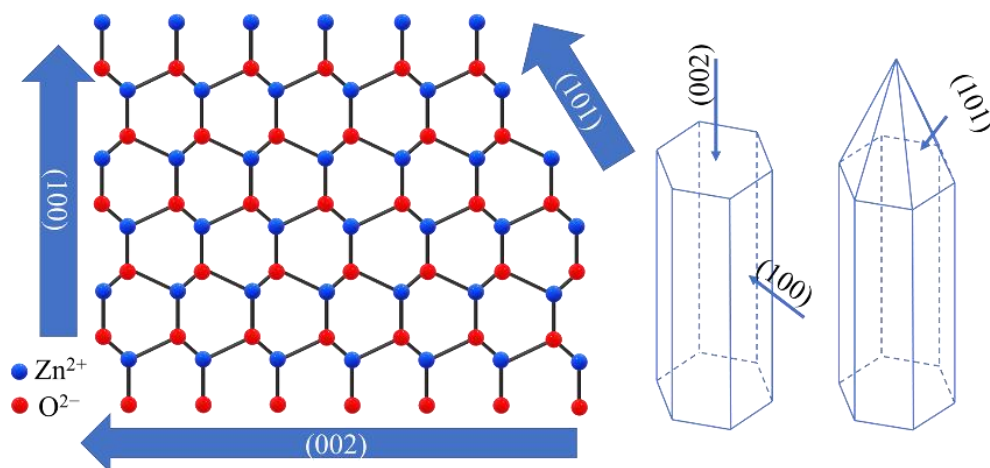
Figure 3 The three main crystallographic planes of the hexagonal wurtzite structure of ZnO.

In crystallography, the ideal crystal is uniform in all directions and in the whole volume. Yet, in reality, this is not possible as the volume of a particle is finite and at the boundaries of the crystal, the atoms are not conjugated by the same number of atoms as in the bulk. In consequence, the terminal atoms of a crystal, situated in the same family of planes, form a crystal's facet. In the case of the ZnO can be observed that depending on the facet, the arrangement of the edge atoms is different. This has a crucial consequence on the polarity of the various facets because the polar bond between O and Zn atoms can create a

local electric field, which if it is coupled on the whole surface a slight but stable electric momentum could form [85]. We can fairly presume that this surface charge could also interact with the separated charges resulting from the activation of the catalyst. The surface of (101) facets consists of relatively smoothly and evenly spaced Zn and O atoms, which results in low polarity on this surface. The surface of (100) facets is formed of Zn-O bonds in a slightly distorted honeycomb structure. In consequence, this plane is alternating in Zn-O dips and ascents. Nonetheless, the unpaired orbitals of a Zn and an O atom between two neighboring ascents are relatively close, which could decrease this electric homogeneity by having lower polarity. Lastly, (002) surfaces are ending in either Zn or O atoms, which have the highest polarity. Theoretically, to conserve the electric neutrality of the crystal, opposite pairs of (002) facets should be Zn and O terminated. This also implies that a flat homogenous (002) facet has strong electric interaction with the hole (if it is O terminated) or electron (if it is Zn terminated). On the contrary, on (100) facets the preferential interaction is more localized depending on the vicinity of the localized surface charge and on (101) the electron and hole pair can move even less preferentially. As mentioned before the electronic structure of a semiconductor determines how can interact with light. The differences in the electronic structure of the facets also result in different light-harvesting capabilities.

So far, the crystal structure was presented in ideal conditions, but one main characteristic of real crystals is defects. These crystal defects usually arise during the formation of the crystal, but they can be introduced by thermal, chemical stress, or photocorrosion by simply using the catalyst [86]. These defects are crucial in catalysis because these atoms (or voids of atoms) are in a higher energy state, they can facilitate reactions much easier. The most prominent example in heterogenous photocatalysis is Ti^{3+} defects, which usually are the main sites where the hydroxyl radical generation is initiated in the case of TiO_2 [87]. The defects can be of the size of an atom or cluster of atoms called point defects but can be larger as line, planar, or bulk defects. Types of point defects are vacancies, adatoms on the surface and interstitials. Zn vacancies are usually scarce for the previously mentioned non-stoichiometry of the material. On the other hand, there are two types of oxygen vacancies, single valent and double valent. O and Zn interstitials are also common defects to the crystal structure, but Zn interstitials are usually discussed as Zn interstitial complexes because of the distortions caused by the excess positive charge from complexes with other defects. Interestingly, the unpaired orbitals for two neighboring Zn atoms at a Zn terminated (002) facet can be considered a double valent oxygen vacancy. As

such, some of these defects can be more native to some facets. The importance of these defects can be expected based on their charge, which can determine how will the electron-hole pair or the generated hydroxyl radical could interact or react with it. [88]

The crystal formation starts with a crystal seed, where the individual component atoms from a precursor agglomerate form cluster of atoms, known as a seed. This is followed by further attachment of new atoms until the bulk atom and surface atom ratio reaches a critical point and starts to self-organize into lower energetic states, corresponding to the crystal structure, which could be followed by further growth. The formation of the hexagonal crystal structure can be observed at a size of a few nanometers [89]. During the crystal growth from the seed, the ratio of surface atoms and bulk is high, which also suggests that a significant portion of the particle's energy is concentrated on the surface. In this period, the crystal is more prone to form defects, due to this unstable, energy dens state.

Based on the polarity of the various facets the growth of the crystal can be influenced by simply facilitating or inhibiting based on the interaction of the polar surface with the reaction media and Zn precursor. If a molecule has a high affinity for polar facets can saturate the surfaces through adsorption, hindering the crystal growth on that surface and vice versa for nonpolar facets. This gives the possibility to design the surface structure of the crystal. Simulations based on density functional theory showed that hydroxyl radical formation is highly favored on (101) facets [90], due to the native single valent oxygen vacancies. Nonetheless, the other facets also could have an important role in the hydroxyl generation process, because on higher polarity facets the water adsorption is more favored, but could also result in the formation of surface zinc hydroxide bond.

The highest coherent volume of a crystal without larger defects is called the crystallite (sometimes also referred to as a grain). This crystal unit can be reproduced by simply translating the unit cell into the boundaries of the particle, without disruption. Controlling the crystal growth also gives the possibility to control the exposed facet composition of the crystal. Various methods are known to synthesize ZnO: sol-gel [53], chemical vapor deposition [91], thermal decomposition [92], wet chemical methods [7], and solvothermal [93], just to name a few. In the present work, solvothermal methods were used, as this method offers efficient control of the parameters of crystallization (temperature and duration of the treatment). Although using these methods various ranges of different facet ratios have been achieved, no general value can be concluded as good for photocatalysis without some controversy. The photocatalytic application also greatly influences whether a

given facet ratio enhance the activity or quite the opposite, because, as mentioned before, the interaction of the target molecule with the facets has to carefully considered. Another explanation could be the randomness in the distribution of facets on the surface. As such, local defects could form small portions of different facets. This is not necessarily means the decreasing the photocatalytic efficiency, because the different properties of the facets could be complementary during the photocatalytic process, perceived as a synergetic effect.

2.4.2. Morphological modification

Morphological modifications are encompassing methods to control the shape and topology of the particles. Theoretically, morphological and structural modification should be separable but are inherently intertwined. Usually, there could be a trade in the formation of surface structure, when the formation of a crystal is controlled to a certain geometry. Nonetheless, it is possible to form agglomerated particles into a certain morphology from smaller crystals, but the contact between the crystallites induces local changes on their surfaces. Morphological changes involve tailoring the size, specific area, porosity, shape, or topological properties of the particles. There are three classes of morphologies such as zero-dimensional (spherical), one-dimensional (wires, rods), two-dimensional (films, layers) and three-dimensional (hollow structures, porous structures), which were extensively investigated in the case of ZnO [94]. The most native morphology for ZnO is rods resembling the unit cell.

As the reactions during photocatalysis are initiated at the boundary of the particle, the surface area of the catalyst is a determining factor for enhancing the activity. Consequently, a higher surface area should result in higher photocatalytic activity, if the other properties of the semiconductor are not modified. Inherently, the size and specific surface area are linked for a given morphology through the square-cube law. Unfortunately, there is a lower limit of stability in size, because as mentioned before at a small crystal size, the energy of the particle is more concentrated at the surface boundary. This leads to lower crystallinity, a higher likelihood of recombination and a tendency to agglomerate to reduce surface tension, so additional stabilization is required [95]. Porosity also increases surface area and adsorption of the model pollutant to the particle. In addition, the light can penetrate deeper into the particle, eventually less likely for the photon energy to escape through reflection. One- and two-dimensional modifications are especially useful if they are coupled with structural control, as vectorial charge transfer can be enhanced along the increased dimension. Thin film ZnO structures are the main components in various electronic and

optical devices, like UV lasers. Their characteristic dimension is thickness. Varying the thickness could lead to different optical properties, like higher transparency and light trapping [96]. This simple morphology also makes it easier to utilize the beneficial effects of preferential orientation.

In the present work, the solid and hollow spherical morphologies of ZnO are discussed more in detail. Solid spherical morphology has the lowest surface-per-volume ratio for a given particle. This leads to a bad economy of the specific surface area at higher diameters. The more concentrated geometry also leads to a more probable stabilization of particles against agglomeration. Even in the case of agglomeration due to the unique geometry gaps will always be present between spheres. Another advantage is that spheres are isotropic, so preferential orientation should not occur [76] (Figure 4). Also, the distribution of various facets could be more homogeneous in the case of ZnO spheres, making light-harvesting properties uniform on the whole surface. This simple morphology also makes it easier to compare various samples based on the only characteristic dimension (diameter). On the other hand, the positively curved surface could lead to a higher loss of light energy in the case of reflection. The preferential growth of ZnO into spheres is difficult to achieve because as soon as the cluster of Zn and O grows sufficiently big to form a crystal the polarities of various facets interact differently. In consequence, various chemicals, called morphological agents, are used to influence the formation of spherical crystals (e.g. surfactants, amines, ethanolamines). As mentioned before smaller spheres (order of a few nms) require stabilization. Larger spheres (in a few micrometers or 100 nm size) are usually formed by the controlled agglomeration of crystallites, which could lead to porous structures.
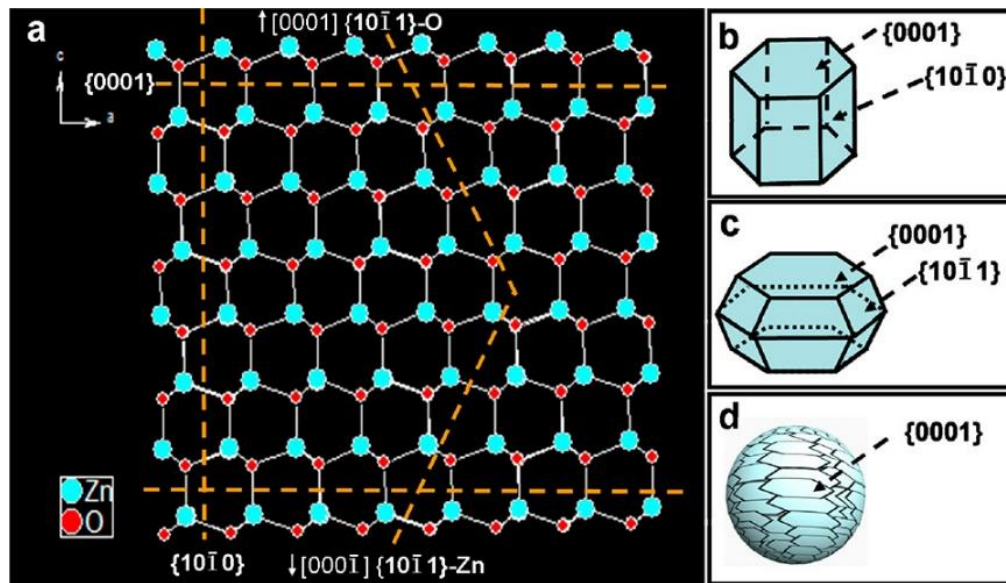
Figure 4 ZnO atomic stacking model, including {0001}, {10$\bar{1}$1}, and {10$\bar{1}$0} facets (a). Schematic illustrations of a ZnO prism (b), a polyhedron (c), and a sphere (d) [76].

Hollow structures resemble their solid counterparts with the interior cavity. This aspect can be also considered as thin film folded into a specific form, which also allows some characterization and phenomena to be implemented in this case too. Consequently, the following advantages can be exploited in the case of hollow structures:

- The hollow structures can have a better specific surface area. As such better photocatalytic performance can be achieved because the actual chemical reactions occur at the solid-liquid interface [97,98].

- In the case of application in suspension, the flotation of the particles can be eased due to the decreased overall density of particles, because of the closed cavity [99].

- In the literature was highlighted that the mechanical properties (tensile strength, stiffness, etc.) of hollow structures are comparable to their solid counterparts [100].

- Due to the increased photocatalytic efficiency to mass ratio, it is also economically more appealing [101–103].

- As the light waves are reflected inside the cavity, constructive interference can enhance the light-harvesting capabilities of the catalyst [104].

Generally, a hollow morphology can be achieved by the application of a template, which can later be removed through calcination [105]. In recent years, the carbonaceous spheres have become popular templates, due to their facile preparation from simple materials

25

like glucose or fructose [106]. These carbon spheres (CSs) are derived by the sequential reduction of the carbohydrate, which can be achieved with a simple solvothermal treatment. In a few publications, where carbon spheres were applied to prepare hollow structured ZnOs [107–109], it was established that the formation of the ZnO layer is due to the polar-polar interaction of the functional groups (-OH, =O, -COOH) and the Zn ions. These functional groups are usually on the surface and originate from the incomplete reduction of the carbohydrates, as CSs grow [107]. This simplicity and the mechanism of formation imply that these templates could be prepared from other more complex carbohydrates too. Such an example was made in previous research, where hollow TiO_2 spheres were synthesized using CS templates, which were prepared from ordinary table sugar (sucrose). This mad the method even more low-cost and accessible and in addition also made it possible to improve the catalytic efficiency [104] (Figure 5). To the best of our knowledge, such types of CSs were not applied to prepare ZnO hollow spheres (ZnO-HSs). Hence, the present study aims to evaluate the applicability of sucrose-derived CSs in the hope to achieve an increase in the photocatalytic activity of hollow structures compared to solid counterparts.
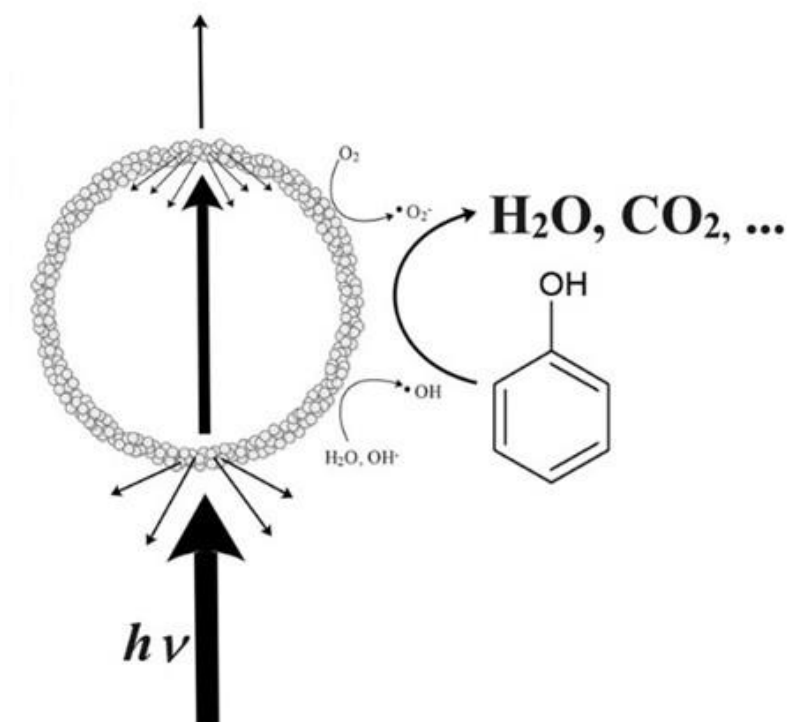
Figure 5 Schematic representation of the enhanced light harvesting of hollow spherical structures [44].

2.4.3. Noble metal deposition

Another way to extend the excitability range and photocatalytic efficiency of ZnO is the preparation of composite materials with ZnO. To enhance the activity through composite formation the individual characteristics of the component materials, respective their possible interactions should be evaluated. A possibility is to prepare composites with other semiconductors, with complementary excitability range in the visible (e.g. Bi_2WO_6 [74], bismuth oxyhalides [79]). In composite materials, because of the contact between the materials, the electron and hole from one sample can interact with the electronic states in the component material or even with the other electron-hole pair [110]. This addition of material could also increase the specific surface area if the added has a higher value, which inherently could improve the activity. A careful design is required to enhance the catalytic activity, because in some cases the electronic interaction between the two phases can result in "short-circuiting" the charge separation process, before its utilization for the degradation of model pollutants [111].

Metals are conductors, which could be complementary property to semiconductors, to stabilize and prolong the lifetime of electron-hole pairs. The deposition of noble metals can greatly enhance the photocatalytic activity of ZnO [112,113]. The most common metals used are noble metals such as Ag [114], Au [113], Pd [115], and Pt [116]. The photogenerated electrons can be transferred to the metal phase, which can stabilize the charge separation and hinder the recombination of the electron-hole pair [117]. To exploit this beneficial effect of noble metal deposition, the preparation of noble metal/semiconductor composite has become a common strategy to enhance the catalytic activity of ZnO [117,118]. The magnitude of the enhancement is greatly dependent on the characteristics of the metal (e.g. crystallite size, and morphology) [73]. The introduction of noble metals can also introduce new energy levels in the material (if it is in the semiconductor structure) or at or near contact boundaries. The fraction and distribution of the metal phase in metal/semiconductors are also key aspects to consider. As mentioned, the metal particles prolong the lifetime of the separated charges. On the other hand, the high mobility of the electrons in the metal phase could also lead to a higher recombination rate, because it could facilitate the electron transfer between defects states internally rather externally. The available literature data suggest that improving the catalytic activity can be achieved with 1 %wt or less metal concentration [81,111,112,119].

To sum up, the noble metal deposition could have the following effects on photocatalytic activity:

- hinder the recombination of charge carriers, through affinity towards electron conduction
- increase the surface area (thus increasing the number of active sites capable of initiating charge separation)
- reduce its band gap by introducing new states depending on the type of metal doping
- modify its surface properties

However, the photocatalytic applications of hollow structures in these composites are scarce. Thus, both aspects were studied in my dissertation (hollow spherical morphology and the effect of noble metal deposition).

3. Aims of the thesis

The present research was initiated in the Research Group of Environmental Chemistry, with the supervision of Prof. Klára Hernádi and dr. Zsolt Pap. The main focus aligned with the research fields' aims, which are to enhance the photocatalytic activity and applicability of semiconductors in heterogeneous photocatalysis. In the present case the enhancement of the activity of ZnO photocatalysts.

The main trend in the research field is to search for better catalysts by trial and error. Although, this is a straightforward, but inefficient method. Thus, one main goal of the present work is to outline key structural features responsible for the catalytic activity of ZnO, respectively to determine its role in the catalytic activity. Such tasks are laborious, so the present work also proposed to test the applicability of a specific experimental design to determine such relations. To get better control of the parameters solvothermal method was chosen and the photocatalytic activity was investigated with synthesis parameters (composition of the reaction mixture, solvothermal temperature and duration) and indirectly its relation to the structure.

Another approach applied is to enhance catalytic activity through morphological modifications, namely preparing ZnO in solid and hollow spherical morphology through the modification of the previous method. Also, considering wider material requirements of future research, tunability of the spherical morphology in terms of diameter was proposed. In the case of solid spheres, an additional goal was to investigate whether the crystal structure can still be designed, despite the isotropic morphology. The solid spheres could provide the most consequential reference for hollow sphere morphology. In the case of hollow spheres, the goal was to apply an existing method of preparing hollow ZnO spheres using carbon sphere templates in the previously mentioned solvothermal method. By such modification, the structural and morphological control can be investigated in the presence of a template too.

The investigation of the effect of noble metal deposition on ZnO was also set as a goal to further improve the catalytic efficiency of the hollow structures.

I also aim to conduct a thorough investigation to reveal the causal relationship between the observed morpho-structural properties and photocatalytic activities resulting from the application of the various synthesis methods to better understand those phenomena, which are significant in this regard for the subsequent development of future photocatalysts.

4. Experimental part

4.1. Reagents and materials

During the experiments, all materials were used without further purification. For the synthesis of ZnO photocatalysts the following materials were used: zinc acetylacetonate monohydrate (ZnAA$_2$, Zn(C$_5$H$_7$O$_2$)$_2$ · H$_2$O, 99.99%, Alfa Aesar, Germany), zinc acetate dihydrate (ZnAc$_2$, Zn(C$_2$H$_3$O$_2$)$_2$ · 2H$_2$O, 99.98%, VWR International, Hungary), zinc chloride (ZnCl$_2$, >99%, Alfa Aesar, Germany), diethanolamine (DEA, C$_4$H$_{11}$NO$_2$, 99.95%, Alfa Aesar, Germany), absolute ethanol (EtOH, 99.99%, VWR International, Hungary) and ultrafiltered bidistilled water *Millipore Milli-Q* (MQ, conductivity 65.9 - 77.0 µS/cm).

For the preparation of carbon sphere templates table sugar (sucrose, Magyar Cukor Zrt., Koronás^{TM}) and MQ water were used. For the purification of the CS templates, acetone (99.99%, Molar Chemicals, Hungary) was applied.

For the noble metal deposition, the applied precursors were tetrachloroauric acid (HAuCl$_4$ · 4H$_2$O, Alfa Aesar, Germany) and hexachloroplatinic acid (H$_2$PtCl$_6$, 99.99%, Sigma Aldrich, Germany). For the stabilization and growth of the noble metal particles trisodium citrate (Na$_3$C$_6$H$_5$O$_7$ · 2H$_2$O, >99.0%, Sigma-Aldrich, Germany) was used, and sodium borohydride (NaBH$_4$, ≥96%, Sigma-Aldrich, Germany) was used for their reduction.

Compounds used as model pollutants for photodegradation tests were methyl orange (MO, C$_{14}$H$_{14}$N$_3$NaO$_3$S, 99.99%, VWR International, Hungary) ibuprofen sodium salt (99.99%, Merck KGaA, Germany), diuron (99.99%, Merck KGaA, Germany) and phenol (analytical grade, Spektrum 3D, Hungary).

4.2. Synthesis of ZnO-based photocatalysts

4.2.1. Solvothermal synthesis of ZnO and experimental design [120]

In each experiment for the solvothermal synthesis of ZnO, a reaction mixture was prepared by dissolving a certain amount of ZnAA$_2$ corresponding to a concentration of X$_1$ (0.068, 0.136 and 0.204 mM) in a solvent prepared by mixing MQ water and absolute ethanol corresponding to a certain concentration of ethanol, X$_2$ (30, 60 and 90% v/v). First, the precursor was added to pure ethanol and stirred continuously for 40 min using magnetic stirrers at a speed of 500 rpm to ensure solution homogeneity. Then the corresponding amount of MQ water was added to obtain the desired solvent composition and was stirred for another 20 minutes. This was followed by the transfer of the reaction mixture into a

PTFE-lined autoclave, with a 70% active volume. The mixture was subjected to solvothermal treatment at a temperature of X_3 (90, 140 and 190 °C) with a heating rate of 5°C·min^{-1} for a duration of X_4 (4, 8 and 12 h). In all the cases we obtained a white precipitate, which was washed several times with ethanol and dried for 12 hours at 80 °C. A proposed mechanism for the formation of ZnO from the precursor and solvent mixture is represented in Figure 6.
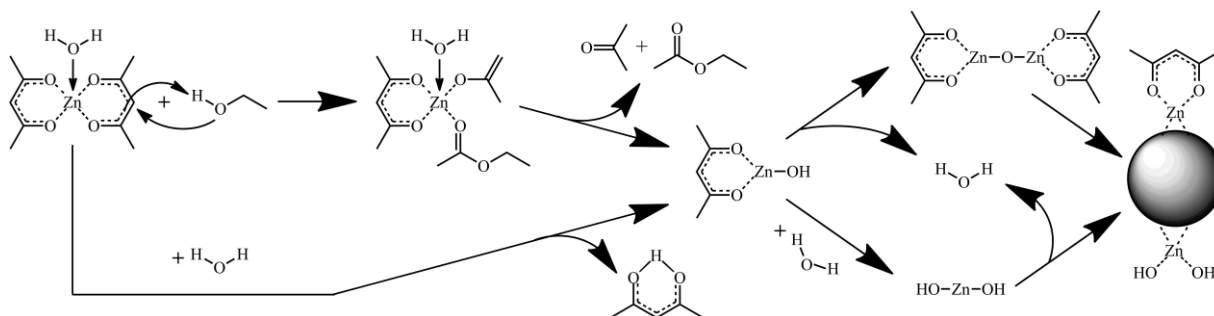
Figure 6 Proposed mechanisms of ZnO formation from zinc acetylacetonate monohydrate.

Box–Behnken design (BBD) with response surface methodology was applied to investigate the influence of 4 major independent variables (molar concentration of the precursor in the reaction mixture, ethanol content of the solvent, temperature, and duration of the crystallization procedure) [72,121–123]. The Box–Behnken design is a second-order technique based on a three-level factorial design (suited for three factors and more), with selected points from a system arrangement [124]. The interaction effects between synthesis variables and their influence on the response (dependent variable) were quantified. Furthermore, the developed prediction model was used to optimize the synthesis conditions for the higher photocatalytic degradation efficiency of the obtained ZnO.

The number of experimental runs required (*NE*) is calculated by equation (10).

$$NE = 2 \times k \times (k - 1) + C \tag{10}$$

In equation (2) the number of factors is k and the central point is C. To improve the stability and adequacy of the model, all factors have been adjusted to three levels: −1 (lower), 0 (medial) and 1 (higher) and the central point of the experimental design (with parameter coordinates: precursor concentration 0.136 M, 60% v/v ethanol-water solvent, 140 °C, 8 h solvothermal treatment) was carried out three times. The chosen factors and their three levels are shown in Table 1 and based on these data, the 27 experimental conditions were specified compared to 81 of a full factorial design. The notation of the synthesized ZnOs is chosen by the value of the levels (−1, 0, 1) and according to the parameter order mentioned in Table 1

(e.g. ZnO 1001 is ZnO synthesized at 190 °C, with a precursor concentration of 0.136 M in 60% ethanol-water mixture, 12 h solvothermal treatment).

Table 1 Variables, levels of variables and constraints used for Box–Behnken design [120].

Factors	Symbol	Levels		
		-1	0	1
Temperature [°C]	X_1	90	140	190
Concentration of the precursor [M]	X_2	0.068	0.136	0.204
Ethanol content of the solvent [% v/v]	X_3	30	60	90
Duration of the solvothermal treatment [h]	X_4	4	8	12

The results were statistically analyzed using Minitab v.17 software. The relationship between the set of independent variables and the response (conversion, crystallinity) was evaluated based on the Box–Behnken design with a full quadratic model expressed as equation (11).

$$Y = b_0 + \sum_{i=1}^{4} b_i X_i + \sum_{i=5}^{8} b_i X_{i-4}^2 + \sum_{i=1}^{i=3} \sum_{j=i+1}^{j=4} b_{ij} X_i X_j + error \qquad (11)$$

Where *Y* is the response (conversion, crystallinity), X_i are the independent variables and b_i (i = 0 to 14), are regression coefficients and the *error* is the error.

ANOVA was applied to evaluate the quality of the model equation. The significance of the model equation was statistically assessed by calculating the p-value (probability value—the probability of obtaining test results at least as extreme as the results observed during the test) with a significance level of 95% (p < 0.05). The model goodness of fit was evaluated by the coefficient of determination (R^2) and the reproducibility of experimental data was determined just by errors. The validation of the model was tested by the generation of new input variables based on the model. To have a better overview of the model, response surfaces and contour plots were also generated.

4.2.2. Solvothermal synthesis of ZnO spheres [125]

Considering the research published by A. Šarić et al. [126] and A. Gómez-Núñez et al. [127], two synthesis strategies were applied: first, to optimize solvent composition to

prepare ZnO photocatalysts with spherical morphology; second, to control various aspects of the morphology (mean diameter, primary particle size).

In each of the experiments, a solution of Zn precursor or precursors and DEA was prepared in an ethanol-water mixture according to 68 mM total Zn precursor and 204 mM DEA concentration as follows: The Zn precursor was dissolved in a corresponding amount of absolute ethanol under continuous stirring for 40 min, then DEA was added in 1:3 molar ratio of Zn to DEA and further stirred for 20 min. The water content was adjusted with MQ water to obtain a certain ethanol-water mixture (ethanol concentration of 80, 90, 95, 99 and 100% v/v), after which the solution was stirred continuously for another 30 min. This was followed by the transfer of the reaction mixture into a PTFE-lined autoclave (V_{fill}/V_{tot} = 70%), which was subjected to a solvothermal treatment at a temperature of 150 °C for 10 h, with a heating rate of 2 °C·min^{-1}. The as-prepared ZnOs were washed 3 times with absolute ethanol and once with a 66–33% ethanol/water solution to purify them from the remaining DEA, then dried at 100 °C for 12 h.

Based on the synthesis procedure mentioned above, the optimal solvent composition was selected that resulted in the best photocatalytic activity and spherical morphology. Then, the effect of various Zn precursor compositions was investigated ($ZnAc_2$:$ZnAA_2$ = 0:100, 5:95, 10:90, 15:85, 20:80, 25:75, 50: 50, 75:25, 100:0 % n/n) together with the temperature of the solvothermal treatment (120, 150 and 180 °C). The 68 mM cumulative concentration of the Zn precursors was constant throughout all experiments. Sample notation was the following: samples synthesized with pure precursors, $ZnAc_2$ and $ZnAA_2$, were named NS (nanospheres) and MS (microspheres), respectively in cases of the precursor mixtures M"percentage of $ZnAc_2$"NS followed by three digits corresponding to the applied solvothermal temperature (example: ZnO synthesized from $ZnAA_2$ at 150 °C is NS150, from a mixture 5% $ZnAc_2$ and 95% $ZnAA_2$ at 180 °C is M5NS180). A full schematic representation of the preparation of ZnO solid spheres is presented in Figure 7.

Zinc precursors C_{ZnAc_2}:C_{ZnAA_2} - 0:100, 100:0, 5:95, 10:90, 15:85, 20:80, 25:75, 50:50
                          and 75:25 → C_{ZnAc_2} + C_{ZnAA_2} = 68 mM
                    T°C - 120, 150, 180
$ZnAc_2$ $ZnAA_2$ $c_{EtOH,final}$ - 80, 90, 95, 99, 100 v/v%

Diethanolamine (**DEA**) H_2O
Zn:DEA = 1:3

EtOH   40 min   20 min   30 min   T°C
                                                      10 h
Stirring   Stirring   Stirring

Drying   Purification
100°C, 12 h

ZnO spheres
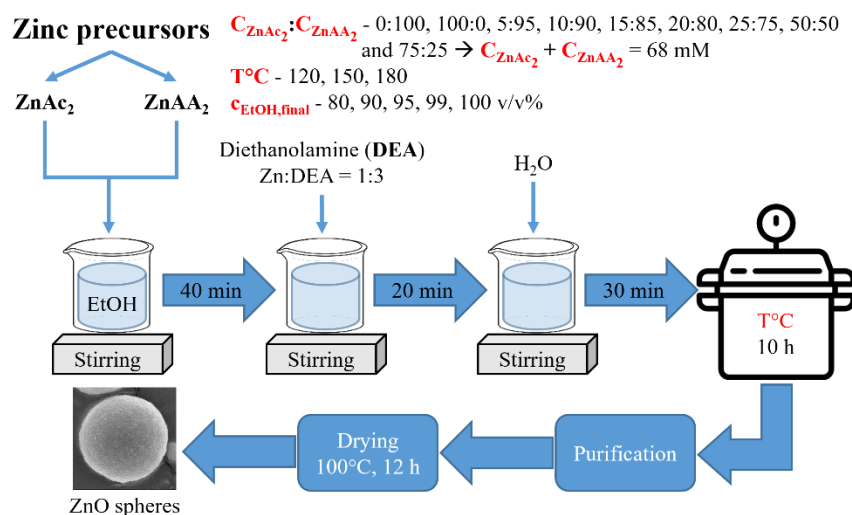
Figure 7 Schematic representation of the synthesis of solid spherical ZnO [93].

4.2.3. Synthesis strategies for the preparation of ZnO HSs [128]

First, the carbon sphere templates were prepared according to Gyulavári T. et al [104] as follows. In a PTFE-lined autoclave, a 0.15 M water-based solution of sucrose was prepared (V_{fill}/V_{total} = 29%) and the pH was set to 12 using a 2 M NaOH solution. The as-prepared solution was subjected to hydrothermal treatment at 180 °C for 12 h. The obtained black precipitate was separated by centrifugation and washed with 100% acetone several times to remove residual organic contaminants formed during synthesis. This was followed by a drying step in air at 40 °C for 24 h. Then, the dark brown product was collected and ground to obtain the CS powder. Further, the CSs were coated with a ZnO shell.

Two synthesis methods were applied to prepare a ZnO coating on the CS templates: chemical impregnation and solvothermal method.

During chemical impregnation, 200 mg of CSs was suspended in 60 mL of 99.3% v/v ethanol under vigorous magnetic stirring, in which 50 mmol of Zn precursor ($ZnAc_2$, $ZnCl_2$, $ZnAA_2$) was dissolved. The mixture was ultrasonicated continuously for 24 h. The aged solution was centrifuged to separate the impregnated CSs, followed by a drying step at 40 °C for 24 h. The as-prepared samples were calcined at 500 °C under continuous airflow to eliminate the CS templates through oxidation, resulting in crystalline ZnO. For this purpose, a Thermolyne 21,100 tube furnace was used applying a 5 °C·min^{-1} heating rate with a constant air supply (30 L·h^{-1}).

Solvothermal synthesis is based on the ZnO nanorod synthesis method with the modifications as follows. 15.5 mmol of Zn precursor and 300 mg of CSs were dissolved in 196 mL of 99.3% v/v ethanol and stirred for 1 h. These values were calculated according to

the theoretical ZnO:CS mass ratio of 12:1. The temperature of the solvothermal treatment is 180 °C and the duration is 12 h. The resulting solid samples were washed three times with 65%, 45%, and 20% v/v ethanol-water mixtures. The materials were then dried, calcined and ground in the same way as described in the previous paragraph. The weight ratio of ZnO to CSs was fine-tuned to obtain regular hollow spheres and the samples with the following ratios were further synthesized 10:1, 9:1, 7.5:1, 6:1, 5:1. A schematic representation of the two synthesis methods is shown in Figure 8.
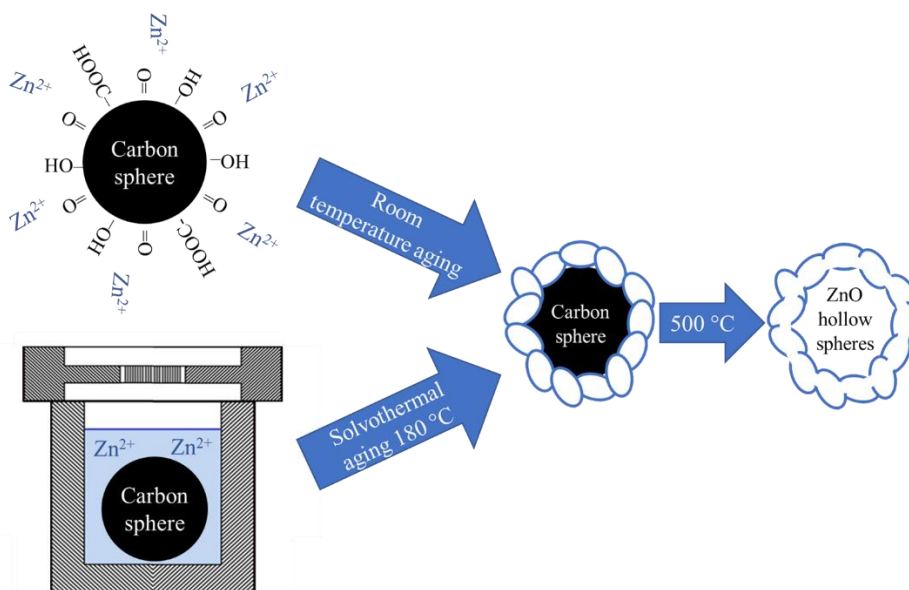
Figure 8 Schematic image of the synthesis strategy applied in this work to prepare ZnO hollow spheres.

A reference material consisting of solid ZnO spheres was also fabricated with average diameters equal to those of the hollow spheres described in the previous paragraphs as follows: a precursor mixture of 20% $ZnAc_2$ and 80% n/n $ZnAA_2$ was dissolved in 99% v/v ethanol-water mixture in 68 mmolar concentration and stirred for 40 min. Diethanolamine was added to the mixture in a 3 to 1 molar ratio of diethanolamine to total zinc precursor and stirred for another 40 min. Later the mixture was transferred to a PTFE-lined autoclave and subjected to solvothermal treatment at 180 °C for 12 h. The purification process was identical to that of the hollow spheres' and it was also calcined in the same conditions.

4.2.4. Noble metal deposition on ZnO HSs

Following the investigation of various ZnO synthesis methods, the one resulting in regular spherical morphology was selected for noble metal deposition. The following

synthesis procedure was applied to deposit 1% wt gold or platinum nanoparticles onto the surfaces of ZnO HSs based on the work of Kovács G. et al [73]: 198 mg of ZnO HSs was suspended in 22 mL of MQ water, to which 1.563 mL of trisodium citrate (0.063 mM) was added under vigorous stirring for 30 min. Then, 0.4 mL of $HAuCl_4 \cdot 4H_2O$ (25.4 mM) or 0.1625 mL of H_2PtCl_6 (31.3 mM) was added to the system. The chemical reduction of noble metal precursors was carried out using 0.5 mL of precooled (T ~ 0 °C) $NaBH_4$ (0.15 M) solution, which was stirred for another 30 min. The as-prepared Au and Pt ZnO HS composites were separated by centrifugation from their suspension, then washed with MQ water three times, dried at 40 °C for 24 h and ground in an agate mortar.

4.3.   Methods and instrumentation

A Rigaku Miniflex II diffractometer was used for X-ray diffraction measurements (XRD). The instrument was operated with Cu-K_α radiation (λ =1.5406 Å) between 20 and 80 2θ°, applying 0.02° steps and 1°·min^{-1} scan speed. Mean primary crystallite sizes were estimated by 3 different methods, that is, the Scherrer equation, the Williamson-Hall analysis (W-H) and the size strain plot (SSP) [129]. Each diffraction peak was fitted with a pseudo-Voigt function type 1 in OriginPro 2018. Other equations were also used as follows:

i.) Correction for instrumental broadening:

$$\beta_{hkl} = [(\beta_{hkl})^2_{Measured} - (\beta_{hkl})^2_{Instrumental}]^{\frac{1}{2}} \tag{12}$$

ii.) Scherrer equation:

$$D = \frac{K\,\lambda_x}{\beta_{hkl}\,cos\theta} \tag{13}$$

iii.) W–H equation:

$$\beta_{hkl}\,cos\theta = \frac{K\lambda_x}{D} + 4\varepsilon\,sin\theta \tag{14}$$

iv.) Size–strain equation:

$$(d_{hkl}\,\beta_{hkl}\,cos\theta)^2 = \frac{K}{D}\left(d_{hkl}^2\,\beta_{hkl}\,cos\theta\right) + \left(\frac{\varepsilon}{2}\right)^2 \tag{15}$$

where β_{hkl} is the full width at half maximum corrected from the instrumental error, θ is the Bragg angle, d is the distance between adjacent planes in the Miller indices (*hkl*) (calculated from the Bragg equation, i.e., $\lambda = 2d\,sin\theta$), D is the mean primary crystallite size, K is the shape factor (0.9) and ε is the crystal strain.

For some samples, the texture coefficient (*TC*) was also calculated using the three main reflections of ZnO corresponding to crystallographic planes (100), (002), (101) and

reference diffraction data available at [130]. The equation used for the calculation of the texture coefficient was the following [131]:

$$TC_{hkl} = \frac{\frac{I_{(hkl)}}{I_{0(hkl)}}}{\frac{1}{N}\sum_N \frac{I_{(hkl)}}{I_{0(hkl)}}} \tag{16}$$

Where TC_{hkl} is the texture coefficient of the (hkl) plane, I is the measured intensity, I_0 is the standard intensity of the corresponding plane and N is the number of reflections considered. TC values are equal to 1 if the structure is close to that of bulk ZnO.

The diffuse reflectance spectra (DRS) of the samples were obtained using a Jasco-V650 UV–Vis spectrophotometer with an integration sphere (ILV-724). The measurements were taken in the wavelength range of 250–800 nm using $BaSO_4$ as the reference. Band-gap energies were calculated by the Kubelka Munk equation and Tauc plot representation. Possible electron transitions were estimated by the first derivative of the DRS. In some cases, the band gap tail energy, also called Urbach energy, was determined according to the publication of P. Norouzzadeh et al [43]. The room-temperature photoluminescence (PL) emission spectra of the samples were recorded at 350 nm excitation wavelength using a Horiba Jobin Yvon Fluoromax-4 type spectrofluorometer and a 350 nm cut-off filter with a spectral window of 1 nm.

The surface of the ZnO samples was studied using Fourier transform infrared spectroscopy (FT-IR) with a Jasco 6000 spectrophotometer in the 400–4000 cm^{-1} range applying 4 cm^{-1} spectral resolution.

Specific surface areas of the catalysts were determined by N_2 adsorption at 77 K, using a BELCAT-A device. The specific surface area was calculated via the BET method.

The morphology of the samples was analyzed by a Hitachi S-4700 Type II scanning electron microscope (SEM) and a FEI TECNAI G2 20 X-Twin type transmission electron microscope (TEM). During SEM measurements the electron beam was produced using a cold field emission gun applying 10 kV acceleration voltage, while in the case of TEM 100 kV was set. The micrographs were further evaluated to determine the diameters and distribution of diameters in the ImageJ software.

4.4.   Assessment of photocatalytic activity

The photocatalytic efficiency of the ZnO samples was evaluated by the decomposition of various model pollutants: methyl orange, Na-ibuprofen, diuron and phenol. For a typical photocatalytic experiment, 100 mL of a solution containing the

pollutant and the catalyst ($C_{catalyst} = 1$ g·L^{-1}) was prepared. The mixture was sonicated in the dark for 10 min to ensure adsorption-desorption equilibrium. The suspension was transferred to Pyrex® glass tube reactor with a thermostatic jacket and 2.5 cm inner diameter. The four-hour measurements were carried out under UV irradiation (6 × 6 W fluorescent lamps, Vilber-Lourmat T-6L UV-A, $\lambda_{max} \approx 365$ nm, emission spectra of the lamps used are in Appendix Figure S1) with a distance between the reactor and lamps 5 cm. During the experiments, constant temperature (25 °C, by circulating water in the thermostatic jacket using an ultrathermostat), magnetic stirring (400 rpm) and the dissolved oxygen concentration (by bubbling with air at 30 L·h^{-1}) were maintained.

The used model pollutants and their concentration, in specific cases, were the following: the samples prepared in section 4.2.1 (ZnO rods) were tested for MO ($C_{0,MO} = 0.1$ mM), in case of solid spheres (section 4.2.2) all samples were measured for phenol ($C_{0,phenol} = 0.3$ mM), in case of ZnO HSs respective their noble metal composites were measured for the degradation of Na-ibuprofen ($C_{0,ibuprofen} = 0.1$ mM), diuron ($C_{0,diuron} = 0.1$ mM) and phenol ($C_{0,phenol} = 0.1$ mM). Sampling from the reaction solutions was taken every 10 min in the first hour for ZnO rods and ZnO SSs, respectively 20 min for ZnO HSs, and in the case of all the samples every 30 min in the next 3 hours.

Quantitative analyses of the MO present in the reaction solution during irradiation were carried out by UV-Vis spectroscopy at absorption maximum of 464 nm (using JASCO-V650 spectrophotometer, using the calibration curve presented in Appendix Figure S2). The concentrations of the other model pollutants were measured with high-performance liquid chromatography (HPLC). The device consisted of a Merck Hitachi L-7100 low-pressure gradient pump equipped with a Merck-Hitachi L-4250 UV–Vis detector ($\lambda_{detection} = 210$ nm for phenol, 214 nm for ibuprofen and 254 nm for diuron). A 50% v/v ethanol-water mixture was used as eluent for phenol and ibuprofen, respectively 70% v/v for diuron. The total organic carbon content was measured at the end of the photocatalytic tests after 4 hours of irradiation. The equipment used was an Analytik Jena N/C® 3100 apparatus with an NDIR detector. The furnace temperature was 800°C and 1.0 mL samples were injected. The measurements were made in triplicate.

In some cases, to investigate the reusability of ZnO samples, the degradation experiments were repeated two or four additional times as follows: the catalyst was separated through centrifugation and washed two times with MQ water, followed by its addition into a freshly prepared model pollutant solution.

5. Results and discussion

5.1.   Solvothermal synthesis of ZnO nanorods and structural tailoring

As mentioned in a previous section (section 3), one of the main goals of the research was to identify key structural features, which could be indicators of the photocatalytic activity of ZnO. Reviewing the literature demonstrates the complexity of how a given catalyst exhibit a photocatalytic activity. Attempts to quantify a relationship between photocatalytic activity with one parameter of ZnO are scarce in the literature because such research would demand a high number of experiments and analysis efforts. In addition, applying a certain model doesn't guarantee success, because of the complexity of the photocatalytic process. The main idea of the present study is that the photocatalytic activity of a semiconductor is mainly determined by its physical, structural, and optical properties. These are the results of the synthesis of the photocatalyst. Consequently, a quantifiable relationship between the synthesis parameters and observed photocatalytic activity should exist, also in the case of other material parameters too. If we optimize these models separately, we could identify possible material properties which mainly determine the activity, by simply observing whether the structural parameters tend to find maximum or minimum in the same way as the photocatalytic activity. Reevaluating the work of X. Liu et al [132], the data available in the X-ray diffractograms are usually overlooked and are simply used to identify crystal phases and calculate the mean primary crystallite size using the Scherrer equation. Yet, several times there is a change in the ratio between the intensities (002) and (100) of ZnO, which are not used for calculating the crystallite size but indicates a change in the structure of the crystal.

5.1.1. Characterization

XRD measurements were carried out to identify the crystal phases of the as-prepared ZnO-s. Some of the diffractograms of the synthesized ZnO samples can be seen in Figure 10. The sample notation is the following: "ZnO" and the coordinates of the parameter levels according to BBD (an example is presented in Figure 9).

Sample code								
T [°C]		C_{ZnAA_2} [M]		C_{EtOH} [% v/v]		t [h]		
Value	Level	Value	Level	Value	Level	Value	Level	
190	1	0.204	1	90	1	12	1	ZnO 1-100
140	0	0.136	0	60	0	8	0	
90	-1	0.068	-1	30	-1	4	-1	

Figure 9 An example of how the samples are coded.

The three main diffraction peaks of ZnO were identified (JCPDS card no.0-3-0888) at scattering angles of 2θ: 31.40, 34.4, 36.3 corresponding to (100), (002), (101) crystallographic planes. Only the hexagonal wurtzite crystal phase (P63mc) was identified, and no impurity phases were observable. Additional X-ray diffractograms can be found in Appendix Figure S3. On the diffractograms, it could be observed that the ratio of the intensities of these peaks differs from sample to sample (a few examples could be found in Figure 10). To investigate a possible relation between the PDE and the ratio of intensities of (002)/(100), ANOVA was applied for the ratio of intensities of (002)/(100) in the function of the input parameters. Mean primary crystallite size was calculated and varies between 30–46 nm for the samples.
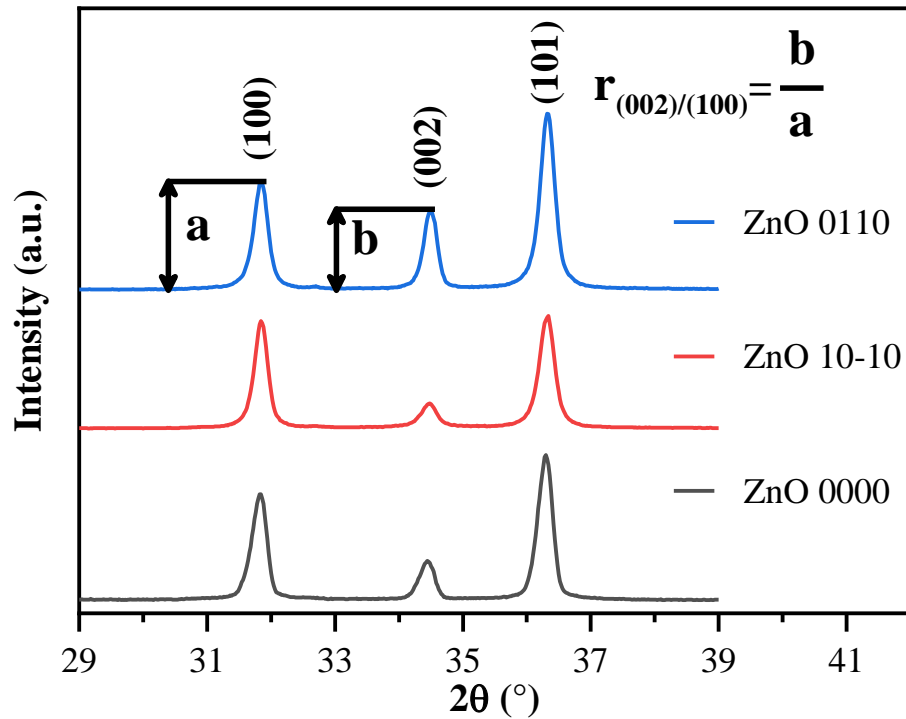
Figure 10 XRD patterns of some representative ZnO samples [120].

The light absorption properties of the ZnO samples were determined by diffuse reflectance spectroscopy and the band-gap values were calculated using Kubelka–Munk transformation and the first-order derivative of the DRS (Figure 11). Due to the slight difference in the band gap values (3.08–3.15 eV using Kubelka–Munk transformation and 3.15–3.24 eV using the first derivative of the spectra) no conclusive trend was observable. These values indicate excitability in the UV-A region of the samples. The DRS, respective of the first-order derivative of DRS is presented in Appendix as Figure S4.
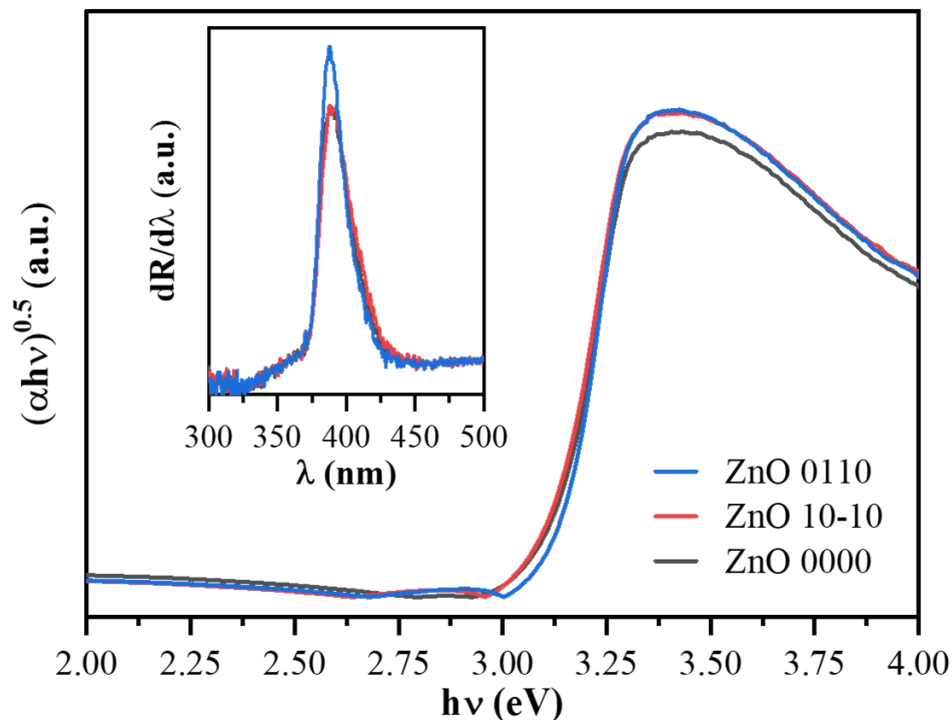
Figure 11 Tauc plot of the DRS of three representative ZnO samples and the first order derivative (inset).

5.1.2. Photocatalytic activity

Following the structural and optical characterization, the photocatalytic activities of the samples were investigated for the photocatalytic degradation of methyl orange. As expected, during photolysis experiments MO decolorization was not significant <1 μM, due to the lamp emission being in the range of 345-409 nm and the photolysis of MO occurs at higher photon energy in aqueous media [133]. During the adsorption period, the change in the concentration of MO did not exceed 2 μM, so the decolorization during the irradiation period is due to the photocatalytic activity of the ZnO phase.

The methyl orange decay curves are presented in Figure 12. The variation of the MO concentration shows strong linearity, as expected [70,134,135]. It is easy to observe that by changing experimental values a change in the photocatalytic activity is observable. To better quantify the photocatalytic activity numerically, which can be used for the mathematical model, photocatalytic degradation efficiency (PDE) was calculated using the following equation:

$$PDE(\%) = \frac{C_0 - C}{C_0} \times 100 \qquad (17)$$

In equation (17) C_0 and C represent the starting, respective final concentration of the model pollutant.
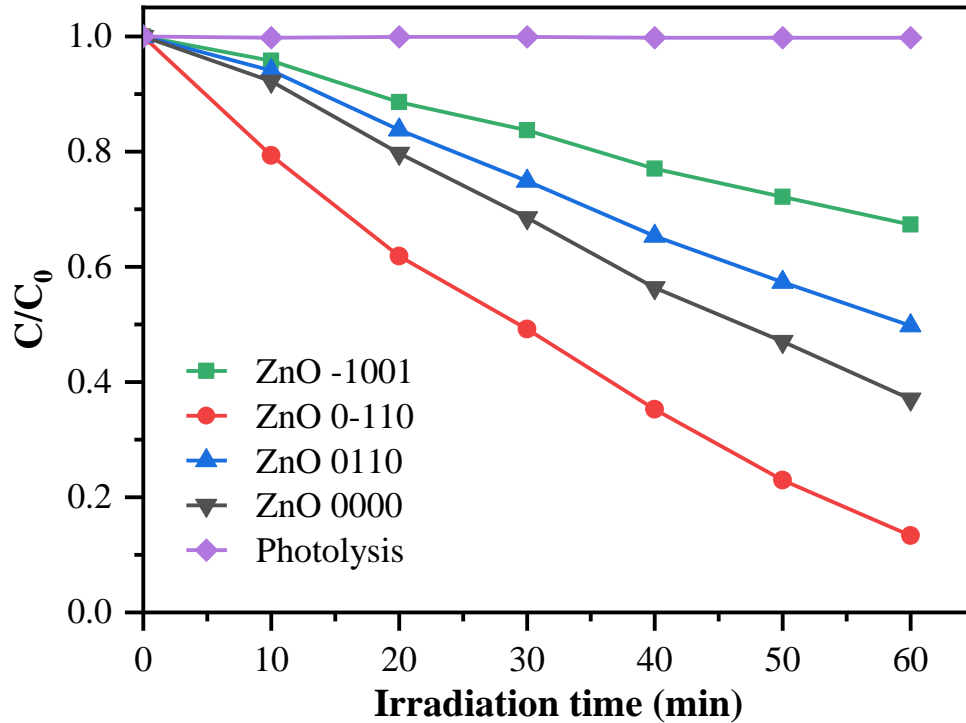
Figure 12 The MO degradation curves of some representative ZnO samples [120].

5.1.3. Model fitting and ANOVA analysis

As mentioned, a fractional factorial design is more convenient because of the lower number of experiments. In the present case, applying BBD resulted in a 66% reduction in experimental runs. The structure of the design results in experiments differing in two parameters, which makes it difficult to elucidate the cause of the difference in activity. As such, the behavior of the fitted model should be used to describe the relationship between the parameters and activity. In general, fractional experimental designs are sensitive to the mathematical behavior of the output. A full quadratic equation was fitted separately for the PDE and ratio of intensities (002)/(100) using ANOVA analysis. The determined correlations are equations (18) and (19) were further used to optimize the synthesis method to maximize the photocatalytic activity of ZnO.

$$PDE\ (\%) = -168.8 + 1.629X_1 + 906.6X_2 + 0.999X_3 + 4.98X_4 - 0.007X_1^2 -$$
$$-1232X_2^2 - 0.006X_3^2 - 0.5951X_4^2 - 1.007X_1X_2 + 0.004X_1X_3 +$$
$$+0.014X_1X_4 - 6.581X_2X_3 - 12.59X_2X_4 + 0.060X_3X_4 \tag{18}$$

$$r_{(002)/(100)} = 0.854 - 0.004X_1 - 1.280X_2 - 0.009X_3 + 0.0107X_4 + 0.000005X_1^2 +$$
$$+8.94X_2^2 + 0.0001X_3^2 - 0.002X_4^2 - 0.0147X_1X_2 + 0.000035X_1X_3 +$$
$$+0.0003X_1X_4 + 0.0014X_2X_3 - 0.008X_2X_4 - 0.00039X_3X_4 \tag{19}$$

In equations (18) and (19), X_1, X_2, X_3, and X_4 are the factors of the following parameters: temperature (°C), the concentration of the precursor (M), ethanol content of the solvent (% v/v) of EtOH and the duration of the solvothermal treatment (h), the output variables are PDE (%, photocatalytic degradation efficiency of MO) and $r_{(002)/(100)}$ (ratio of intensities of diffraction peaks corresponding to (002) and (100) crystallographic planes). A good agreement exists between the predicted and experimental values for both responses, as it is shown in Figure 13.
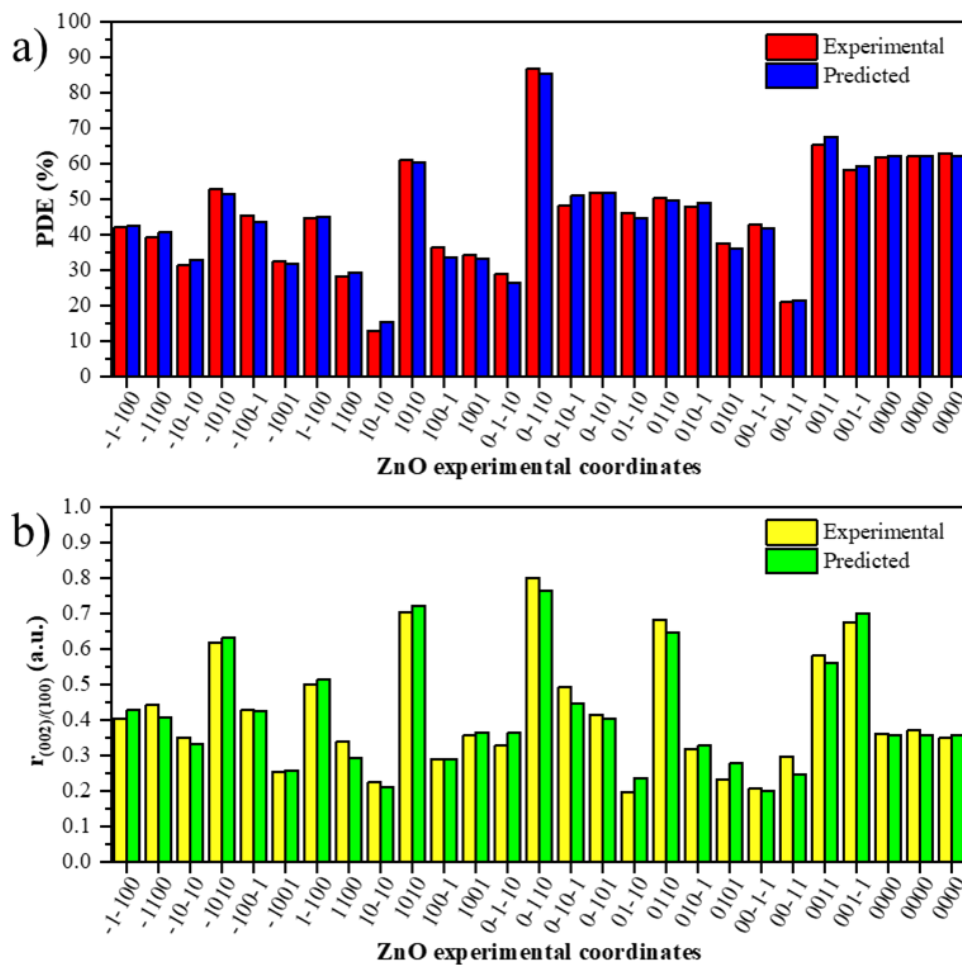
Figure 13 Experimental runs of Box–Behnken design with predicted and experimental values: in case of PDE (a); in case ratio of intensities (002)/(100) (b) [120].

From Figure 13, it becomes obvious that the parameters do show great variance upon the activity and the structural parameter $r_{(002)/(100)}$. Comparing the two output values the variance is also very similar, which indicates a relation between the $r_{(002)/(100)}$ and the photocatalytic activity. The ANOVA results of the ZnO photocatalysts synthesis are shown in Table S1 and Table S2. A full quadratic equation was successfully fitted for both outputs with the low standard deviation values (σ) of 2.15 for PDE and 0.039 for the $r_{(002)/(100)}$. In addition, the validity of the predicted values is well indicated with high R^2 values (0.9913 for PDE and 0.9743 for $r_{(002)/(100)}$) [122]. The ANOVAs resulted in a highly significant p-value ($p < 0.05$) for PDE for all the studied factors, but the significance threshold was exceeded in the case of half of the parameters for the intensity ratio. The variance inflation factor (VIF) is an indicator of whether the predictors are correlated or not. In the present case, VIF values are 1.00 or 1.25, which suggests there is no multicollinearity in the models.

Subsequently, the predictors are stable. Although, the lack of the fits' significance is close to the threshold p-value (0.054 for PDE and 0.059 for $r_{(002)/(100)}$), the difference between the predicted and experimental values suggests that the fit is acceptable. Generally, a thermal process follows an exponential behavior. An exponential function can be approximated by polynomials, but there might be ranges where a simple quadratic equation may not approximate sufficiently. Consequently, the lack of fit can be the result of the exponential behavior of the process [121,136].

In the case of the ratio of intensities (002) and (100) half of the terms show significance (Table S2). For this output the parameters describing the composition of the reaction mixture show significance for almost all related terms. Temperature-related interaction terms also show significance.

The quadratic model fitting was also attempted for the mean primary crystallite size and band gap energy of the samples, but the results showed no conclusive correlation. The relatively narrow range of values for these outputs is probably the source of the high error in the model.

Figure 14 shows residuals in the function of fitted values and Pareto charts of diagnostic plots of the regression with both PDE $r_{(002)/(100)}$ (the normal probability distribution plot is presented in Appendix Figure S5).
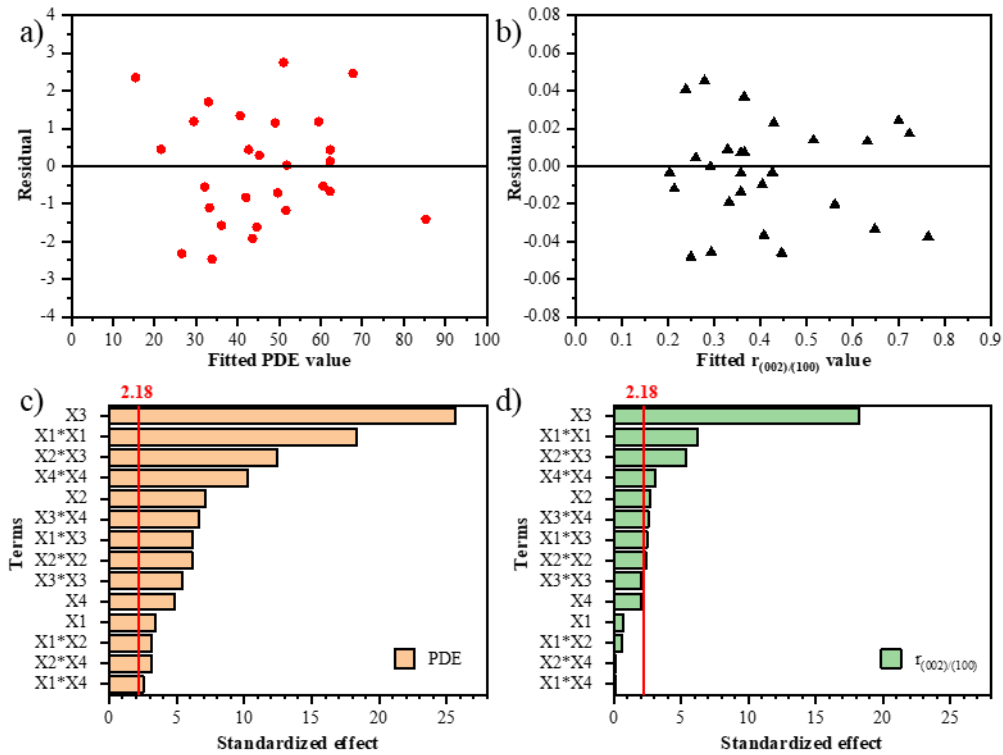
Figure 14 Diagnostic plots of ZnO synthesis results: residual vs. fitted values: for PDE (a); for $r_{(002)/(100)}$ (b); standardized effects of the equation terms for PDE (c); for $r_{(002)/(100)}$ (d) [120].

Generally, the distribution of residuals signifies whether the error in a model is preferentially caused or it is just random noise. In the present case, analysis of residuals shows a random distribution, is independent, without skew. The significance of 3 terms is well revealed in the standardized effects of the equation terms plot (Figure 14), showing the effect on the output in the following order: for PDE $X_3 > X_1^2 > X_2X_3$ and for $r_{(002)/(100)}$ $X_3 > X_3^2 > X_2$. In both equations, the highest impact was produced by the composition of the solvent and the duration of the solvothermal treatment induce only a slight change.

5.1.4. Effect of synthesis factors as surface plots

3-D response surfaces and contour plots were prepared to better visualize the behavior of the two outputs as a function of two parameters. This method enables a graphic evaluation of the effect of two parameters, respective their interaction, while the remaining two are held constant. The hold values were chosen according to the parameter set of the central point (precursor concentration 0.136 M, 60% v/v ethanol-water solvent, 140 °C, 8 h solvothermal treatment). The 3-D and 2-D graphs of the two separate outputs are presented side by side in Figure 15 and Figure 16, to evaluate whether the crystallographic parameter

and the photocatalytic activity could show similar trends or not. Previously, the standardized effects of the various terms in the equations signified that the composition of the reaction mixture (ethanol and precursor concentration) determines predominantly the direction of change both in the PDE and in the $r_{(002)/(100)}$. As can be seen in Figure 15, both outputs increase with ethanol concentration and decrease with the precursor concentration. In addition, it can be observed that the maximum point on the surface plots is achieved at 90 % v/v ethanol and 0.068 M precursor concentration in both cases. Nonetheless, the solvent composition influences greater the outputs.
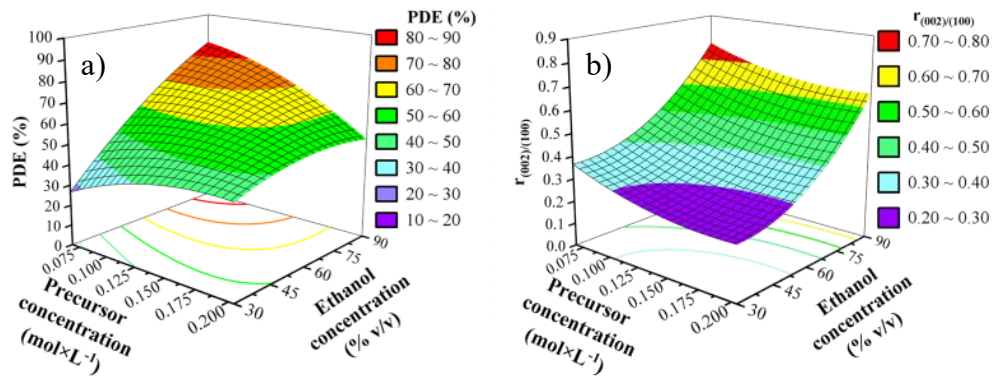
Figure 15 Effect of interaction between precursor concentration (X_2) and ethanol content of the solvent (X_3) on the PDE (a) and $r_{(002)/(100)}$ (b) of ZnO as a 3D response surface. Fixed parameter values: 140 °C, 8 h solvothermal treatment [120].
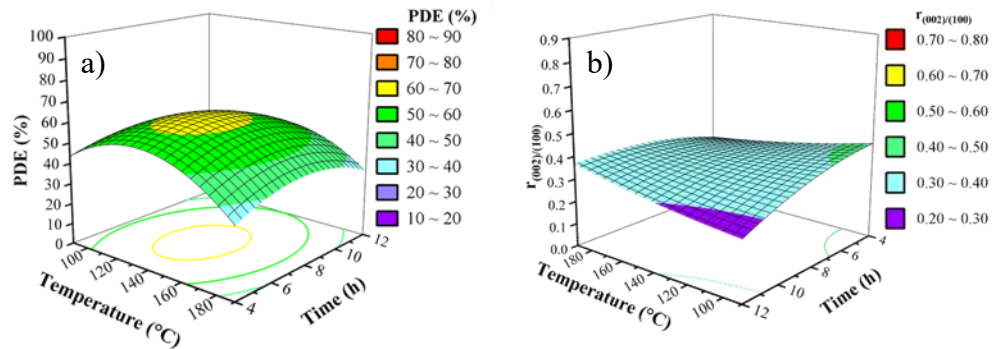
Figure 16 Effect of interaction between temperature (X_1) and duration (X_4) of the solvothermal treatment (a) on the PDE and (b) $r_{(002)/(100)}$ of ZnO as a 3D response surface. Fixed parameter values: precursor concentration 0.136 M, 60% v/v ethanol-water solvent.

Technically, the $r_{(002)/(100)}$ is relative intensity, which also indicates a different ratio of crystallographic facets corresponding to those X-ray diffraction peaks. The photocatalytic activity also shows a similar trend as the relative intensity, which signifies that by controlling

the solvent composition in the synthesis, it could also control the distribution of these facets of the crystal and in parallel, the photocatalytic activity. In the literature, it was already pointed out that a higher photocatalytic activity can be achieved using organic solvents in some specific solvothermal [76] and sol-gel methods [113].

The used precursor (zinc acetylacetonate hydrate) has higher solubility in organic solvents. Also, its reaction with water molecules results in $Zn(OH)_2$, which would hinder photocatalytic activity [137,138]. The higher ethanol concentration prevents the fast reaction of the precursor to form amorphous $Zn(OH)_2$ and can promote the formation of ZnO. On the other half, the precursor concentration is also an influential parameter, due to the same reasons, as the more abundant the precursor in the solution the more increased could be the reaction rate to the products. Consequently, it could be expected that their interaction effect is observable on the response surface, as the change in activity and relative intensity is doubled when the ethanol concentration is changed from 30% to 90%.

The similarity between the trends between the two models breaks when temperature and duration are represented in the function of the outputs (Figure 16). The standardized effects suggested that temperature only produces a significant change in the outputs, in interaction terms and the duration in almost one of the cases, which is well reflected on the 3-D surface plot. This difference can appear because of the small range of change in the output. Nonetheless, this signifies that to achieve the higher photocatalytic activity, the duration of the solvothermal treatment is a less crucial aspect.

5.1.5. Optimization and model validation

As two the validity of the two correlations has been discussed, it is consequential to test, whether these correlations can be applied to new experimental data. Another objective is to achieve higher photocatalytic efficiency. As such, optimization of the model can provide instances for both objectives. In addition, the same optimization was carried out for the relative intensity to further test the correlation between PDE and $r_{(002)/(100)}$.

The optimization was carried out using the Minitab software for both $r_{(002)/(100)}$ and PDE independently, which resulted in new parameter sets, presented in Table 2. The values obtained for a few synthesis parameters already coincide with certain experimental sets used to fit the model. To thoroughly test the stability of the model an additional randomized parameter set has been chosen to avoid reconfirmation of already used data. As could be expected based on the response surface plots, to maximize the outputs, the optimum values

of the ethanol concentration are the highest examined value (90%) and the precursor concentration is at the lowest (0.068 M).

Table 2 The optimization of the ZnO synthesis for optimum photocatalytic degradation efficiency [120].

Sample	Temp.	Precursor Conc.	EtOH Conc.	Duration	Predicted		Experimental	
					PDE	$r_{(002)/(100)}$	PDE	$r_{(002)/(100)}$
	[°C]	[M]	[% v/v]	[h]	[%]	[a.u.]	[%]	[a.u.]
Optimized $r_{(002)/(100)}$ (ZnO-r opt)	190	0.068	90	7.56	74.90	0.873	77.30	0.834
Optimized PDE (ZnO-PDE opt)	155	0.068	90	9.75	88.03	0.766	89.10	0.799
Random-ized (ZnO-rand)	107	0.102	69	9.00	67.18	0.516	69.30	0.534

Interestingly, the optimization resulted in experimental coordinates at the boundary of the examined intervals, which signifies that an even higher value can be achieved outside of the system boundaries. 3-D response surface plots were again used to visualize the region where the optimum was determined, with the hold values of 0.068 M precursor and 90% ethanol (Figure 17), which showed again that duration does not induce a significant change in the outputs. Even though, a different optimum temperature was determined for PDE and $r_{(002)/(100)}$, the observed catalytic activity and relative intensity does not change significantly. The photocatalytic performance of the samples is comparable to a commercial photocatalyst Degussa p25 titanium dioxide (P25), and the activity of the optimized ZnO sample is almost identical to it, as can be seen in Figure 18.
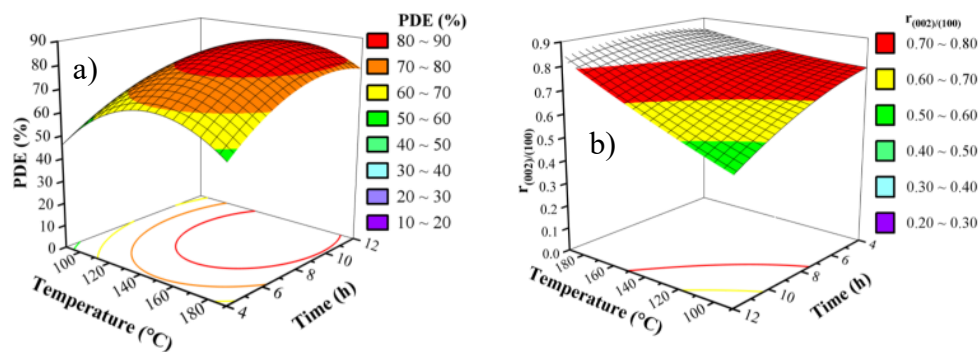
Figure 17 Surface plots of time and temperature of the solvothermal treatment in the optimization region of parameter intervals for the PDE (a) and $r_{(002)/(100)}$ (b). Fixed parameter values: precursor concentration 0.068 M, 90% v/v ethanol-water solvent.
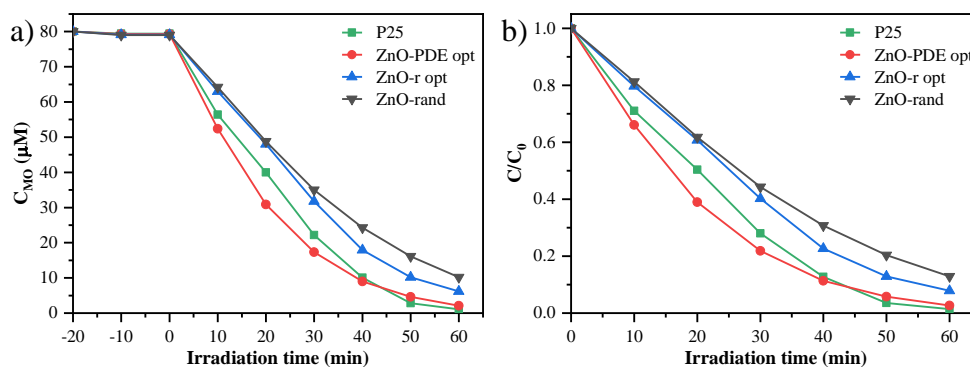
Figure 18 The MO degradation curves of the validation experiments of ZnO [120].

Often, one of the key issues of catalysts is their reusability, which could be especially problematic in the case of ZnO, as it is more prone to photocorrosion and deterioration during use than TiO_2 [139]. The PDE-optimized ZnO (ZnO-PDE opt) was the best-performing catalyst, so it was selected for the reusability test in the degradation experiment. After each experimental cycle, the conversion of methyl orange decreased by 1%. The conversion values of MO are 88% in the first, 87% in the second and 86% in the third cycle), which could be attributed to the loss of material during the collection of the catalyst.

5.1.6. The relation of (002) peak to the photocatalytic activity of ZnO

The influencing of the intensity ratios of various X-ray diffraction peaks in photocatalyst synthesis is a hot topic in the literature. Some publications have already observed a trend in the change of the X-ray diffraction peak, corresponding to (002) planes also showing a similar trend in the catalytic activity. Comparing these publications could lead to some controversy in contrast with the present study, as they observed a trend

opposite, which is discussed before, but these researches aim at a higher ratio of (002)/(100) (>1.2, up to 5 or <0.2) [140]. This structural feature can be explained by an oriented growth along the (002) planes, which is represented in Figure 19. As can be observed, this would lead to a long hexagonal bar-like morphology, if the (002)/(100) ratio is high and hexagonal plates if it is low. The SEM micrographs (Figure 19b and c) of two ZnO samples with different $r_{(002)/(100)}$ and both present the mentioned morphology with no observable difference, but the PDEs have a noticeable difference (~10%). It is also worth mentioning that the preferential orientation, based on the XRD measurements, is at the scale of the primary crystallites and the SEM micrographs show particles with a much bigger size.
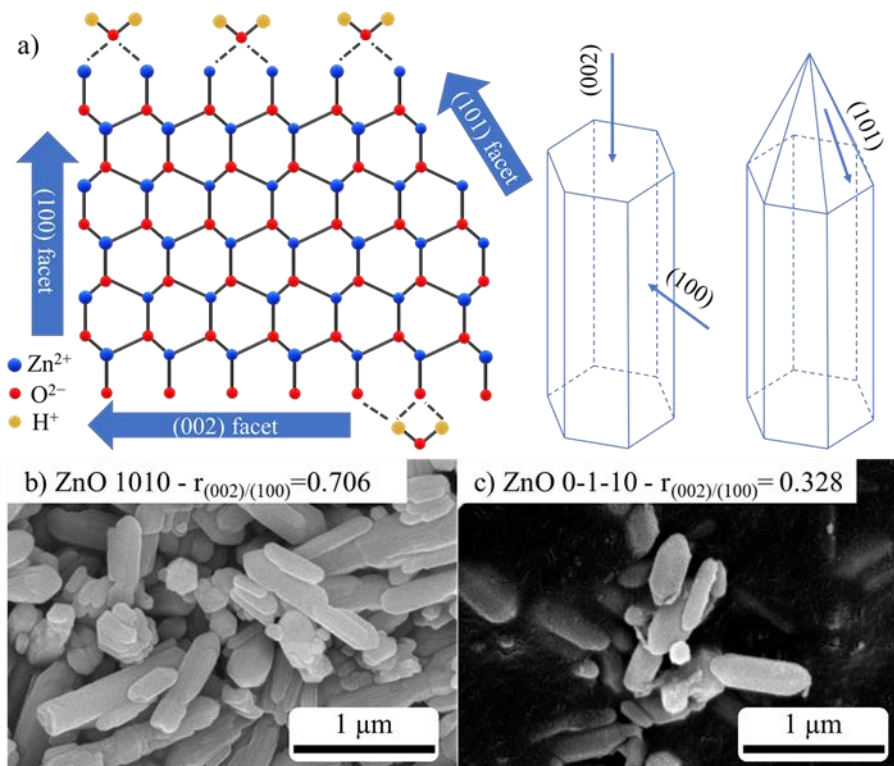
Figure 19 Schematic representation of oriented growth of ZnO along different crystallographic planes (a); Scanning electron micrographs of samples ZnO 1010 (b); ZnO 0-1-10 (c) [120].

Several existing publications had the opportunity to examine the interval discussed in the present study (0.2–0.9), but unfortunately, it is not examined in detail or this feature was omitted completely. A few of these types of examples are presented in Table 3.

Table 3 Comparison of literature data of different ZnO photocatalysts based upon the observed ratio of (002)/(100) and activity [120].

Synthesis method	Photocatalytic activity experiment	Range of (002)/(100)	Observed Trend of photocatalytic activity with the ratio of (002)/(100)	Reference
Solvothermal	Photoreduction CO_2	0.91–1.27	Increased	[140]
Chemical bath deposition process	Photodegradation of rhodamine B	1.28–1.9	Decreased	[74]
High-temperature chemical precipitation	Photodegradation of rhodamine B	0.63–0.92	Increased	[141]
Chemical precipitation	Photodegradation of phenol	0.54–0.93 (I), 0.93–1.13 (II)	I-Increased, II-Decreased	[142]
Electrospinning deposition	Photodegradation of rhodamine B	0.81–1.06	Increased	[143]
Combustion	Photodegradation of methylene Blue, crystal Violet	0.4–0.55	Increased	[144]
Solvothermal	Methylene Blue	1–5	Decreased	[145]
Hydrothermal	Photodegradation of NO	0.9-7	Increased	[146]

X-ray diffraction is a powerful tool to characterize the structure of crystalline materials. To understand what signifies this change in the ratio of various diffraction peaks, their actual appearance on the diffractogram must be discussed. The signal in the diffractograms arises when the conditions regarding Bragg's law of reflection are fulfilled. This states that only at specific incident angles on an atom belonging to a specific crystal plane can occur a reflection, which can be seen as a signal in the detector. In an ideal crystal (perfectly ordered and spanning to infinity), this would result in diffractograms containing only lines at the specific Bragg angles in well-definable ratios. On the contrary, this is not possible, because at the particle boundary the constituent atoms will not have the same number of neighboring atoms. In consequence, the surface atoms always are in a different chemical environment than the bulk and implicitly have different energetical states [147]. To decrease this higher energetical state the surface structure is always distorted compared to the bulk, which causes the atoms to be in a slightly different position. This in turn will cause a shift in the Bragg angle, resulting in peaks, with lower maximum intensity. If the ratio of surface and bulk atoms increases, the peak breadth grows and the intensity decrease,

53

which is the basis of the Scherrer equation. Overall, this also imposes that the ratio of the areas of the peak should be maintained, which was also observed in the present case. The average ratio of areas for diffraction peaks (002) and (100) is 0.36±0.06. During the preparation of the powder samples for X-ray diffractometry, it can be assumed that the particles are randomly oriented. Thus, preferential orientation should not constitute an error in the measurement. Nonetheless, certain geometries of the particles (e.g. bars, plates) can self-organize preferentially, during placement on a flat plane, like the usual X-ray sample holder, if they have an increased size along a flat facet [148], but based on the size and the random ordering observed on SEM micrographs, this could be eliminated. Along the intensity of the peaks, the FWHM varies too for the ZnO samples. The Scherrer equation correlates the primary crystallite size to the FWHM, but it determines the average size of the particle. The Scherrer equation assumes that the crystallites are close to spherical and in consequence isotropic in all directions. In addition, the size is determined across the direction perpendicular to the corresponding plane of the peak. As such, the calculations were repeated for the other two main diffraction peaks, (100) and (101) (Table S3). This showed that size anisotropy is observable, but no conclusive relationship can be determined. This can be the consequence of the inherent problem of the BBD that the synergetic effects of parameters are intensified in the data. Nonetheless, size anisotropy is always observable, when intensity ratio of (002)/(100) changed.

The size anisotropy of the samples signifies that the synthesis parameters influence the crystal growth along facets corresponding to the mentioned crystal planes. This means the various facets could differ in the interactions which facilitate the chemical reactions of the formation of ZnO. The three main characteristic planes of ZnO differ in polarity in order of (100)<(101)<(002) [90]. On (100) facets, the charges are relatively evenly distributed and cancel each other out on the surface, which is slightly distorted on the (101) due to the higher distance between the terminating atoms with small local polarities[132,141]. On (002) facets are especially highly polar, due to these facets being Zn^{2+} or O^{2-} terminated and it is perpendicular to (100) [74,134,145]. As the nucleation of the ZnO might occur and there is a sufficient number of atoms present in the seed the crystal planes and facets will form. From this point in the crystallization, the polarity of the facets determines how they interact with the solvent and the unreacted precursor. As the solvent is composed of two liquids with very different polarities their interactions vary according to the polarity of the crystal facets. In the precursor molecule, the Zn^{2+} is coordinated by the two chelate molecules acetylacetonate,

but most likely these two planes of the zinc-enolate rings are perpendicular. The apolar nature of two methyl groups on acetylacetonate makes it less likely that the precursor could approach the polar facets and more readily can adsorb on apolar facets. The (002), more precisely the Zn^{2+} terminated [0001] facets can react more readily with water molecules, binding hydroxide on the surface. The oxygen terminated (002) is not likely for the mentioned reasons with the precursor. On the other hand, as the $ZnAA_2$ is reacted the liberated acetylacetone has sufficient polarity to adsorb and coordinate with surface Zn ions on polar facets, which could inhibit the growth at highly polar (002) facets. At the edges and peaks of (101) and (002), there is enough space and sufficiently low polarity along the (101) plane for the precursor or partially hydrolyzed precursor to coordinate with the edge oxygen facilitating growth along (101). This can be observed as the conical tips of the ZnO particles.

The beforementioned is enough to propose an explanation for the observed behavior of the ratio of (002)/(100) with the synthesis parameters. The most influential parameter was the solvent composition. At lower ethanol concentrations the water more readily can adsorb on (002) facets, which could inhibit the growth of the particle in the perpendicular direction, due to the low polar interaction of the precursor. This surface adsorption of water also leads to a local higher water concentration near the polar facet. The precursor is more soluble in ethanol and will hydrolyze rapidly forming a new seed or creating a (101) facet [76]. The temperature is also a predominant effect. All the reactions involved are temperature-driven, so by increasing the temperature the activation energy could be lowered. The higher thermal kinetic motion of the molecules can disrupt local inhomogeneities and the dielectric constant of the solvent is also greatly increased by temperature. This could explain why by raising the temperature the growth of the (002) facets is not inhibited.

Various kinds of research demonstrated that crystal facets contribute to or hinder the light-harvesting capabilities or photocatalytic reactions (Table 3). One plausible explanation could be that the different polarities of the crystal facets can have a preference towards different photocatalytic reactions. Considering the general reaction model for heterogeneous photocatalysis and the mentioned adsorptive properties of the samples based on their polarity, it can be assumed that the hydroxyl radical formation could occur at the (002) facets. This would also imply that higher photocatalytic activity should be observed with a particle with the (002) facets. Aside from the adsorptive properties of the facets the other properties should be evaluated. Due to the lower polarity and surface energy of (100) and (101) facets can host electron-hole pairs and consequently can move more freely. In addition,

size anisotropy could also affect the mobility of the electron-hole pair in the direction of the smaller cross-section, because of the quantum confinement effect [149]. This implies a possibility that the (002) facets contribute to the photocatalytic activity with the adsorption of water molecules as a source for hydroxyl and (100) or (101) utilization of the electron-hole pair. It seems that the synergetic effects of the crystal facets could be better exploited for photocatalysis.

On a few occasions, it was argued the [0001] crystal facet (a facet in (002) planes) is central to the photocatalytic reactions of ZnO [74,76], and to our best knowledge, the literature focused more on much higher ratios ($r_{(002)/(100)} > 1$). In much higher values of (002)/(100), the photocatalytic degradation of methylene blue [150] followed a similar, but opposite trend, as well as in the case of rhodamine B [140,151] and photoreduction of CO_2 [132]. Considering that the previously mentioned literature does not discuss the present interval of the ratio of these crystallographic facets (0.2–0.9) proves that this interval could induce an opposite trend upon the photocatalytic activity.

Considering the results and the above-discussed arguments, the following conclusions can be made:

- The Box-Behnken experimental design with reduced experimental runs was successfully used to investigate possible correlations between the structural characteristics of ZnO semiconductors and their photocatalytic activity.

- The synthesis parameters (precursor concentration, solvent composition, temperature and duration of the solvothermal treatment) were correlated with the photocatalytic activity and a structural parameter the ratio of the intensity of X-ray diffraction peaks (002) and (100) in the range of (0.20-0.88).

- The correlations were further optimized to maximize photocatalytic activity and the model was validated with new experiments and photocatalytic measurements.

- A plausible cause of the change in $r_{(002)/(100)}$ is the size anisotropy of the crystallites, more precisely the decreased diameter across perpendicular to (002).

- The polar-polar interactions of the solvent molecules and crystal facets are the main cause of the structural change and oriented growth of crystallites.

- The resulting model indicates that the photocatalytic activity can be enhanced by increasing the $r_{(002)/(100)}$.

5.2. Morphological modification: ZnO solid spheres

In the previous section, the relation between a structural parameter of ZnO ($r_{(002)/(100)}$) and photocatalytic activity was discussed. It was mentioned that due to the fractional experimental design two parameter values were changed compared to a central point experiment. This made it difficult two deduce single-parameter relationships. Further the original synthesis method was modified by fixing the precursor concentration and the duration of the solvothermal treatment to the previously determined optimum values (0.068 M and 10 h). For the morphological modification spherical morphology was chosen as it is simple and isotropic geometry. The research published by A. Šarić et al. [126] and A. Gómez-Núñez et al. [127] proved that monoethanolamine and triethanolamine can facilitate the formation of spherical morphology of ZnO. Although two different precursors (zinc acetylacetonate and zinc acetate) were used with two slightly different morphological agents, the similarity in the mechanism of formation suggests that the two methods can be combined. Unfortunately, the photocatalytic activity was not investigated as a basis for comparison. In the literature, the synthesis methods of TiO_2 usually include the application of single Ti precursor or an in-situ preparation/modification of the precursor. The work of A. Tiwari et al. [152] a two-precursor-approach was applied and obtained different anatase/rutile crystal phase ratios with two different precursors. The application of a mixture of precursors resulted in tunable ratio crystal phases between the values, compared to those obtained during the single precursor approach. The application of the two different precursors resulted in ZnO spheres with different average diameters. Considering the similar structure and bonding between zinc and the two anions (acetylacetonate and acetate), a mixed precursor approach could result in a tunable spherical morphology. In addition, the $r_{(002)/(100)}$ structural parameter was investigated, and how it changes with the morphological modification.

5.2.1. Preliminary investigation of synthesis parameters

The first objective was to investigate the synthesis conditions that facilitate the formation of ZnO with spherical morphology and photoactivity. The micrographs (Figure 20) showed that spherical morphology can be achieved at high ethanol concentrations (99% and 100%). Unfortunately, the photocatalytic activity was notable, when 99% ethanol was applied during synthesis. A. Šarić et al. [126] and A. Gómez-Núñez [127] argued, based on theoretical calculations, that monoethanolamine and triethanolamine can form relatively stable zinc-based complexes with both precursors. The N and O atoms of the amine and

hydroxyl groups can coordinate with the Zn^{2+} ion. Based on the similarities between this alkanolamine family, it can be fairly assumed that diethanolamine can also form stable complexes. X. Wang et al. demonstrated that the number of spherical particles can be increased by controlling the concentration of monoethanolamine in water-based solutions [153]. Moreover, the publication of A. Šarić et al. [93] showed that organic solvents offer better control over the formation of spherical ZnO particles. Based on these two publications, a synthesis method can be developed to investigate and control the relationship between spherical morphology and photocatalytic activity. In the previous section, we discussed that the formation of ZnO from these precursors involves at least a hydrolysis step forming hydroxylated oligomers, which can form ZnO through dehydration processes [154,155]. In case of insufficient water concentration, unreacted DEA complexes could remain at the particle boundaries, which hinders photocatalytic activity.
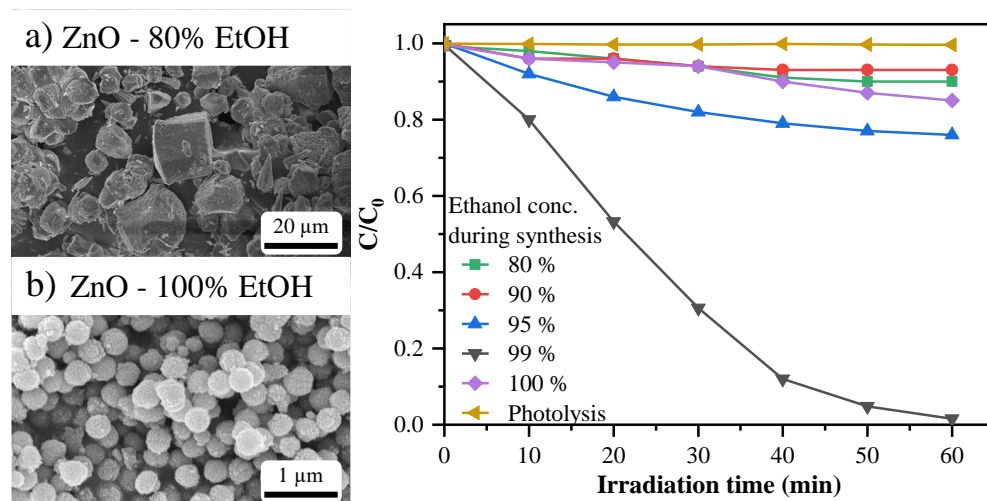
Figure 20 SEM micrographs (a, b) and phenol degradation curves of the ZnO samples from the preoptimization experiments (c) [93].

In the previous section was demonstrated that solvent composition can have a great influence on the structure, so X-ray diffractometry was used to study the as-synthesized ZnOs. On the diffractograms of the samples, the crystallographic planes of the hexagonal wurtzite structure (100), (002), (101), (102), (110), (103), (200), (112) and (201) (Figure 21) were present (JCPDS 36–1451). In every case when ethanol concentration was below 99% v/v, the small additional peaks $Zn(OH)_2$ appeared (JCPDS 38-0356) [129,156]. The previously mentioned hydroxylation reaction of the precursor probably takes place at a much faster rate, due to the high water content, and dehydration is inhibited. In consequence, the photocatalytic activity is decreased due to the presence of the impurity phase, $Zn(OH)_2$. The

poor crystallinity of the sample synthesized at 100% ethanol, can be observed from the broad diffraction peaks. In this case, the zinc precursor-DEA complexes lack the water to complete the hydrolyzation reaction. To ensure the spherical morphology of the particles and an acceptable photocatalytic activity, in further experiments, 99–1% ethanol-water was chosen for the solvent composition.
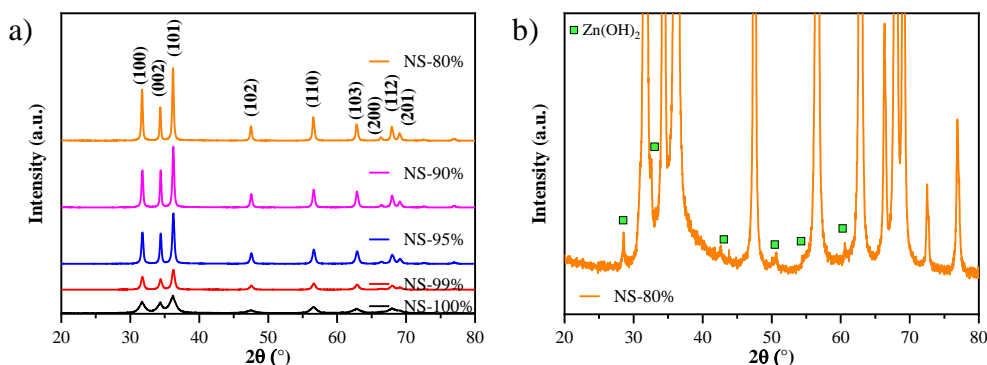
Figure 21 X-ray diffractograms of ZnO samples synthesized using different ethanol-water solvent compositions with the identified peaks corresponding to the hexagonal ZnO crystal structure (a) and the magnified diffractogram of NS-80% with small peaks corresponding to Zn(OH)$_2$ crystal structure (b) [93].

5.2.2. Characterization of ZnO spheres

As the required solvent composition for spherical morphology was established, the influence of the synthesis temperature (at 120, 150, and 180 °C), anion in precursor molecule (acetylacetonate, acetate), and respective precursor composition were investigated. The various ZnO samples were examined using XRD, FT-IR, DRS, SEM, and TEM.

On the X-ray diffractograms, the corresponding peaks of the usual hexagonal wurtzite structure were identified with no impurity phase observed (Figure 22). The crystallinity and well-defined peaks were good indicators to further evaluate the diffractograms using the three calculation methods for the primary crystallite size. Compared to the Scherrer equation, the W-H and SSP methods involve additional terms describing the broadening of the diffraction peaks, due to the crystal strain. These equations can still be improved using various correction terms for the anisotropic strain, but on various occasions proved to be inconsequential to the result [157]. The main advantage of these two methods is that if there is no broadening due to strain (in the case of an ideal crystal), the equations used in these two methods will be reduced to the conventional Scherrer equation. On the other hand, in the case of notable crystal strain, the calculated primary crystallite size will

be greater compared to the ones calculated by the Scherrer equation, which happened to be in the present case [158,159].
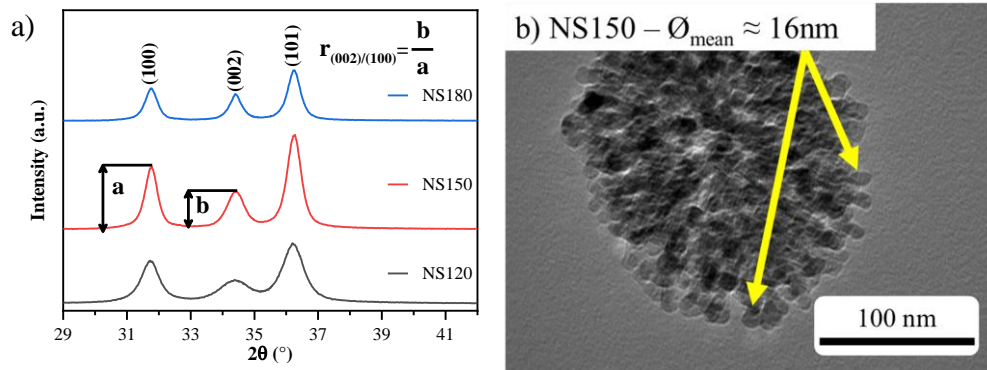
Figure 22 X-ray diffractograms of ZnO samples synthesized using ZnAA₂ precursor at different temperatures (a) and a corresponding TEM micrograph showing crystallites with a mean diameter of 16 nm that build up the sphere (b) [93].

TEM measurements can also offer to verify the results obtained by the various methods used for primary crystallite size calculation. Two samples were selected randomly for TEM investigations. In Figure 22b can be observed that the spheres are composed of smaller crystals and their size was measured using ImageJ software. In Table 4 presented the various mean primary crystallites size values, based on the four different methods. The values obtained using XRD data give information about the average coherent diffraction length. In other words, the average distance where the unit cell is repeated without structural defects. Imperfections (e.g. dislocations, vacancies, etc.) can lower this value, so the actual mean primary crystallite size could be slightly bigger [129]. Another thing to consider is that XRD gives information about a large volume of the sample, while TEM only offers information about a minuscule amount of the sample, but it can be improved by increasing the data volume. In the present case, the mean diameter of the crystallites determined by TEM was based on at least 300 diameters.

Table 4 Mean crystallite size of NS150, and M10NS120 determined by different XRD data evaluation methods [125].

Sample	Mean primary crystallite size (nm)			
	Scherrer	W-H	SSP	TEM
NS150	14.8	16.5	15.0	16
M5NS120	9.6	9.7	7.7	11

Based on Table 4, one can be observed that W-H values are closer to the actual crystallite size determined by TEM and the values, based on the Scherrer equation is smaller. This could be expected because the fraction of the surface atoms is significant at such a low scale and those atoms occupy a slightly distorted position, which in turn generates strain. All in all, crystal strain is an important factor to consider at the nanoscale, so W-H or SSP

In Figure 23 is strikingly observable that the application of precursor mixtures always resulted in a primary smaller crystallite size compared to the samples prepared from one precursor. In addition, the actual composition of the mixture induces only a mild change in the crystallite size. Considering that the byproducts of the ZnO formation could be acetic acid or acetate anion, it is probable that these molecules could facilitate the hydrolyzation of the $ZnAA_2$-DEA complex. This could promote the fast process of crystal seed formation. Also, this trend of smaller crystallite size was unaffected by the change in synthesis temperature. Another observable trend that indifferent of the composition with increased temperature the crystallite size also increased as well.
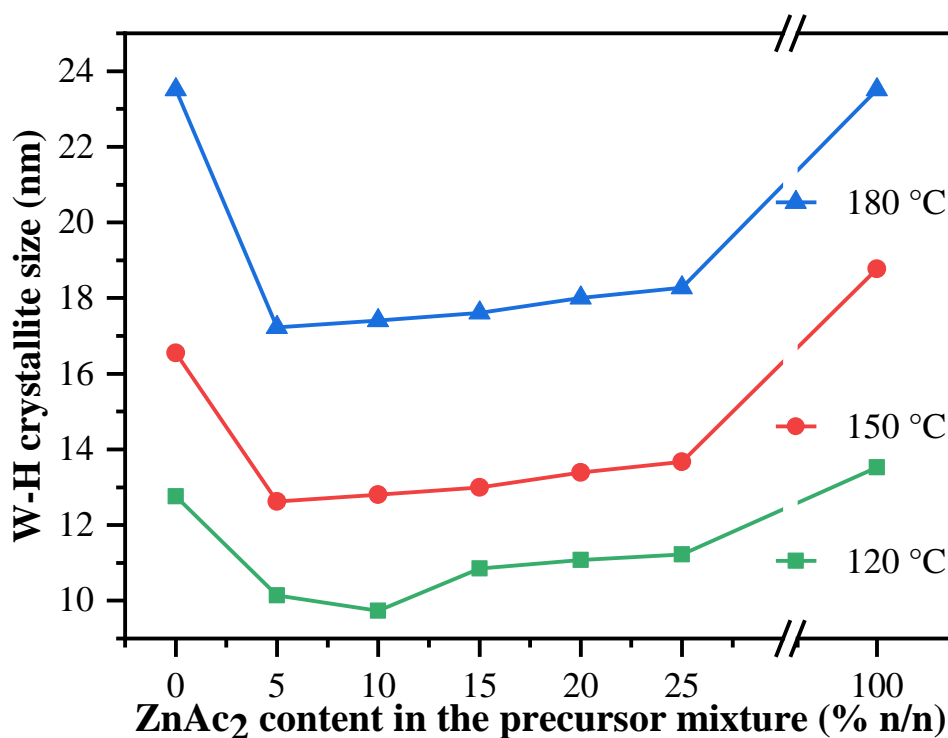
Figure 23 Crystallite mean size of the synthesized ZnO spheres estimated by the W-H method [93].

The abovementioned structural and morphological features (Figure 23) imply that the applied method provided valuable information regarding the mean primary crystallite size and average diameter of the spheres. The tuning of the mean primary crystallite size seems possible, by simply adjusting the temperature of the solvothermal treatment and the ratio of precursors. Examining the diffractograms further (Figure 24), the intensity ratio of the two peaks corresponding to the (002) and (100) crystallographic planes was increased for the samples with the increase of the synthesis temperature as in the case of ZnO nanorods. In powder diffraction is assumed that the crystallites are randomly oriented. Considering that ZnO crystallites are arranged in spherical aggregates the possibility of preferential orientation can be eliminated. Besides the change in intensity of the (002) peak, an increase in the FWHM is also observable, as previously. The FWHM is directly correlated to the mean primary crystallite size of the particle by the Scherrer equation [42]. Considering that in the present case every sample was synthesized at the three mentioned temperatures, the problem observed with the BBD is less prevalent. As such the calculations were repeated for the other two main diffraction peaks, (100) and (101) (Table S2). In this case, the results clearly show that the primary crystallite size is always smaller for the (002) peak. Also, the same trend was observed with the ratio of the sizes calculated for (100) and (002) peaks as

with the intensity ratios. Consequently, size anisotropy is the cause of the variation in the intensity ratio of (002)/(100), more specifically the decreased primary crystallite size in the direction normal to the (002) plane.
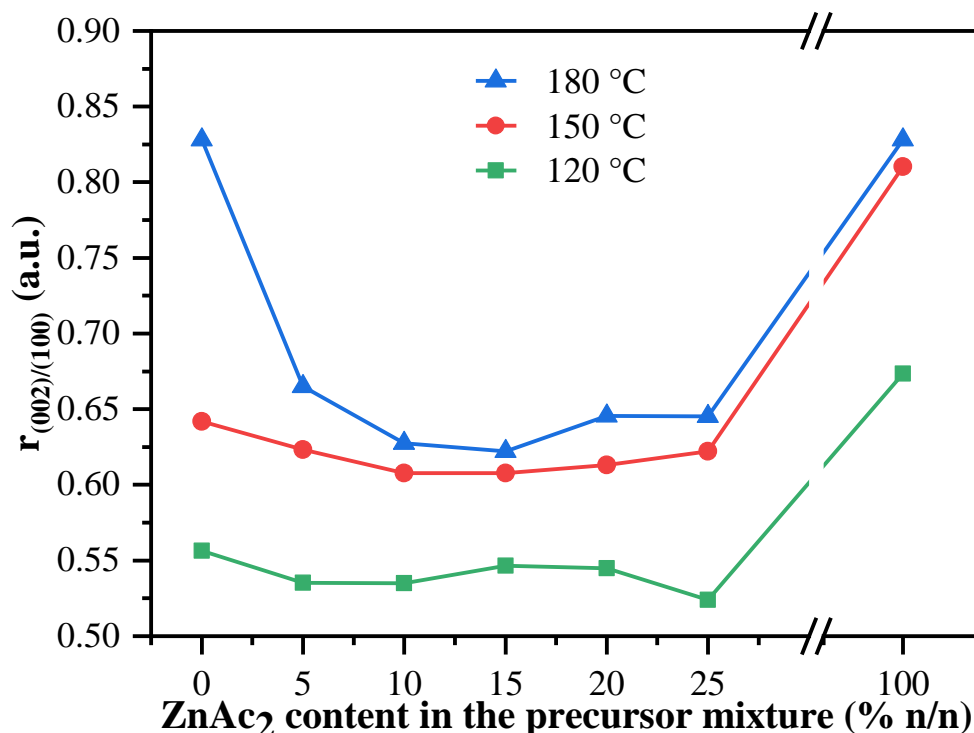
Figure 24 Ratio of intensities of two peaks corresponding to the (002) and (100) as a function of the ZnAc$_2$ content in the precursor mixture (b) [93].

Irrespective of the temperature or precursor type, the as-prepared ZnO samples always showed spherical morphology. Based on the experiments performed by using the two precursors purely (i.e., without mixing them), the size of the spheres was of two different orders of magnitudes: the size of spheres was 305 nm for ZnAA$_2$ (NS180) and 2.81 µm for ZnAc$_2$ (MS180) (Figure 25). It was inferred that the ZnAc$_2$-DEA$_x$ complexes were less stable and promptly interact with water molecules due to the polarity difference between the acetate ion and acetylacetonate. The formation of hydroxide taking place at a much faster pace could explain the almost tenfold increase in the average diameter of NS180 compared to that of MS180. The diameter distribution histogram for sample NS180 is presented in Figure S6. The other main difference between the two samples was that the microspheres (MS180) were highly polydisperse, while the nanospheres (NS180) were monodisperse. This arises from the interaction between the byproducts that form due to the hydrolysis of precursors. Acetylacetone is miscible with the solvent, while acetate could be

released in an ionic form before becoming protonated, increasing the number of inhomogeneous regions in the sol.
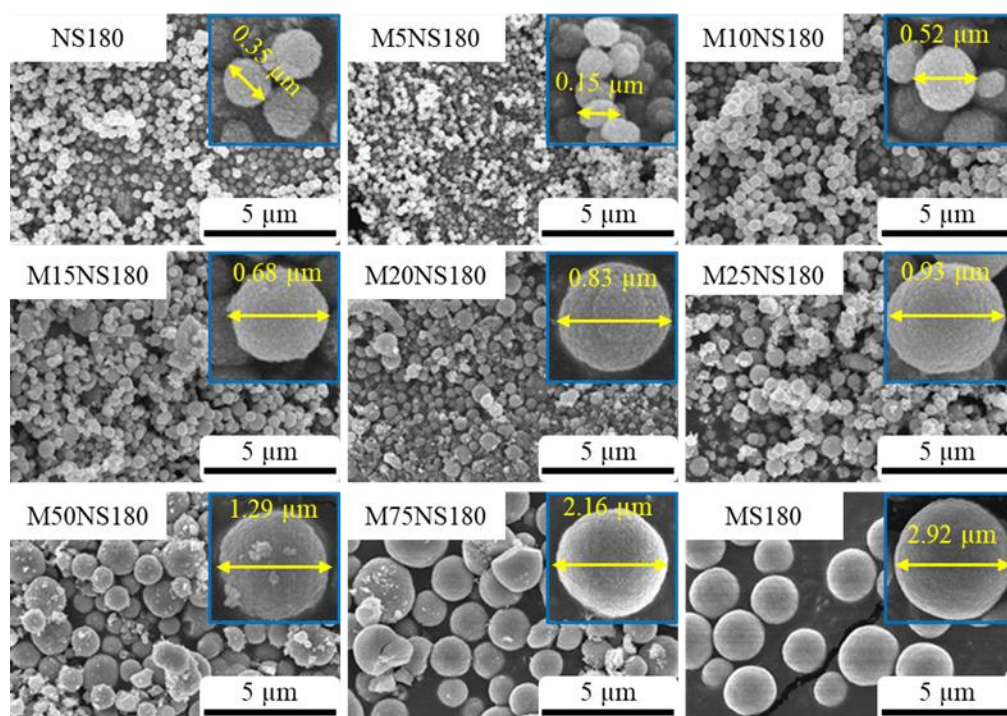
Figure 25 SEM micrographs of the samples synthesized by applying different precursor mixtures at 180 °C (the ratio of precursors is indicated in the sample code as NS and MS samples with pure ZnAA$_2$, respectively ZnAc$_2$; MxNS180 – the "x" number refers to the molar percentage of ZnAc$_2$ in the ZnAA$_2$-ZnAc$_2$ mixture [93].

The SEM micrographs in Figure 25 reveal that the average diameter of spheres is changing according to the composition of the precursor mixture. The size range of the spheres is situated between the samples prepared from the pure precursors (NS180 and MS180). Moreover, the observed average diameter is proportional to the zinc acetate:zinc acetylacetonate molar ratio. This suggests that the crystallization from the two precursors can occur in synergy, which also implies that anions participate with a similar mechanism in the reactions. It is worth mentioning, that there is one exception, M5NS180, which has the smallest average diameter of 155 nm, smaller than NS180 (305 nm), but considering that it is only one sample out of 27, it is an acceptable error.

A linear equation fitting was carried out for the samples synthesized at 180 °C with an $R^2 > 98\%$, showing that a well-quantifiable empirical relationship exists between the composition of the precursor mixture and the observed diameter of the ZnO spheres (Figure 26). For all the precursor mixtures, the synthesis was carried out at 120 and 150 °C. The average diameter showed opposite trends for the two precursors, in the case of MS samples

increased, while in the case of NS samples decreased with temperature. It has been already been shown that the crystallite size is temperature dependent and interestingly, Figure 26 shows that in the same samples synthesized at different temperatures the trend of size increase with composition persists only the slope of the line is increasing with the temperature. In addition, these opposite trends of the precursors with temperature were balancing each other in the mixtures with an equilibrium at ~25% ZnAc$_2$. Considering that, the crystallite size increased with the temperature consistently in the case of the whole series of samples, the formation of spheres should be determined by an agglomeration process separately after the crystallites have already formed.
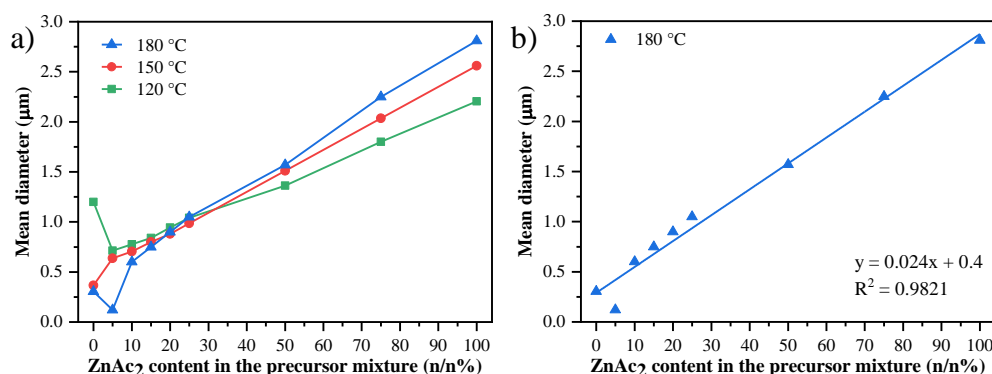
Figure 26 Mean diameters determined from the SEM micrographs as a function of ZnAc$_2$ content of the precursor mixture for the three synthesis temperatures (a) and a linear equation fit for the 180 °C sample series (b) [93].

Intuitively, the equilibrium point where the trend lines should change their tilt would be expected at 50%, but it is at 25% ZnAc$_2$. This suggests that the agglomeration of the crystallites to spheres is more influenced by the proprieties of the anions and in the case of acetate is more intense. Both chemicals can function as chelating agents, but acetic acid can donate the hydrogen ions more readily than acetylacetonate, otherwise said, it is more acidic. DEA, due to the amine group, can act as a base, so a mild acid-base reaction system can form with the free acetic acid and acetylacetonate, but based on the polarity of the functional group this reaction system can be overtaken by the stronger DEA-acetic acid polar interaction.

For the samples synthesized at 150 °C and from pure precursors at all three temperatures, the specific surface area was measured using nitrogen adsorption. To test whether the average diameter of the spheres correlates with the specific surface area (S$_A$), it was estimated using the following equation [160]:

$$S_A = \frac{6}{D \times \rho} \times 10^{-6} \tag{20}$$

In (20) D is the diameter of the spherical particles (cm) and ρ is the density of ZnO (5.606 g·cm^{-3}). Based on equation (20), the specific surface area is inverse proportional to the diameter and the same trend is revealed in the measured values (Figure 27). As could be expected, there is a magnitude difference between the estimated S_A and the measured values. If the specific surface area is estimated based on the primary crystallite size (S_{A-WH}), the results are closer to the measured ones. Even though the same trend can be observed for S_A and S_{A-WH}, this variation in S_{A-WH} reflects only 2 nm of change in crystallite size, so should be applied cautiously.
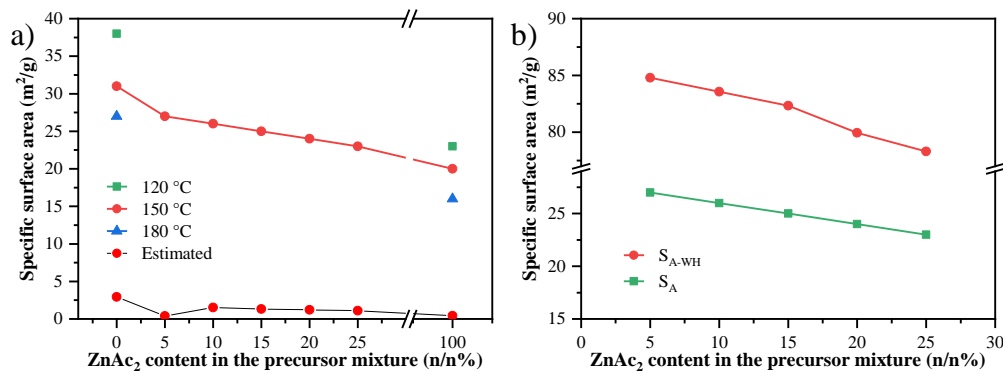
Figure 27 Specific surface area calculations (S_{A-WH} is the estimated specific surface area for the W-H crystallite size) [93].

Based on the previously made observation about the morphology, primary crystallite size and their relation to the precursor composition and synthesis temperature the following can be deduced:

    i)   BET and TEM measurements revealed that the primary crystallites are not closely packed in the spheres.

    ii)   The formation of the crystallites and the actual spheres are separate processes and the spheres are likely agglomerated from the separately formed crystallites;

    iii)   The various parameters (temperature, precursor composition) are influencing the structure and morphology, which can be easily controlled by these parameters.

Sufficient data has been acquired to conceptualize the mechanism of the formation of the ZnO spheres (Figure 28). This mechanism is proposed from the moment when the homogenous reaction mixture is prepared and the thermal treatment has been initiated. First,

the hydrolysis of the precursor-DEA complexes takes place, due to the increased ambient thermal energy in the reactor, and the crystal seeds form. During the initial growth, the by-products of the hydrolysis (acetate and acetylacetonate anions, respective DEA, and water) can saturate the surface of the crystallite because of the noncovalent interactions, which could hinder the crystal growth and cause the small size of the crystals. The released DEA can be adsorbed on the surface of the particles through hydrogen bonding, leading to aggregation. The high surface energy due to the small size of the particles could also contribute to the tendency to form spherical aggregates. Next, the crystal growth is continued in the spherical agglomeration causing the crystallites to link at contact surfaces. As the growth progresses the surface area at the contact points is lost. This could explain, why the specific surface area is situated between the estimated values corresponding to the diameter of spheres and the primary crystallite size.
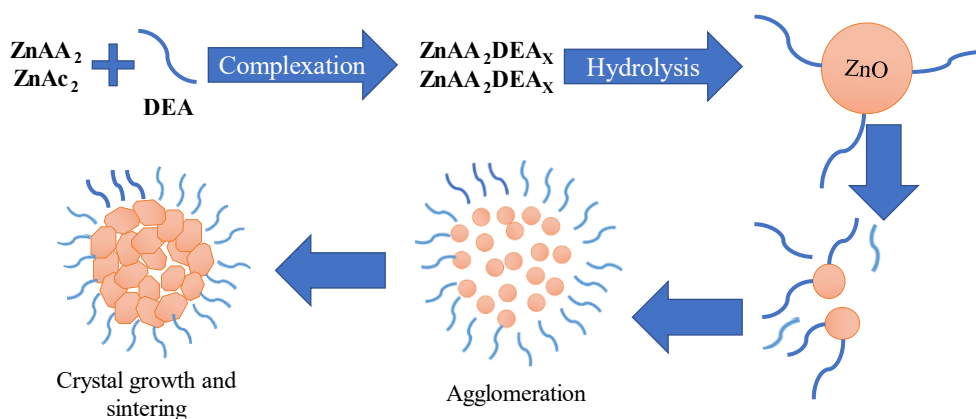
Figure 28 Proposed mechanism of the formation of ZnO spheres [93].

Figure 29 are presented the results of the FT-IR measurements. The stretching Zn–O and bending Zn–O–Zn was identified in the range of 390–540 cm^{-1}. The broad band at 3434 cm^{-1} corresponds to stretching vibrations of O–H of adsorbed water. The bands with low intensity are associated with organic impurities, but fortunately, their ratio with the Zn–O stretching vibrations is not as significant as observed previously in the literature [93]. The high purity of the samples can be caused by the addition of water during synthesis, because the stronger hydrogen bonding of water, could prevent the chemisorption of the byproducts The identified by-products with their corresponding wavenumbers were the following: N–H (3250 and 910 cm^{-1}), C–H (2973, 2925 and 2856 cm^{-1}), C=O (1616 and 1396 cm^{-1}), C–N (1270 cm^{-1}) and C–O (1065 cm^{-1}).
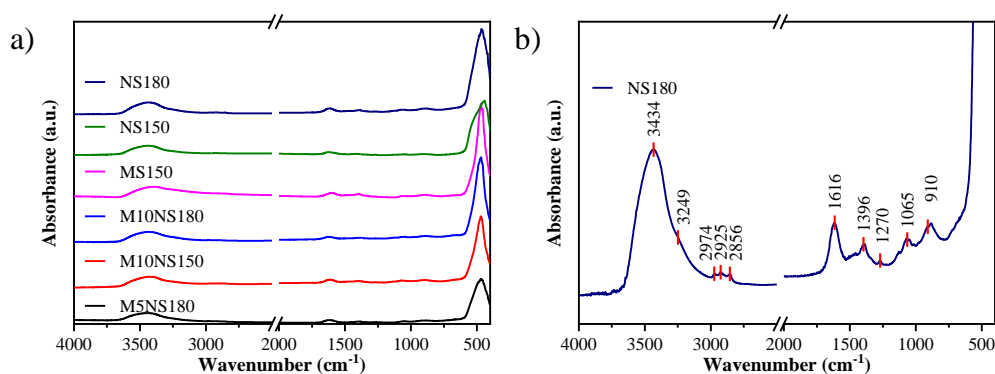
Figure 29 FT-IR spectra of the investigated photocatalysts: some representative sample (a) and the magnified region of a for sample NS180 (b) [93].

Diffuse reflectance spectroscopy was used to investigate the optical properties of the samples. The derivative method and Kubelka-Munk transformation were applied to calculate the band-gap energy. Based on these calculations, no significant change can be observed in the band-gap energies, as all values are in the range of 3.12–3.19 eV. However, the band-gap values slightly decreased according to the acetate concentration for samples synthesized at 180 °C. In addition, the lower synthesis temperature also increased the band-gap energy. Considering that the lower synthesis temperature causes the anisotropic growth of particles, this slight change could be attributed to the defect states in (002) facets [161].
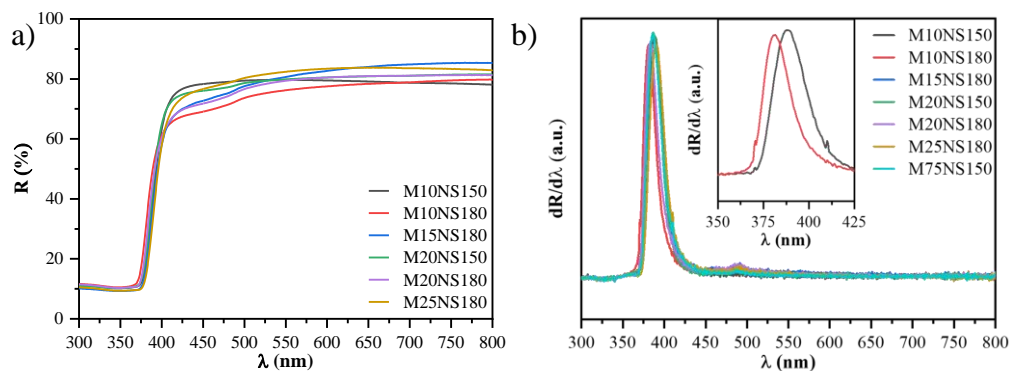
Figure 30 Diffuse reflectance spectra (a) and their respective first-order derivative spectra (b) of some of the ZnO semiconductors with inset of magnified range (350-425 nm) for two samples synthesized at different temperatures [93].

Photoluminescence (PL) is an effective way to study the optoelectronic transitions in semiconductor materials. The main bands, where emissions can be expected are the near band edge emission (NBE) in the UV and near-UV region, which is specific to the exciton recombination. Usually, in the range of 450–750 nm, is a broad emission, which has been established to be caused by the defective states of the ZnO: blue-green in 480–550 nm,

originating from the singly charged oxygen vacancies, yellow in 580–610 nm from doubly charged oxygen vacancies or zinc interstitials, the orange-red in 620–750 nm is proposed to be the defect complexes involving zinc vacancies or zinc interstitial complexes due to oxygen vacancies [160,181,182]. The PL spectra of the samples M15NS prepared at the three different temperatures are shown in Figure 31. The specific NBE and oxygen vacancy emissions can be easily identified. In addition, the effect of synthesis temperature is observed as a change in the intensities of both regions of emissions. The increase in the synthesis temperature leads to the decrease of the NBE emissions and increases the defect emissions, which indicates that the recombination path of the electron-hole is favored through the oxygen defects. Other PL spectra of samples synthesized at different temperatures (Figure S7) are showing the same trend. The temperature is also related to the size anisotropy of the crystallites, it indicates that orientation along (002) planes lead to more oxygen defect-related emissions. As stated before, the oxygen defects are more native to facets corresponding to (002) planes. Once the electron-hole pair forms, it could travel in the crystal structure freely and randomly. Considering that the primary crystallites have a lower size in [002] direction, than in the case of pure randomness the exciton requires a shorter path to end up on a facet corresponding to (002), than to (100) or (101). This increases the likelihood of the electron trapping at oxygen defects, which could increase the recombination.
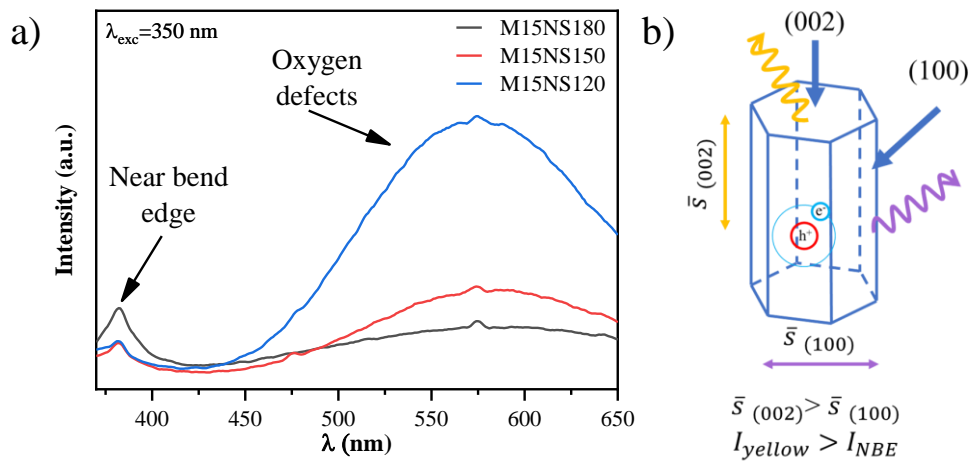
Figure 31 PL spectra of M15NS ZnO samples synthesized at different temperatures using 350 nm excitation wavelength (a) and schematic representation of how the average mean path of the electron-hole pair ($\bar{s}$) is related to the specific emissions (b).

5.2.3. Photocatalytic activity

Figure 32 shows the results of the photocatalytic degradation experiments of phenol under UV-A irradiation for the as-prepared spherical ZnOs.
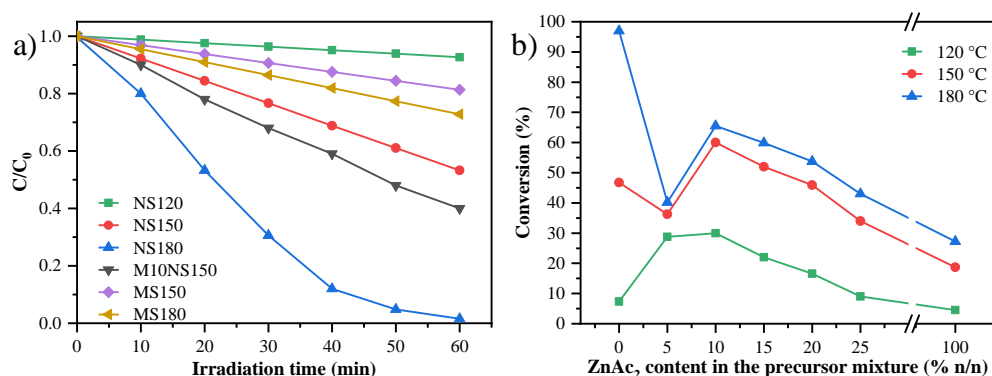
Figure 32 Photocatalytic activity of the investigated photocatalysts for phenol degradation under UV light irradiation (a) and conversion of phenol as a function of the precursor ratio used during the synthesis (b) [93].

The adsorption of phenol was less than 1% in the case of samples. During the degradation of phenol, various intermediates could form before reaching the final degradations products (CO_2 and H_2O), which were also detected in the present case (hydroquinone, resorcinol, hydroxyquinol, catechol, etc.) [162]. Besides the fact that at low concentrations the reaction rate also slows down, the curvature in the decay curve can also be attributed to the competitive reaction environment of phenol with its intermediates (Figure S8). The photocatalytic performance of the samples shows a wide range of variation (5-99%), which indicate that the structural and morphological differences influence this aspect.

Like all semiconductor-based photocatalysts, ZnO is also prone to photocorrosion [67]. NS180 was the best-performing catalyst, so it was selected for stability tests by applying the catalyst in 5 consecutive phenol degradation experiments. At the end of each cycle, the catalyst was separated from the suspension through centrifugation and reintroduced into a new solution. The results of the reusability tests are presented in Figure 33. The decline of the photocatalytic performance is higher after the second cycle, after which is only ~1% per cycle. Structural modification is also important a key aspect to verify stability. Considering that the primary crystallite size is relatively small and ZnO is prone to form $Zn(OH)_2$ on the surface, the agglomeration of the crystallites, respectively the appearance of impurity phases could be expected. Yet, surprisingly the X-ray diffractograms (Figure S9) showed no

significant difference or impurity, only a slight increase in crystallite size (~3%). In addition, the SEM measurements were also executed, to examine the effect of the degradation experiments on the morphology. Figure 33b reveals that aggregation of the spheres has taken place, which could be explained that the hydrated surface of ZnO, the spheres could adhere more efficiently to each other due to a stronger hydrogen bonding. Nonetheless, the catalyst can be considered stable.
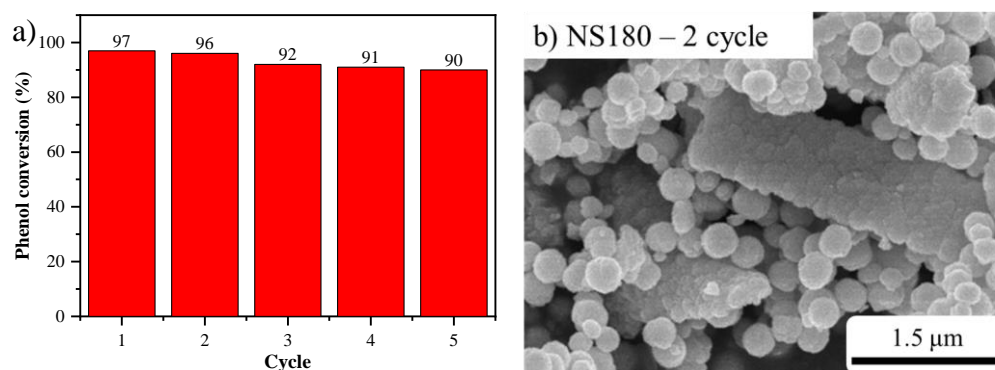
Figure 33 Catalyst reusability for NS180: a) phenol conversion measured for 5 cycles of reuse of the catalyst and b) a SEM micrograph of the dried ZnO sample after the second cycle [93].

5.2.4. Further characterization of the photocatalysts

Previously, in the case of ZnO synthesized using BBD, it was observed that a large number of parameters can influence photocatalytic activity. None of the observed trends can fully explain the variation in the photocatalytic activity and why it changes from sample to sample. The following observations were considered from the previous sections:

- DRS and FT-IR measurements do not show conclusive differences between the samples.
- The primary crystallite size better correlates with the specific surface area of the samples, than the diameter of the spheres.

- Among the structural features, the (002) and (100) crystallographic planes' diffraction intensity ratio ($r_{(002)/(100)}$) is the only one that changes according to the observed photocatalytic activity.

- The (002) orientation increases the likelihood of electrons being trapped in oxygen defect states.

The turnover frequency for the photocatalytic tests was calculated according to equation (21) [163] for NS, MS samples synthesized at 120, 150, and 180 °C and MNS samples at 150 °C.

$$TOF = \frac{\Delta C}{S_A \times C_{cat}} \tag{21}$$

In equation (21), *TOF* is the turnover frequency in nmol·m^{-2}·h^{-1}, *ΔC* is the change in concentration of phenol in an hour, S_A is the specific surface area of the sample, C_{cat} is catalyst concentration (1 g·L^{-1}). The data presented in Figure 34, demonstrates that by applying 150 or 180 °C during synthesis, a better photocatalytic activity can be achieved because of the increased r$_{(002)/(100)}$. In the previous section has already been argued that these parameters are related. Both the primary crystallite size and r$_{(002)/(100)}$ show similar patterns with the activity. Yet, PL measurements showed the crystallographic orientation and defect emissions are related. These defects states probably contribute to the utilization of the electron-hole pair for catalytic reactions, but a larger crystallite could also better stabilize them as well.
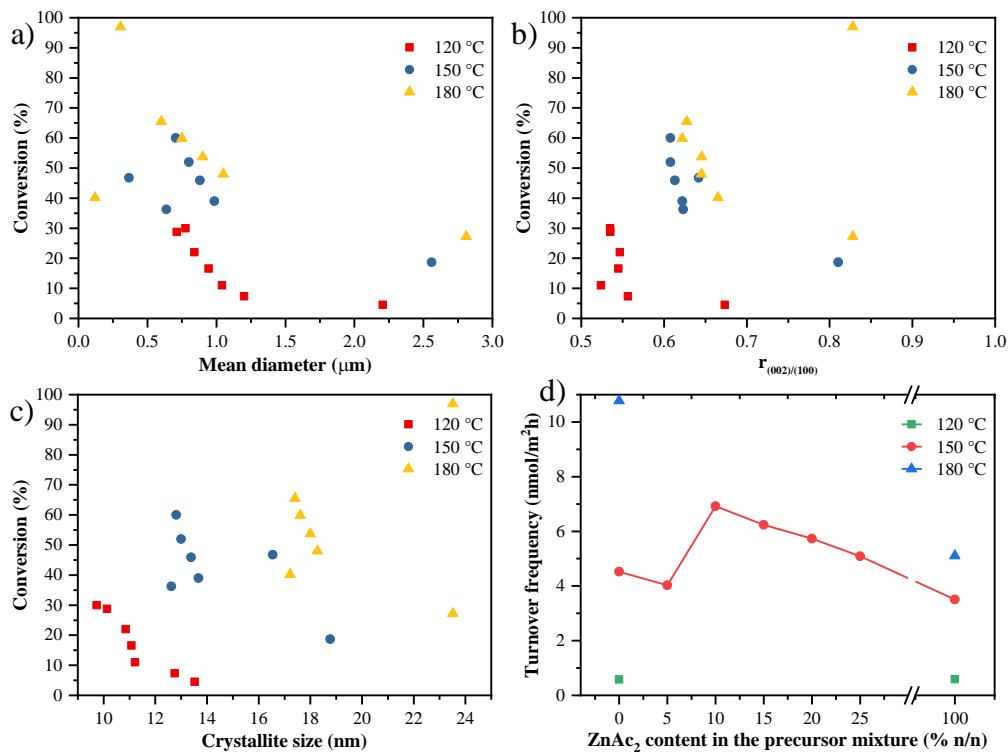
Figure 34 Material properties in relation to the photocatalytic activity: conversion in the function of mean diameter (a), r$_{(002)/(100)}$ (b), the primary crystallite size (c), and TOF in the function of the precursor composition (d) [93].

Considering that the ZnO spheres form from the aggregation of the smaller crystallites, we can fairly assume that their structural features (r$_{(002)/(100)}$, primary crystallite size) impact predominantly the photocatalytic activity. These possible relations of photocatalytic activity have already been hinted at in previous sections related to ZnO

nanorods and in the literature [164–166]. TOF combines the observed activity of the catalyst with its specific surface area. In Figure 34d the pattern formed by the TOF shows a decreasing trend with precursor composition in Figure 34c, as well as increasing photocatalytic activity with increasing crystallite size within the same temperature series. I propose that the activity is more likely influenced by the increased orientation along (002), based on the previous sections and arguments [167]. These facets can have more oxygen defect states, which adsorb more efficiently the reactants required for degradation (OH$^-$, O$_2$), then we can assume that a low proportion of this facet does not supply enough reactants to fuel the photocatalytic process. Likewise, the high ratio could supersede the regions responsible for the generation of electron-hole pairs.

Comparing the present results to the results in section 5.1 several changes are observed. Even though the crystallite size calculations used for the SSs are more accurate, the values are much smaller than those calculated for the nanorods. The solvent composition is modified outside of the previously examined intervals and a morphological agent (DEA) was applied, but the structural parameter, $r_{(002)/(100)}$, can still be tuned. In addition, the same trend with the photocatalytic activity and $r_{(002)/(100)}$ was preserved, despite morphological modification. Also, the catalytic activity is greatly improved. This enhancement can be attributed to the smaller primary crystallite size or simply that the crystallites are not so closely packed as in the case of nanorods.

Considering the results and the above-discussed arguments, the following conclusions can be made:

- Modifying the synthesis method of ZnO nanorods to synthesize ZnO solid spheres has been successful.
- Using a mixed precursor approach ZnO spheres can be accurately controlled in the continuous range of 120–2800 nm with similar high specific surface area.
- The W-H method for calculating primary crystallite size was found to be the most accurate among the methods applied.
- The structural parameter $r_{(002)/(100)}$ can still be tuned regardless of the modification of the synthesis
- The mechanism proposed for the formation of spheres is a 3 step process: it starts with the formation of crystal seeds, then spheres were formed via

agglomeration according to the precursor composition, followed by crystal growth and sintering.

- The photocatalytic activity trend with $r_{(002)/(100)}$ is changed, despite the modifications to the original synthesis.
- The $r_{(002)/(100)}$ is also related to the ratio of NBE and oxygen defect emissions.

5.3. Morphological modification: ZnO hollow spheres and noble metal composites

The morphological modification of ZnO to ZnO SSs greatly improved the photocatalytic activity compared to the ZnO nanorods. In addition, the structural tunability, respective to its relation to the activity, is both maintained. This suggests that the original synthesis has flexibility for modification without sacrificing other beneficial properties of the resultant semiconductor. This flexibility provides the opportunity to further investigate other morphological modifications, which might improve photocatalytic efficiency. Further, the work of B. Réti et al. [169,170] and T. Gyulavári et al. [80,104,171] was taken as the basic strategy for further improvement of photocatalytic activity. In the mentioned publications TiO_2 hollow structures were prepared using carbon sphere templates and hollow TiO_2-noble metal composites. Modifying the method with the addition of a template can thoroughly test this flexibility of synthesis, especially if the structural control is still maintained. The ZnO SSs provide a consequential basis of comparison to investigate how the hollow spherical morphology influences the photocatalytic activity as tunable reference material. Even though there are some existing publications describing the synthesis of ZnO hollow spheres using spherical carbon templates [172–175], their number is scarce and to the best of our knowledge, $ZnAA_2$ was not used as a ZnO precursor for the synthesis of hollow spheres using carbon sphere templates. As the previous results demonstrated superior photocatalytic activity can be achieved for ZnO using the $ZnAA_2$ precursor, but the other possible precursors were also considered in the preparation of hollow structures. Also, the preparation of CSs developed by B. Réti et al. [169,170] is unique, because the carbon source used is ordinary table sugar, which has a different chemical structure than the most commonly used glucose. Based on the previous results during the solvothermal method, the ethanol concentration was raised to 99.3%, because the lower water content slowed the crystal seed formation and is the highest value on which ZnO was still obtained.

5.3.1. Preliminary investigation of synthesis parameters

It has shown that the preparation of semiconductor oxides with hollow spherical morphology is founded upon the ability of metal ions to coordinate with the residual hydroxyl, carbonyl, and carboxyl groups on the surface of the CSs via chemical impregnation and subsequent removal of the template through calcination [71,75]. A difficulty in this procedure can arise if the binding of zinc ions is energetically less favored than solvation into the liquid phase.

Unfortunately, the chemical impregnation method was not successful and only a minute amount of solid material was produced and the application of $ZnCl_2$ as the precursor did not yield any solid material. On the other hand, the solvothermal method was successful and the yields were acceptable at >95%. The SEM measurements revealed that the samples are composed of large irregular agglomerates of small crystals (Figure 35). However, in the case of the $ZnAA_2$ precursor, some spherical particles are also formed. This implies that the zinc ions do not bind sufficiently to the surface of CSs and the crystallization occurs in the liquid phase or the ZnO crystals do not adhere to the surface sufficiently(Figure S10). A probable explanation could be that there are less amount of functional groups available since the applied purification method is thoroughly optimized to remove the by-products of the carbonization process [104].

Precursor	Chemical impregnation method	Solvothermal method
ZnAc$_2$		
ZnCl$_2$	No solid product	
ZnAA$_2$		
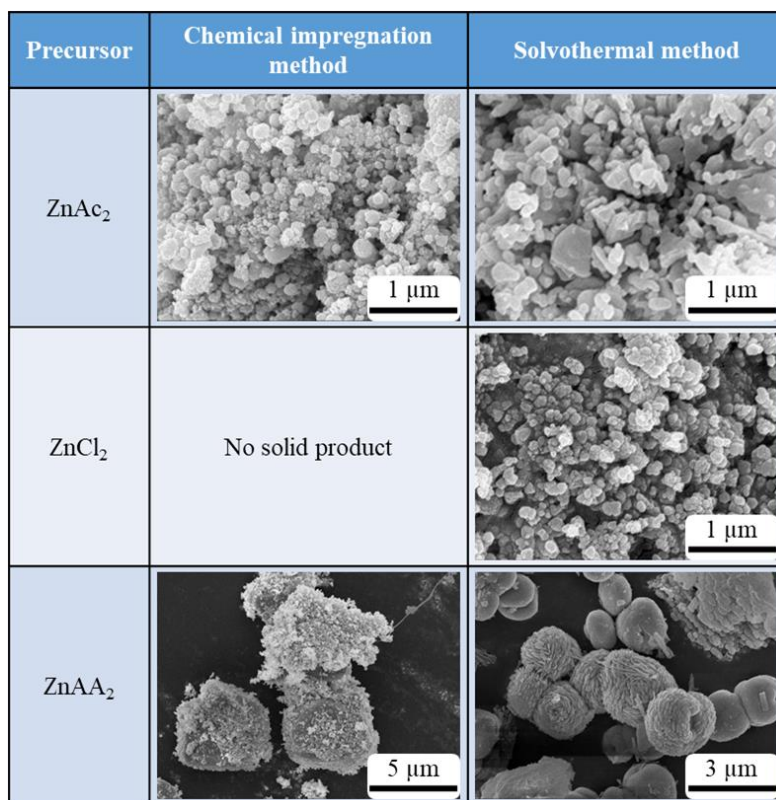
Figure 35 SEM micrographs of samples synthesized by chemical impregnation and solvothermal method [128].

The application of ZnAA$_2$ was the only precursor showing promising prospects to achieve hollow spherical morphology and also only in solvothermal methods. This method also requires parameter optimization, because the average diameter of particles was 10 times higher than that of the CS templates. The mass ratio of ZnO to CSs was selected as a variable synthesis parameter to optimize the thickness of the ZnO layer on the CSs with the following values: 10:1, 9:1, 7,5:1, 6:1, 5:1. Throughout these experiments the concentration of ZnAA$_2$ was kept constant. These are named "*ZnO-HSs-*" with a number at the end indicating the applied mass ratio of ZnAA$_2$:CSs. In Figure 36, it can be seen, that spherical morphology was achieved regardless of the applied ZnAA$_2$:CS mass ratio. Some additional irregularly shaped particles were always observable. A probable explanation can be that as the ZnO layer grows some loosely adhered crystallites could break off. At a lower concentration (e.g., at a 6:1 ratio), some spherical cavities could be observed at the surface of agglomerated particles, with sizes corresponding to those of CSs (~500 nm).
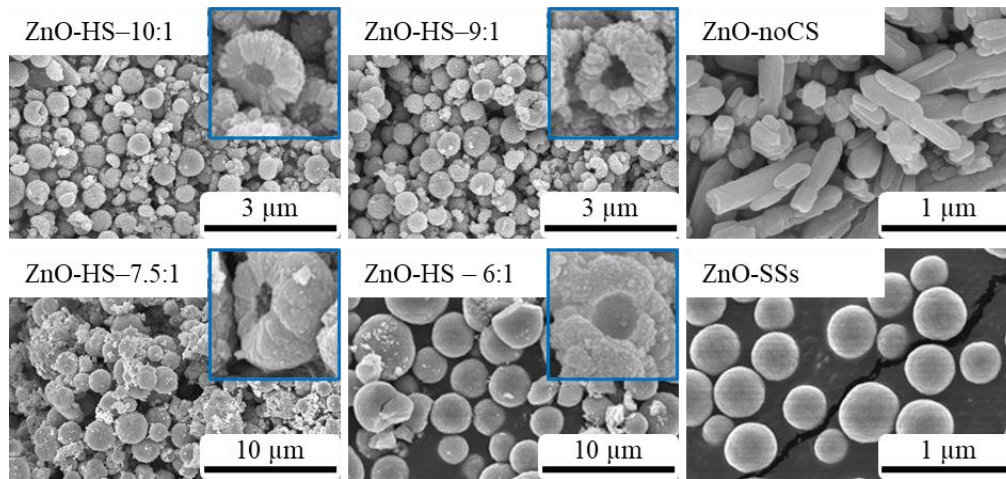
Figure 36 SEM micrographs of samples synthesized with different ZnAA$_2$:CS mass ratios and reference samples (ZnO solid spheres (SS) and ZnO samples synthesized without CSs (noCS)) [128].

The presence of smaller irregular particles could also indicate that the nucleation of ZnO occurs not just at the surface of the CSs, but also in the liquid phase. Using the SEM micrographs of ZnO-HS-10:1 and ImageJ software, the average diameter of spheres was determined as in the case of solid spheres in the previous sections, which was calculated to be ~800 ± 80 nm. In addition, the broken spheres confirm the presence of cavities in the spheres. Considering the average diameter of CSs (500 nm), the average thickness of the ZnO can be estimated to be ~150 nm, but TEM micrographs (Figure 37) revealed that the actual value is between 110–170 nm and the diameter of the cavities are between 350 and 450 nm. This difference can be caused by the sintering crystallites. The ZnO-HS-10:1 sample was selected for noble metal deposition in further experiments, and it will be referred to as "ZnO-HS". For reference materials, solid ZnO spheres were an evident choice (denoted as "ZnO-SS") using the synthesis method described in section 4.2.2, which had the same average diameter
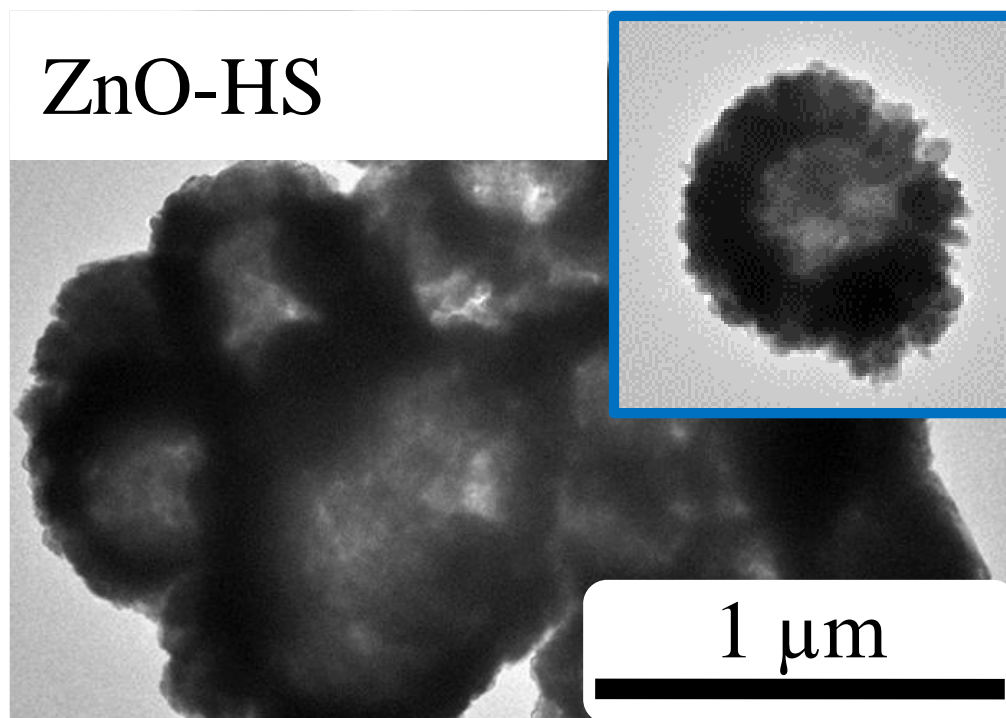
Figure 37 TEM micrograph of ZnO-HS synthesized with tuned ZnO:CS weight ratio [128].

5.3.2. Characterization of ZnO-HSs

The ZnO-HS and the noble metal/ZnO-HS composites were examined by XRD, FT-IR, and DRS measurements. The ZnO-coated CSs (ZnO-CS), solid spheres with an equal mean diameter (ZnO-SS), and a ZnO sample synthesized with the same procedure without the application of CSs (ZnO-noCS) were also characterized and used as reference materials to investigate the effect of the hollow morphology. The reference materials, ZnO-noCS and ZnO-SS were also calcined with identical calcination parameters.

On the X-ray diffractograms of the as-synthesized samples (Figure 38), the usual diffraction peaks corresponding to the hexagonal wurtzite crystal structure of ZnO have been identified (JCPDS 36–1451) at $2\theta°$: 31.74, 34.39, 36.21, 47.54, 56.59, 62.89, 66.38, 67.98, 69.11 [43]. The rest of the diffraction peaks correspond to the crystal structure of the noble metals: Au at 38.14 and 44.32 $2\theta°$ (JCPDS 04–0784) [176] and Pt at 39.70 $2\theta°$ (JCPDS 04–0802) [177]. Similarly to the previous sections, the peaks were analyzed using Pseudo Voigt function 1 of Origin Pro software. The as-determined numerical data was used to calculate the mean primary crystallite size of the ZnO crystal phase with the three previously mentioned methods (Scherrer equation, W-H, and SSP) and the results are presented in Table 5. Unfortunately, in the case of noble metals, W-H and SSP methods can not be used in the

present case, because of the small number of peaks, so the Scherrer equation was used to calculate the mean crystallite size. Considering that the synthesis method used to prepare the ZnO samples is based on the method presented in section 4.2.1 preferential orientation could be expected. Previously $r_{(002)/(100)}$ was used to express numerically the crystal orientation. The application of templates can influence crystal growth and preferential orientation, so to better examine this possible effect the texture coefficients were calculated for the three main diffraction peaks corresponding to the (100), (002), and (101) crystallographic planes

Similarly to the previous case of ZnO solid spheres the calculated mean crystallite size by the W-H and SSP methods are greater than those calculated by the Scherrer equation (Table 5). As described in previous sections the peak broadening is caused by the crystal strain, due to the small primary crystallite size.
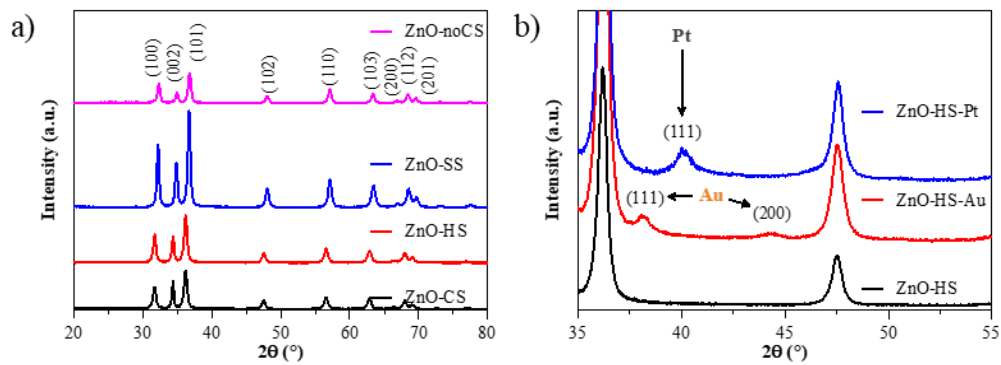
Figure 38 XRD patterns of a) ZnO samples and b) ZnO/noble metal composite [128].

Table 5 Primary crystallite size calculated by Scherrer equation, W-H and SSP methods, and TC values of the ZnO samples [128].

Sample	Primary crystallite size (nm)			TC			$r_{(002)/(100)}$
	$d_{Scherrer}$	d_{W-H}	d_{SSP}	(100)	(002)	(101)	
ZnO-noCS (reference)	16.68	17.75	17.18	0.97	1.12	0.93	0.73
ZnO-SS (reference)	17.14	23.45	20.45	1.05	1.06	0.89	0.68
ZnO-CS	14.48	20.50	17.25	0.84	1.41	0.75	1.25
ZnO-HS	15.59	26.24	20.54	0.95	1.22	0.83	0.91

It is important to emphasize that the reference materials have been calcined to eliminate errors when comparing the various samples to the reference materials. This is well

exemplified by the increase in primary crystallite size between calcined and non-calcined are increased (ZnO-CS, 20.50 nm, ZnO-HS, 26.24 nm). Even though the calcination temperature is relatively low, sintering can occur and particles can fuse at contact boundaries [178–180]. Considering that ZnO-noCS was synthesized based on the previously described method, it is no surprise that TC and $r_{(002)/(100)}$ show a strong preferential orientation for the (002) crystallographic plane. Surprisingly, the addition of CSs intensified the preferential orientation in this direction, despite the morphological modification. Due to the sintering of the crystallites, the preferential orientation can be affected. High preferential orientation of crystal growth can result in a higher proportion of certain facets belonging to a crystal plane family. This leads to a higher probability of contact between crystals at these facets during sintering. This can be observed in TC values of ZnO-CS (1.41) decreasing after the removal of the template (ZnO-HS, TC=1.22), technically the preferential orientation is half of the original value.

The primary crystallite sizes of the noble metals, determined by the Scherrer equation, are 9.57 nm for Au and 9.53 nm for Pt nanoparticles, which is in good agreement with literature data [73]. These values were also confirmed by TEM measurements (Figure 39), which revealed that the particles are randomly distributed on the surface of the HSs. In addition, the morphology of ZnO remained intact and no change was observable in the structure of the ZnO phase.
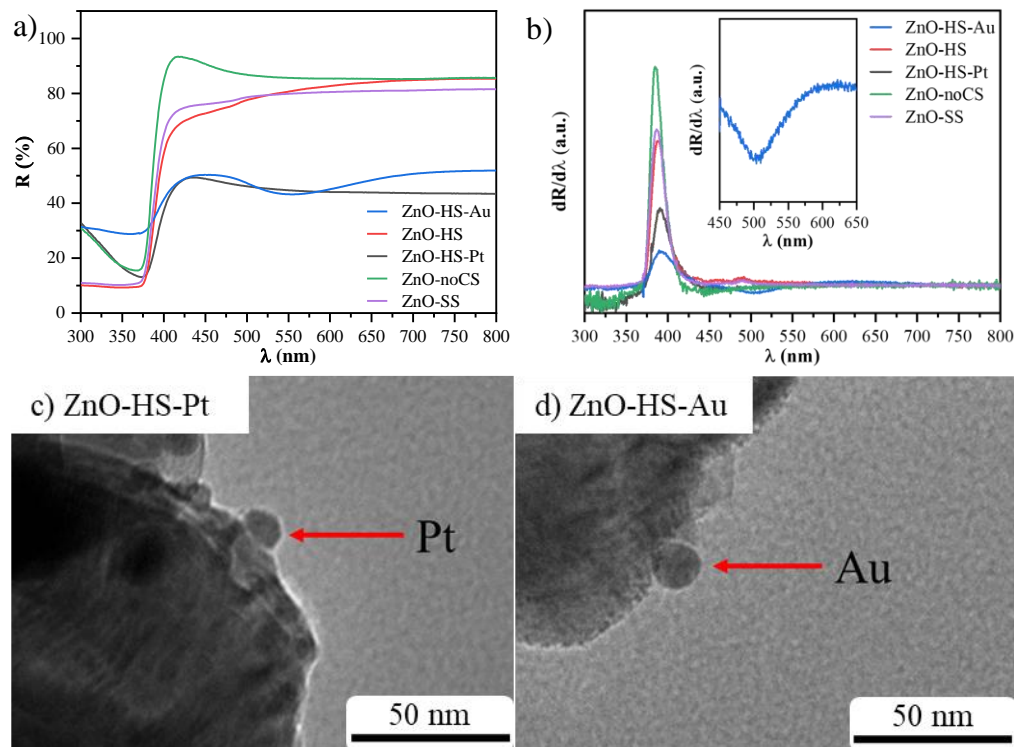
Figure 39 Diffuse reflectance (a), the first derivative of the diffuse reflectance spectra of ZnO samples (b) and their composites and TEM micrographs of ZnO-HS-Pt (c) and ZnO-HS-Au (d) [128].

DRS measurements were used to investigate the optical properties of the samples (Figure 39). Au and Pt nanoparticles absorb light in the visible spectrum and this could also be observed on the spectra of the composite samples, as the reflectance values are much smaller compared to pure ZnO-HS sample, despite the 1% metal doping. The previously described Kubelka-Munk and derivative method was used to calculate the band gap energies, but for composite materials, the derivative method is more advised, because for composite materials the spectra of the different components superimpose, so the derivative method was considered more adequate in the present case for ZnO. The band gap energies of the ZnO samples (ZnO-noCS and ZnO-HS) were calculated to be 3.19 respectively 3,22 eV. In the case of composites, a slight red shift in the band gap energies is observable (3.17 eV). In addition, an inflection curve (at 542 nm) specific for gold nanoparticles is observed and identified as the localized surface plasmon resonance of gold.

To further examine the spectra, the band gap tails, or Urbach energy (E_U), were calculated to investigate the defect state energy levels in the ZnO phase. Defect states play a key role in the stabilization of electron-hole pairs [181]. The Urbach energy was calculated according to the publication of P. Norouzzadeh et al. [43] and is presented in Table 6. The

influence of the noble metal nanoparticles can be observed in Urbach energies, as no significant difference exists in the values determined for the pure ZnO samples (ZnO-noCS, -SS, -HS) and surprisingly in the case of ZnO-CS as well. The E_U increased above 200 meV of the presence of noble metals.

Table 6 Calculated band gap (Eg) and Urbach energy (E$_U$) values of the ZnO samples [128].

Sample	E_g (eV)	E_U (meV)
ZnO-noCS (reference)	3.22	52
ZnO-SS (reference)	3.19	56
ZnO-HS	3.19	58
ZnO-HS-Au	3.17	232
ZnO-HS-Pt	3.17	240

In the photoluminescence (PL) spectra of the samples (Figure 40), the previously discussed NBE specific of the exciton recombination was identified at 391 nm. In addition, the defect emissions at 624 nm (yellow emission) and 646 nm (orange-red emission). [161,182,183]. The defect emissions are more intense compared to the ZnO samples described in previous sections. This region is further presented in Appendix Figure S11.
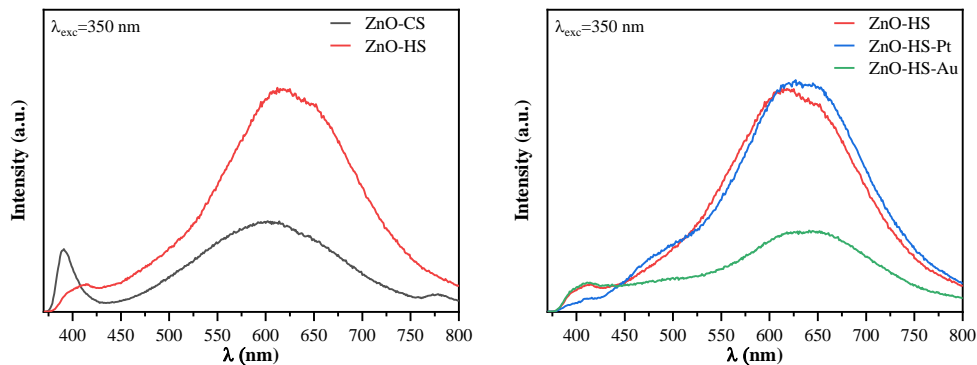
Figure 40 PL emission spectra of the as-prepared samples recorded at 350 nm excitation wavelength for ZnO-CS and ZnO-HS (a) and comparison between ZnO-HS and its respective noble metal composites (b) [128].

On the FT-IR spectra of the samples (Figure 41), the following bands were identified: Zn–O stretching vibrations centered at 460 cm^{-1} [184], adsorbed water at 3435 cm^{-1} (stretching vibrations of O–H bonds). In the case of ZnO-HSs, three additional narrow bands were observed at 1627 cm^{-1}, 1579 cm$^{-1,}$ and 1610 cm^{-1}. These bands can be identified as the bending and stretching vibrations of the chemically adsorbed water molecules or citrate residuals from the noble metal deposition [185]. Bands, which could indicate residuals originating from the incomplete removal of the template were not observed.
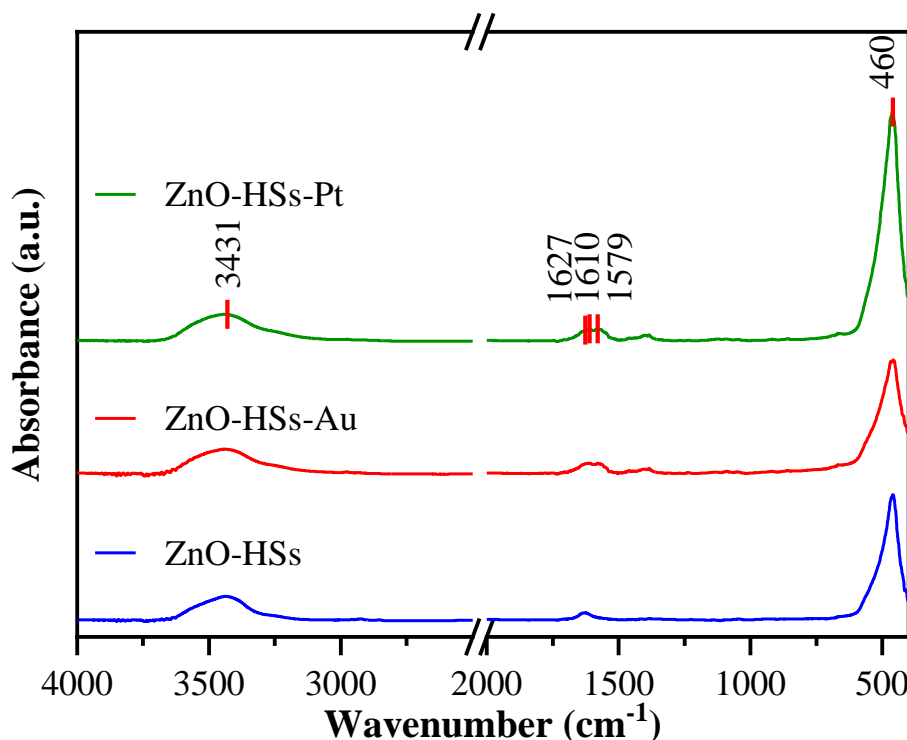
Figure 41 FT-IR spectra of the investigated ZnO photocatalysts: blue – basic hollow spheres, red – gold decorated hollow spheres, green – platinum decorated hollow spheres [128].

5.3.3. Photocatalytic activity

In Figure 42 is presented the photocatalytic activity of ZnO-HS, ZnO-noble metal composites, and the reference materials (ZnO-noCS and ZnO-SS). All samples were measured in the photocatalytic degradation experiments of phenol, ibuprofen and diuron under UV light irradiation. No significant change in concentration (<0.5%) was measured during the adsorption period (10 min) for none of the model compounds. In the photocatalytic degradation of phenol, ZnO-HS had an 83% and a 132% increased performance compared to the reference materials (ZnO-SSs and ZnO-noCS). This can be explained by the increased preferential orientation, as the reference materials had smaller

83

TC values, which have been reduced during calcination, but in the case of ZnO-CS this value was especially high, so did not diminish completely.
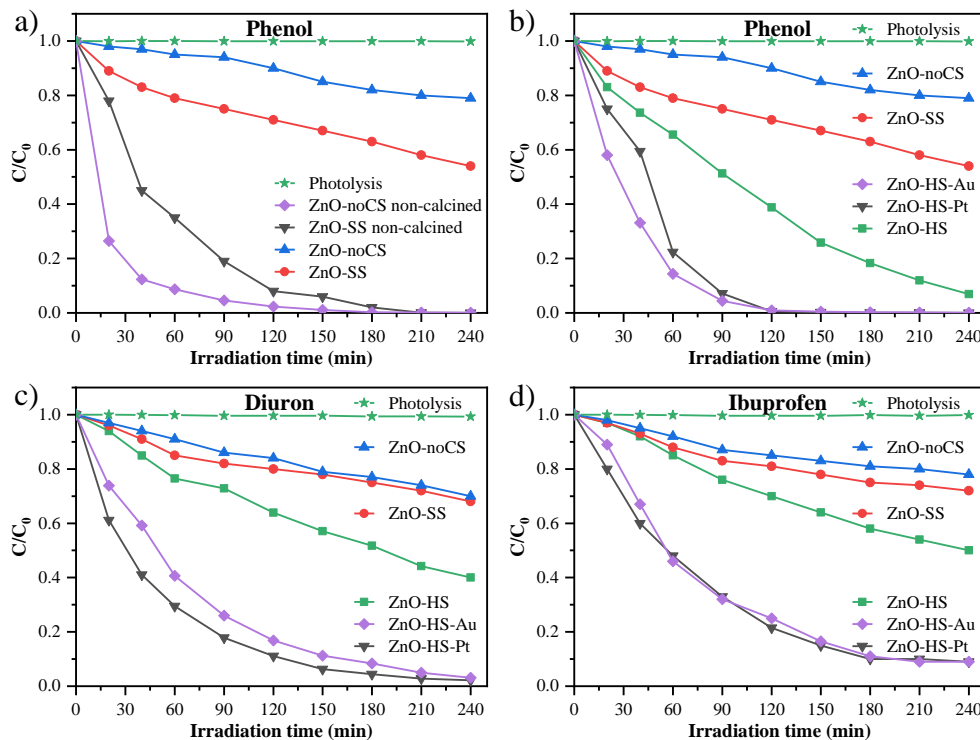
Figure 42 Degradation curves of model pollutants using the as-synthesized ZnO and composite samples under UV irradiation: comparison of the reference materials before and after calcination (a), phenol (b), diuron (c) and ibuprofen (d) ($C_{0,phenol}$ = $C_{0,diuron}$ = $C_{0,ibuprofen}$ = 0.1 mM) [128].

To investigate the influence of the noble metals, the photocatalytic performance of ZnO-HS-Au and ZnO-HS-Pt composites can be compared to the base material. To better quantify the differences between samples, the apparent rate constants (k_{obs}) were calculated (based on Figure 43) and are presented in Table 7.
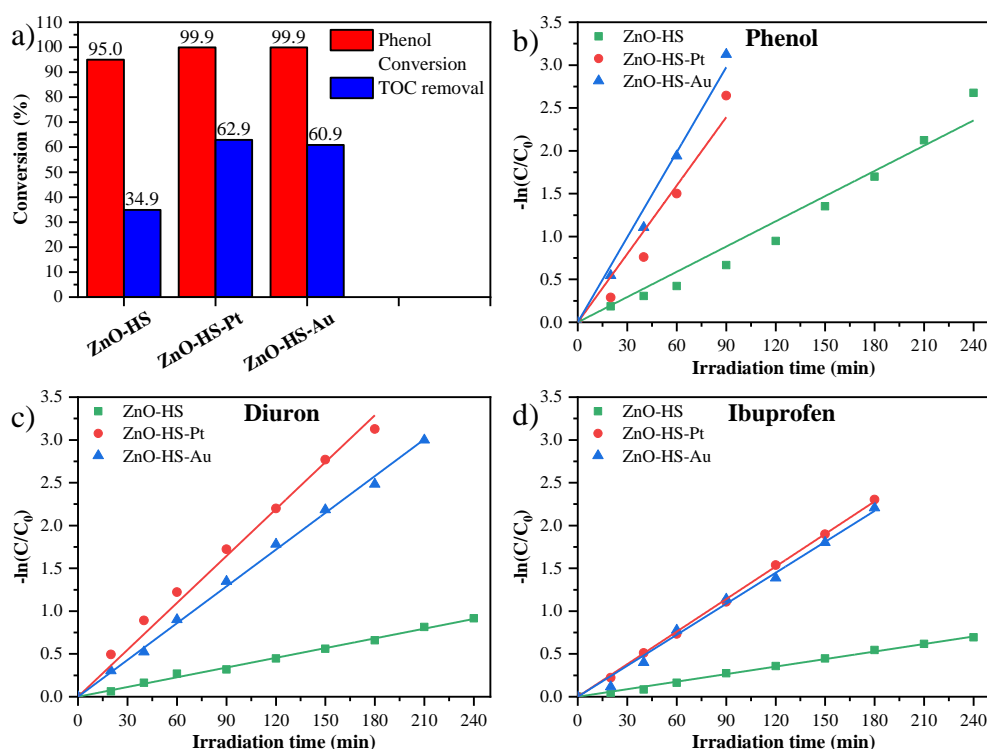
Figure 43 Phenol conversion and TOC removal values after 4 h (a), kinetic plots for phenol (b), diuron (c), ibuprofen of ZnO-HS, ZnO-HS-Pt and ZnO-HS-Au samples (d) [128].

Table 7 The calculated apparent rate constants determined for the as-prepared samples for the degradation of three model pollutants [128].

Sample	$k_{obs} \times 10^{-3}$ (min^{-1})		
	Phenol	**Diuron**	**Ibuprofen**
ZnO-HS	9.81	3.79	2.93
ZnO-HS-Pt	26.57	18.27	12.68
ZnO-HS-Au	33.05	14.32	12.07

The k_{obs} show a 270% and 336% increase in the case of the degradation of phenol for the Au and Pt composites. The increase in the case of diuron and ibuprofen is even greater. Noble metals improve the photocatalytic activity of semiconductors, due to their ability to accept electrons into the crystal structure and subsequently stabilize the charge separation process. There is a slight difference in the effect of the two noble metals on the

photocatalytic activity. An argument can be made based on the plasmon resonance of the metal nanoparticles, which is in the visible region in the case of Au, but in the case of Pt is in the UV. Thus, the used irradiation conditions facilitate light utilization more for Pt. Another aspect could be the higher affinity of gold nanoparticles toward electrons.

The photocatalytic performance of the base material and reference materials was considerably less in degradation experiments of diuron and ibuprofen compared to that of phenol. It should be considered that these organic molecules are more stable, and complex and form more degradation intermediaries [110,186,187], but the noble metal-modified samples degraded the model pollutants after 4 hours. ZnO-HSs-Pt had better photocatalytic performance than ZnO-HSs-Au, unlike in the phenol degradation experiments. The better activity specific to the case of diuron can probably be attributed to the chlorine substituents of the model compound. These chlorine atoms could be released to the suspension during degradation as chloride ions, which can interact readily with the (002)-oriented surface of the crystals [110]. Based on the PL measurements was proposed that Pt could utilize more efficiently at the near-band edge electrons.

A key aspect to consider in monitoring the degradation of these model pollutants is that the various intermediates could be more harmful than the original compound before reaching complete oxidation. In the case of the degradation of phenol, some of these intermediates were detected, which were identical to those observed in the case of ZnO SSs (Figure S8). Ideally, the completion of the photocatalytic reactions results in CO_2 and H_2O, so the change in total organic content (TOC) better reflects the efficiency of the photocatalytic degradation process. As could be expected, because of the intermediaries, the TOC values are much smaller than the phenol conversion values (Figure 43a) until 90% phenol conversion has been reached. The results also strengthen that the noble metal deposition improves the photocatalytic activity in general, as the TOC removal is significantly higher than the bare ZnO-HS. The time required for total mineralization is double for ZnO-HS (12 h) compared to the ZnO-noble metal composites (~6 h).

The ZnO-HS was selected for reusability and stability tests, in which the catalyst was used repeatedly in three consecutive phenol degradation experiments. The XRD and SEM measurements of the reused samples revealed that the performance and morphology of the photocatalysts are remarkably stable (Figure S12). Additionally, the best-performing catalyst, ZnO-HS-Pt, was selected for further degradation experiments in simulated wastewater conditions. Real wastewater could contain various organic and inorganic

materials. Usually, inorganic components are dissolved inorganic salts in the form of ions, of which the most abundant are Na^+, K^+, Ca^{2+}, Mg^{2+}, Cl^-, F^-, SO_4^{2-} and HCO_3^-. Considering, that organic components could mineralize completely to H_2O and CO_2 and inorganic components cannot be further degraded, they are the main focus of the present study. Inorganic ions could interfere with the hydroxy radicals or closely interact with the charged defects states on the surface of the catalyst, hindering the photocatalytic degradation process. For this purpose common mineral water was chosen, Theodora® from Kékkúti Ásványvíz Ltd., with the ion matrix detailed in Table S4, which was used to prepare simulated wastewater solutions with the same concentration (0.1 mM) of model pollutants used in the main study. These solutions were used for the photocatalytic test with the same conditions as described before.

The results of the degradation of the model pollutants in the simulated wastewater in comparison with the original experiments using MQ water are presented in Figure 44. Although, the concentration of the constituents of the inorganic matrix is more than 100 times higher than that of the model pollutants the degradation is only slightly slower.
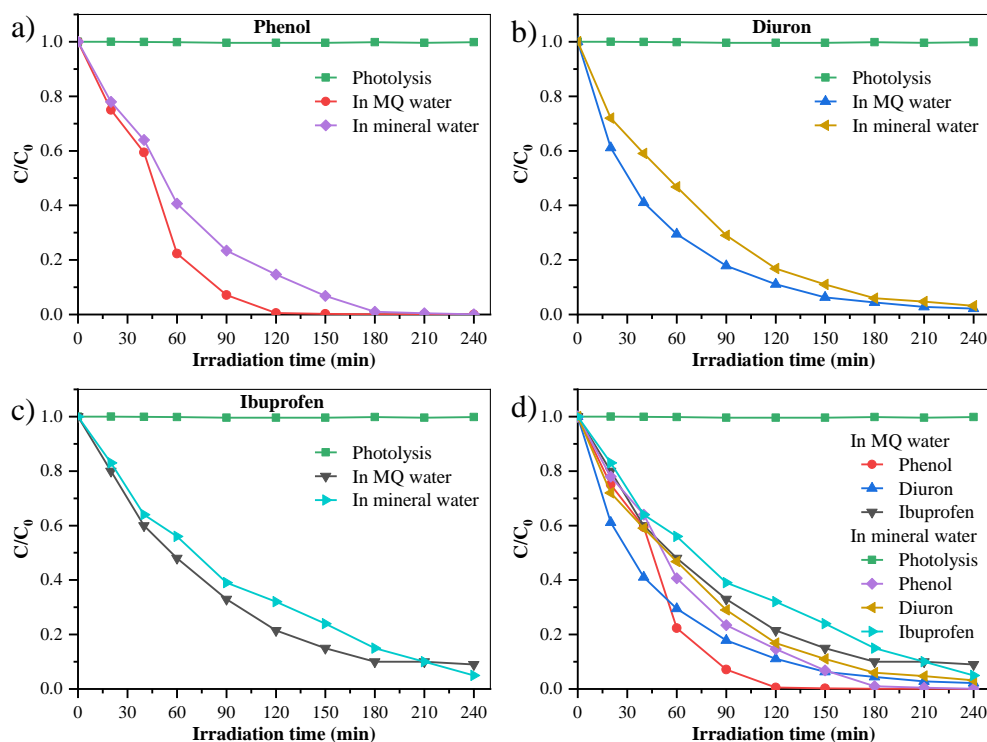
Figure 44 The simulated wastewater photodegradation test results for ZnO-HS-Pt for phenol (a), diuron (b), ibuprofen (c), and all of the decay curves together (d) [128].

5.3.4. Further characterization of the photocatalysts

Although publications studying the photocatalytic activity of ZnO hollow spheres are scarce, the results of a few studies are presented in Table 8 for comparison.

Table 8 The photocatalytic activity of several ZnO HSs in the literature [128].

Catalyst	Conditions of the photocatalytic experiment					Reference
	Catalyst concentration ($g \cdot L^{-1}$)	Model pollutant	Concentration of model pollutant (mM)	Degradation time (h)	Conversion (%)	
Reduced graphene-oxide/ZnO	0.2	Methylene blue	0.01	1.5	99	[92]
ZnO	0.5	Congo Red	0.02	1.5	85	[75]
Au/ZnO	1.7	Methylene blue	0.053	0.33	73.7	[109]
Au/Graphene/ZnO	Catalyst on substrate	Methylene blue	0.01	1	56	[188]
ZnO	1	Rhodamine B	0.042	0.83	99	[108]

Generally, calcination is an essential step in the synthesis of photocatalysts to improve crystallinity and remove moieties, originating from the synthesis. This is especially important in the case of ZnO because the formation of $Zn(OH)_2$ is difficult to avoid when water is present in the reaction mixture [92,188]. In the present case, this is also valid as minuscule amounts of acetylacetone could be adsorbed on the surface of the particles. The oxidation of these organic impurities and the CSs could also react with the loosely bound oxygen of ZnO. As a result of the preferential orientation toward (002) planes, which usually either end with an oxygen or Zn layer of atoms, this oxygen removal could be intensified. Subsequently, the calcination generates oxygen vacancy defect states at the oxygen-rich crystal facet, which could be detrimental to the photocatalytic activity.

Although it has been demonstrated that internal reflection can be exploited to improve the light-harvesting capabilities of TiO_2, optical properties of the material should be considered, such as absorptivity, and the thickness of the optical medium (shell). Considering the shell of the hollow spheres as curved thin films allows some fairly simple evaluation based on afferent literature data [91,189]. In the UV range, the transmittance of ZnO films is very low (<10%) even at film thickness values of 100 nm) [190], but high for

the visible range. Consequently, light harvesting through internal reflection in the present case is not probable.

To sum up, based on the photocatalytic experiments, the hollow spheres were more efficient than the solid spheres and the template-free reference regardless of the model pollutant applied. The noble metal deposition successfully increased the photocatalytic activity of hollow structures at least twofold.

6. Conclusion

In course of the research work, various methods were successfully applied to increase the photocatalytic activity of ZnO-based photocatalysts. During the investigation of the structural, optical, and morphological properties and the evaluation of the photocatalytic activities, significant relations were found and discussed in detail, and the following conclusions were drawn.

A three-level fractional factorial design, Box–Behnken design, was successfully applied for the optimization of the solvothermal synthesis of ZnO. The following synthesis parameters have been implemented into the model: temperature (90, 140 190 (°C)), the concentration of the precursor in the reaction mixture (0.068, 0.136, 0.204 (M)), ethanol content of the solvent (30, 60, 90 (%) v/v) and the duration of the solvothermal synthesis (4, 8, 12 (h)). The samples were characterized using XRD and DRS measurements. The photocatalytic performance of the samples was measured in the case of degradation of MO under UV irradiation. Significant changes were observed in the photocatalytic activity (PDE) and the ratio of intensities of two X-ray reflections corresponding to (002) and (100) ($r_{(002)/(100)}$). Two characteristics of the catalysts were observed to change while changing the synthesis parameters, PDE and $r_{(002)/(100)}$. Using ANOVA and these two responses, a full quadratic model was fitted and the model adequacy was evaluated and validated. The determined correlations were found to be adequate based on the R^2 values of 0.9913 for PDE. and 0.9743 for $r_{(002)/(100)}$ and analysis of residuals.

The correlations were used to maximize the activity and the structural parameter in optimization experiments, which resulted in new experimental parameter sets. The new parameter sets were verified by new experimental data, which resulted in a new ZnO sample with improved photocatalytic conversion values of MO (88%). The optimal parameter set for the solvothermal synthesis of ZnO were: temperature of 154 °C, the concentration of the

precursor $ZnAA_2$ in the reaction mixture of 0.068 M, ethanol content of the solvent of 90% v/v ethanol, and duration of the solvothermal treatment of 9.74 h. The optimization for the $r_{(002)/(100)}$ resulted in similar experimental conditions. This demonstrated that this crystallographic feature and photocatalytic degradation are related. The data demonstrated that with reduced experimental design, the photocatalytic activity and the orientation along (002) are related and can be tailored accordingly. The model is validated in the range of 0.2–0.88 for the ratio of intensities peaks corresponding to crystallographic planes (002) and (100). Therefore, this study showed that reduced experimental designs can be used for both the photocatalytic and crystallographic design of ZnO.

The previous solvothermal synthesis method was successfully modified to prepare ZnO photocatalysts with spherical morphology with two zinc oxide precursors (zinc acetate and acetylacetonate) with mean diameters of 305 nm and 2.813 μm, respectively. The used shape-tailoring agent was DEA. Based on the data obtained from the ZnO BBD model, the composition of the solvent (water-ethanol) was optimized in the 80-100% concentration range and it was established that 99–1% ethanol is necessary to achieve spherical morphology. It was also determined that this solvent composition is essential to prepare ZnO with noticeable photocatalytic activity.

Two other parameters of the synthesis method were examined to influence the activity and the size of the particles: the temperature of the solvothermal treatment (120, 150, 180 °C) and the ratio of the two precursors (5:95, 10:90, 15:85, 20:80, 25:75, 50:50, 75:25). Using SEM measurements, a linear correlation was determined between the average diameter of the spheres and the composition of the precursor mixture. In addition, it was demonstrated that the temperature also affects the change in the mean diameter, but not the linearity. Three different approaches (Scherrer equation, W-H, and SSP) were used to determine the primary crystallite size of the samples. The W-H method was demonstrated to be the most accurate among them, which values were verified by TEM measurements. Applying precursor mixtures has resulted in a smaller primary crystallite size of ~30% compared to the samples prepared from pure precursors. The precursor composition changes the crystallite size according to the $ZnAc_2$ ratio. The increase of the temperature of the solvothermal treatment increases the crystallite size, while the spherical morphology is unmodified. The specific surface areas were between 16 and 38 $m^2 \cdot g^{-1}$, which more correlated to the crystallite size based on the activity measurements. The FT-IR measurements confirmed the high purity of the samples.

In summary of spherical morphology modification, with the designed synthesis method the following aspects of the spherical morphology can be accurately tuned: mean diameter in the continuous range of 120–2800 nm. The mechanism of formation of the spheres was deduced to consist of two phases: first, the crystallization of ZnO particles in the range of 9–24 nm, followed by their agglomeration and growth according to the precursor composition.

The photocatalytic activity of the ZnO spheres was evaluated in the degradation experiments of phenol under UV radiation and it was demonstrated that the activity can be tailored with different precursor ratios. Despite the modifications applied, it was found that the increased ratio of the (200) and (100) crystallographic planes greatly influence the photocatalytic activity with a similar trend observed as before. The cause of the change in intensity ratio was established to be the size-anisotropy of the primary crystallites. This was determined by applying non-conventionally the Scherrer equation for the X-ray diffraction data. Using the XRD, PL and photocatalytic degradation measurements a causal relationship was determined to the previously found correlation between the $r_{(002)/(100)}$ and photocatalytic activity. This cause was the various recombination routes of the electron-hole pairs specific for the crystallographic facets corresponding to (002) and (100) planes. The high abundance of oxygen vacancies acts as electron traps and facilitates the internal recombination of the electron-hole pair, rather than utilization in the catalytic degradation process.

The described basic solvothermal synthesis method was modified to achieve hollow spherical morphology by applying sucrose-derived carbon sphere templates. In addition, the chemical impregnation method was evaluated for such morphological modification but was not successful. The coating of sucrose-derived CSs was successful during solvothermal synthesis. The ZnO:CS mass ratio was further optimized to tune the hollow spherical morphology and 10:1 was found to be adequate. Using SEM and TEM measurements the removal of templates by calcination was confirmed. Using XRD and the previously best-performing materials revealed that the calcination process reduces the preferential orientation towards the (002) crystallographic plane. In the case of ZnO-coated CSs, the preferential orientation was even greater than in the previous cases, even after calcination.

ZnO-HS-noble metal composites were prepared by deposition of Au and Pt nanoparticles using the chemical reduction method. The presence of 9 nm metal particles was confirmed by XRD and TEM. No structural or morphological change was caused to the ZnO-HSs by noble metal deposition. Based on the PL and DRS measurements, it was

deduced that the two noble metals participate with different mechanisms in the light-harvesting process of ZnO: Pt in the UV range and Au through the defect states.

The photocatalytic performance of the ZnO-HSs and its composites was evaluated in the degradation experiments of three model pollutants under UV irradiation: phenol, ibuprofen, and diuron. Because of the loss of preferential orientation caused by the calcination, the photocatalytic degradation efficiency of ZnO-HSs was greater by at least 70% compared to the reference materials. A remarkable increase was caused by noble metal doping (270% increase) in the apparent rate constants, but slight differences were observed in the case of various model pollutants. The catalysts were also reusable and stable during the reusability tests.

The increased activity of hollow ZnO samples was deduced to be rooted in the preserved preferential orientation towards the (002) plane. The application of CS templates improved the photocatalytic activity because further intensified the preferential orientation.

Overall, it can be stated, that the preferential orientation along (002) crystallographic planes are a key structural factor, which indicates a good performance in photocatalytic degradation of organic pollutants, which is also observable in the literature, despite the lack of emphasis on this aspect on various types of research regarding ZnO-based photocatalysts.

7. Összefoglalás

A kutatómunka során különböző módszereket sikeresen alkalmaztam a ZnO-alapú fotokatalizátorok fotokatalitikus aktivitásának növelésére. A szerkezeti, optikai és morfológiai tulajdonságok vizsgálata, valamint a fotokatalitikus aktivitások felmérése során jelentős összefüggéseket találtam, amelyeket részletesen kifejtettem, és az alábbi következtetéseket vonhatok le.

A ZnO szolvotermális szintézisének optimalizálására sikeresen alkalmaztam egy frakcionális faktoriális tervezetet (Box-Behnken). A ZnO szolvotermális szintézis 4 fő meghatározó paraméterét három különböző értékein vizsgáltam: a prekurzor koncentrációja a reakcióelegyben (0,068, 0,136 és 0,204 M), az oldószer etanol tartalma (30, 60 és 90 % v/v) és a szolvotermális kezelés hőmérséklete (90, 140 és 190 °C), időtartama (4, 8 és 12 h). Az előállított minták fotokatalitikus aktivitását megvizsgáltam metilnarancs bontása esetén UV besugárzás során, és XRD és DRS mérésekkel jellemeztük. Jelentős változásokat figyeltünk meg a fotokatalitikus aktivitásban (PDE) és a (002)-nek és (100)-nak megfelelő két röntgenreflexió intenzitásainak arányában ($r_{(002)/(100)}$). A vizsgált paraméterek és a két vizsgált tulajdonság (PDE és $r_{(002)/(100)}$) között egy kvadratikus modellt illesztettünk. A modell megfelelőségét ANOVA-elemzéssel mértük fel, és kiváló korrelációs összefüggést határoztam meg, amit a PDE esetében a 0,9913-as R^2 érték és az $r_{(002)/(100)}$ esetében a 0,9743-as érték bizonyít, ami a modellek által meghatározott értékek érvényességét jelzi.

A kapott modelleket sikeresen használtam a szintézis paramétereinek optimalizálására, és a kapott optimális paramétereket újabb kísérleti eredményekkel megerősítettük. A kiszámított optimális paraméterek 88%-os MO konverziót eredményeztek a ZnO esetében, a szolvotermális szintézis optimális paramétereihez kapott értékek: 154 °C hőmérséklet, a prekurzor ($ZnAA_2$) koncentrációja a reakcióelegyben 0,068 M, az oldószer etanol tartalma 90% v/v etanol és a szintézis ideje 9,74 h. Az $r_{(002)/(100)}$ optimalizálás hasonló kísérleti feltételeket eredményezett. Ez azt mutatta, hogy ez a kristály ezen struktúrális jellemzője és a fotokatalitikus bontás során tapasztalt hatékonyság összefügg. Mindazonáltal a kapott modellekkel és a validációs kísérletekkel sikerült kimutatni, hogy ezzel a szintézissel és modellel az előállítandó ZnO aktivitása mellett, a szerkezete, a (002) és (100) intenzitásainak aránya, is a 0,2-0,88 tartományban célnak megfelően változtatható. Ezért ez a tanulmány megmutatta, hogy a redukált kísérleti tervezetek mind a ZnO fotokatalitikus, mind a szerkezeti befolyásolására alkalmazhatók.

A korábbi szolvotermális előállítási módszert sikeresen módosítottam gömb morfológiájú ZnO fotokatalizátorok előállításához. A gömb morfológiát DEA-t alkalmazva értük el, amely alakformáló szerként viselkedett. Két különböző cink prekurzor (cink-acetát és -acetilacetonát) alkalmazásával két különböző mérettartományú gömböket eredményezett (305 nm és 2,813 µm). Először az oldószer víztartalmát vizsgáltam, hogy meghatározzam a gömb morfológiához szükséges optimális szintézis paramétereket, megőrizve a fotokatalitikusan aktivitást. A 99-1%-os etanol/víz arányt figyeltük meg mint optimális összetétel, mivel a magas etanol tartalom szükséges a gömb morfológia eléréséhez, az 1% víz pedig elengedhetetlen a ZnO minták magas kristályosságához és fotokatalitikus aktivitásához.

A szintézismódszer két további paraméterét vizsgáltam, amelyek befolyásolják az aktivitást és az elsődleges kristály méretét: a szolvotermális kezelés hőmérséklete (120, 150, 180 °C) és a két prekurzor aránya (5:95, 10:90, 15:85, 20:80, 25:75, 50:50, 75:25). A SEM mérések alapján a gömbök átlagos átmérője lineárisan változott az prekurzor keverékben lévő acetát koncentrációjának növekedésével. A röntgendiffraktogrammok segítségével a minták kristályméretét három különböző megközelítéssel határoztam meg. Ezek közül a W-H módszer bizonyult a legpontosabbnak, amit a TEM mérések is megerősítettek. A kevert minták kristálymérete mindig kisebb volt ~30%-kal, mint a tiszta prekurzorok használata esetén, valamint a prekurzor kevrék összetételétől függően változott. A szolvotermális hőmérséklettel a kristályméret növelhető, a morfológia megörzése mellett. A fajlagos felületek 16 és 38 $m^2 \cdot g^{-1}$ között voltak, ami nincs összhangban az átlagos gömb átmérők alapján becsült értékekkel. Ebből kiderült, hogy a fajlagos felület a kristályméret függvénye, és függ a prekurzor összetételétől. Az FTIR-mérések megerősítették a minták nagy tisztaságát.

Összefoglalva a gömbmorfológiai megfigyeléseket, a bemutatott szintézismódszerrel a ZnO-gömbök mérete pontosan szabályozható a 120-2800 nm-es folyamatos tartományban, hasonlóan nagy fajlagos felülettel. A gömbök kialakulása kétlépcsős folyamatnak bizonyult: a 9-24 nm-es tartományban a ZnO részecskék kristályosodásával kezdődik, majd a prekurzor összetételének megfelelően agglomeráció és növekedés útján gömbök alakultak ki.

A fenol fotokatalitikus bontása során megállapítható, hogy a különböző prekurzorarány használatával készült ZnO-minták a tiszta prekurzorokból szintetizált mintákkal arányos aktivitást mértem. Az alkalmazott módosítások ellenére, a (200) és (100)

rácssíkok megnövekedett egymáshoz viszonyított aránya nagymértékben befolyásolja a fotokatalitikus aktivitást, és hasonló tendencia figyelhető meg, mint korábbi fejezetben tárgyalt esetekben. Az intenzitásarány változásának okaként az elsődleges kristallitok méret-anizotrópiájának tulajdonítható. Ezt a Scherrer-egyenletnek a röntgendiffrakciós adatokra való nem konvecionális alkalmazásával határoztam meg. A XRD, a PL és a fotokatalitikus bontási mérések felhasználásával ok-okozati összefüggést határoztam meg a $r_{(002)/(100)}$ és a fotokatalitikus aktivitás között korábban talált korrelációval. Ez az ok, az elektron-lyuk párok különböző rekombinációs útvonalai voltak, amelyek a (002) és (100) rácssíkoknak megfelelő kristályoldalakra jellemzőek. A nagyszámú oxigén vakanciák ,elektroncsapdaként viselkedik, és inkább az elektron-lyuk pár belső rekombinációját segíti elő, mint a katalitikus bontási folyamatban való hasznosítását.

További morfológiai módosítást értünk el szacharózból előállított széngömb-templátok alkalmazásával, a ZnO üreges gömbök előállításához két szintézismódszer esetében. A szacharózból származó CS-ek alkalmazása nem eredményezett üreges szerkezetek kialakulását, amikor szintézismódszerként kémiai impregnálást alkalmaztam. A szacharózból származó CS-eket azonban sikeresen alkalmaztam szolvotermális szintézis során, üreges ZnO-gömbök előállítására. Meghatároztam az optimális feltételeket (10:1 ZnO:CS tömegarány) a szabályos üreges gömbök előállításához. A templátok kalcinálással történő eltávolítását SEM és TEM mérésekkel voltak igazolva. A referenciaanyagok esetében a kalcinálás során alkalmazott hőmérséklet a (002) rácssík írányába való preferenciális orientáció elvesztését eredményezte. Az üreges szerkezetek esetében a preferenciális orientáció a templátok jelenléte miatt jelentősen megmaradt.

Az Au és Pt nanorészecskéket kémiai redukciós módszerrel sikeresen leválasztottam a HS-ok felületére, amit XRD, TEM, PL és DRS mérésekkel igazoltam. A ZnO morfológiája és szerkezete a nemesfémek jelenléte ellenére változatlan maradt. A kompozitok emissziós spektrumai azt mutatták, hogy a Pt fokozza a töltésszétválasztást az UV-tartományban, az Au pedig csökkenti a hibapotokon keresztüli rekombinációt.

A minták fotokatalitikus aktivitását fenol, ibuprofen és diuron UV-sugárzás során történő lebontásával vizsgáltam. A ZnO üreges gömbök legalább 70%-kal felülmúlták az előzetesen előállított referenciákat. A nemesfémek jelenléte a fotokatalitikus lebontás látszólagos sebességi állandóinak figyelemre méltó, 270%-os vagy annál nagyobb növekedését eredményezte, a használt modellszennyező anyagtól függően. Hasonló hatásfoknövekedést figyeltek meg mind az Au, mind a Pt nanorészecskék esetében. A

katalizátorok az újrafelhasználhatósági vizsgálatok során is újrafelhasználhatóak és stabilnak bizonyultak.

Az üreges ZnO-minták magasabb hatásfokát annak tulajdonítható, hogy megőrizték preferenciális orientációjukat a (002) rácssík írányában. Következésképpen a szacharózból származó széngömbök alkalmazása javította a szolvotermális módszerrel szintetizált ZnO fotokatalitikus aktivitását.

Összességében megállapítható, hogy a (002) rácssík mentén való preferenciális orientáció kulcsfontosságú szerkezeti tényező, amely előzetesen jó fotokatalitikus teljesítményt jelezhet a szerves szennyezőanyagok fotokatalitikus bontásában, ami az irodalomban is megfigyelhető, annak ellenére, hogy a ZnO-alapú fotokatalizátorokkal kapcsolatos különböző kutatások nem hangsúlyozzák ezt a szempontot.

8. Acknowledgments

I want to thank Prof. Zoltán Kónya. He made it possible for me to carry out my research work in the Department of Applied and Environmental Chemistry. The invaluable knowledge and perspectives were shared and shown by the lecturers at the University of Szeged.

I am indebted to Prof. Klára Hernádi that she offered me the opportunity to work in her research group, for all her guidance, and patience, and that she has given me a free hand in experimenting with the various ideas during my research and occasionally learning from my mistakes.

I am very grateful to Dr. Zsolt Pap for his overwhelming support, professional advice, guidance, and open-mindedness toward exploring. I want to thank Dr. Gyulavári Tamás for all his shared experiences regarding the topic of shape-controlled synthesis.

I want to give special thanks to my colleagues from the Research Group of Environmental Chemistry and Materials for Environmental Applications (Babeș-Bolyai University) for their unending support, cooperation, and friendship.

I would like to dedicate the presented results to a former student of the University of Szeged, Molnár Csanád, whom I got the opportunity to work with during my research. His tragic passing obstructed him from fully realizing his potential. His exceptional way of asking the right questions has greatly influenced the research in the right direction.

I am grateful to Sándor Krisztina, Pál Sándor and The City Library of Székelyudvarhely (Romania) for the binding of the dissertation.

I am indebted to my wife, family, and friends, as without their support making this work would not have been possible.

9. References

[1]   C.H. Kuan, C.H. Tu, Lifetime of excess electron–hole pairs measured with white noise performance of the photocurrent, J. Appl. Phys. 87 (2000) 1836–1840. https://doi.org/10.1063/1.372099.

[2]   V. Diesen, M. Jonsson, Formation of H2O2 in TiO2 Photocatalysis of Oxygenated and Deoxygenated Aqueous Systems: A Probe for Photocatalytically Produced Hydroxyl Radicals, J. Phys. Chem. C. 118 (2014) 10083–10087. https://doi.org/10.1021/jp500315u.

[3]   H.R. Yousefi, B. Hashemi, A. Mirzaei, H. Roshan, M.H. Sheikhi, Effect of Ag on the ZnO nanoparticles properties as an ethanol vapor sensor, Mater. Sci. Semicond. Process. 117 (2020) 105172. https://doi.org/10.1016/j.mssp.2020.105172.

[4]   J. Zhang, J. Liu, Q. Peng, X. Wang, Y. Li, Nearly monodisperse Cu2O and CuO nanospheres: Preparation and applications for sensitive gas sensors, Chem. Mater. 18 (2006) 867–871. https://doi.org/10.1021/cm052256f.

[5]   H.-J. Le, D. Van Dao, Y.-T. Yu, Superfast and efficient hydrogen gas sensor using PdAualloy@ZnO core–shell nanoparticles, J. Mater. Chem. A. 8 (2020) 12968–12974. https://doi.org/10.1039/D0TA03552A.

[6]   J. Liu, L. Zhang, J. Fan, B. Zhu, J. Yu, Triethylamine gas sensor based on Pt-functionalized hierarchical ZnO microspheres, Sensors Actuators B Chem. 331 (2021) 129425. https://doi.org/10.1016/j.snb.2020.129425.

[7]   M. Modares, S. Alijani, B. Nasernejad, NOx photocatalytic degradation over ZnO–CdS heterostructure composite under visible light irradiation, Res. Chem. Intermed. 48 (2022) 1831–1845. https://doi.org/10.1007/s11164-022-04705-w.

[8]   V.-H. Nguyen, B.-S. Nguyen, C.-W. Huang, T.-T. Le, C.C. Nguyen, T.T. Nhi Le, D. Heo, Q.V. Ly, Q.T. Trinh, M. Shokouhimehr, C. Xia, S.S. Lam, D.-V.N. Vo, S.Y. Kim, Q. Van Le, Photocatalytic NOx abatement: Recent advances and emerging trends in the development of photocatalysts, J. Clean. Prod. 270 (2020) 121912. https://doi.org/10.1016/j.jclepro.2020.121912.

[9]   A. Pastor, J. Balbuena, M. Cruz-Yusta, I. Pavlovic, L. Sánchez, ZnO on rice husk: A sustainable photocatalyst for urban air purification, Chem. Eng. J. 368 (2019) 659–667. https://doi.org/10.1016/j.cej.2019.03.012.

[10]   S. Barthwal, S. Barthwal, B. Singh, N. Bahadur Singh, Multifunctional and fluorine-free superhydrophobic composite coating based on PDMS modified MWCNTs/ZnO

with self-cleaning, oil-water separation, and flame retardant properties, Colloids Surfaces A Physicochem. Eng. Asp. 597 (2020) 124776. https://doi.org/10.1016/j.colsurfa.2020.124776.

[11] S. Nundy, A. Ghosh, A. Tahir, T.K. Mallick, Role of Hafnium Doping on Wetting Transition Tuning the Wettability Properties of ZnO and Doped Thin Films: Self-Cleaning Coating for Solar Application, ACS Appl. Mater. Interfaces. 13 (2021) 25540–25552. https://doi.org/10.1021/acsami.1c04973.

[12] D. Upadhaya, D. Dhar Purkayastha, Self-cleaning activity of CuO/ZnO heterostructure: A synergy of photocatalysis and hydrophilicity, J. Taiwan Inst. Chem. Eng. 132 (2022) 104216. https://doi.org/10.1016/j.jtice.2022.104216.

[13] S. Nundy, A. Ghosh, T.K. Mallick, Hydrophilic and Superhydrophilic Self-Cleaning Coatings by Morphologically Varying ZnO Microstructures for Photovoltaic and Glazing Applications, ACS Omega. 5 (2020) 1033–1039. https://doi.org/10.1021/acsomega.9b02758.

[14] L. Zhang, Y. He, P. Luo, L. Ma, Y. Fan, S. Zhang, H. Shi, S. Li, Y. Nie, A heterostructured PPy/ZnO layer assembled on a PAN nanofibrous membrane with robust visible-light-induced self-cleaning properties for highly efficient water purification with fast separation flux, J. Mater. Chem. A. 8 (2020) 4483–4493. https://doi.org/10.1039/D0TA00207K.

[15] A. Salam, T. Hassan, T. Jabri, S. Riaz, A. Khan, K.M. Iqbal, S.U. Khan, M. Wasim, M.R. Shah, M.Q. Khan, I.-S. Kim, Electrospun Nanofiber-Based Viroblock/ZnO/PAN Hybrid Antiviral Nanocomposite for Personal Protective Applications, Nanomater. . 11 (2021). https://doi.org/10.3390/nano11092208.

[16] B. Abebe, E.A. Zereffa, A. Tadesse, H.C.A. Murthy, A Review on Enhancing the Antibacterial Activity of ZnO: Mechanisms and Microscopic Investigation, Nanoscale Res. Lett. 15 (2020) 190. https://doi.org/10.1186/s11671-020-03418-6.

[17] S. Karagoz, N.B. Kiremitler, G. Sarp, S. Pekdemir, S. Salem, A.G. Goksu, M.S. Onses, I. Sozdutmaz, E. Sahmetlioglu, E.S. Ozkara, A. Ceylan, E. Yilmaz, Antibacterial, Antiviral, and Self-Cleaning Mats with Sensing Capabilities Based on Electrospun Nanofibers Decorated with ZnO Nanorods and Ag Nanoparticles for Protective Clothing Applications, ACS Appl. Mater. Interfaces. 13 (2021) 5678–5690. https://doi.org/10.1021/acsami.0c15606.

[18] Y. Xie, X. Qu, J. Li, D. Li, W. Wei, D. Hui, Q. Zhang, F. Meng, H. Yin, X. Xu, Y.

Wang, L. Wang, Z. Zhou, Ultrafast physical bacterial inactivation and photocatalytic self-cleaning of ZnO nanoarrays for rapid and sustainable bactericidal applications, Sci. Total Environ. 738 (2020) 139714. https://doi.org/10.1016/j.scitotenv.2020.139714.

[19] C. Gambarotti, Semiconductors in Organic Photosynthesis, in: L. Melone (Ed.), IntechOpen, Rijeka, 2012: p. Ch. 5. https://doi.org/10.5772/28076.

[20] A. Henríquez, H.D. Mansilla, A. Martínez-de la Cruz, L. Cornejo-Ponce, E. Schott, D. Contreras, Selective Oxofunctionalization of Cyclohexene over Titanium Dioxide-Based and Bismuth Oxyhalide Photocatalysts by Visible Light Irradiation, Catal. . 10 (2020). https://doi.org/10.3390/catal10121448.

[21] T.H. AlAbdulaal, M. AlShadidi, M.S.A. Hussien, V. Ganesh, A. Bouzidi, H. Algarni, H.Y. Zahran, M.S. Abdel-wahab, I.S. Yahia, D. Elfiky, M. Jalalah, F.A. Harraz, M.S. Al-Assiri, One-pot synthesis of multifunctionalized Nd2O3 dispersed ZnO nanocomposites for enhancing electrical, optical, and photocatalytic applications, J. Mater. Res. Technol. 19 (2022) 967–988. https://doi.org/10.1016/j.jmrt.2022.05.057.

[22] T. AlAbdulaal, M. AlShadidi, M. Hussien, V. Ganesh, A.-F. Bouzidi, S. Rafique, H. Algarni, H. Zahran, M. Abdel-wahab, I. Yahia, Multifunctional and smart Er2O3–ZnO nanocomposites for electronic ceramic varistors and visible light degradation of wastewater treatment, Environ. Sci. Pollut. Res. 29 (2022) 19109–19131. https://doi.org/10.1007/s11356-021-16754-6.

[23] A. Aljaafari, A. Sedky, Influence of Fine Crystal Percentage on the Electrical Properties of ZnO Ceramic-Based Varistors, Cryst. . 10 (2020). https://doi.org/10.3390/cryst10080681.

[24] T.H. AlAbdulaal, M. AlShadidi, M.S.A. Hussien, G. Vanga, A. Bouzidi, S. Rafique, H. Algarni, H.Y. Zahran, M.S. Abdel-wahab, I.S. Yahia, Enhancing the electrical, optical, and structure morphology using Pr2O3-ZnO nanocomposites: Towards electronic varistors and environmental photocatalytic activity, J. Photochem. Photobiol. A Chem. 418 (2021) 113399. https://doi.org/10.1016/j.jphotochem.2021.113399.

[25] F. Urban, M. Passacantando, F. Giubileo, L. Iemmo, A. Di Bartolomeo, Transport and Field Emission Properties of MoS2 Bilayers, Nanomater. . 8 (2018). https://doi.org/10.3390/nano8030151.

[26] A. George, P. Kumari, N. Soin, S.S. Roy, J.A. McLaughlin, Microstructure and field

emission characteristics of ZnO nanoneedles grown by physical vapor deposition, Mater. Chem. Phys. 123 (2010) 634–638. https://doi.org/10.1016/j.matchemphys.2010.05.029.

[27]   C.J. Lee, T.J. Lee, S.C. Lyu, Y. Zhang, H. Ruh, H.J. Lee, Field emission from well-aligned zinc oxide nanowires grown at low temperature, Appl. Phys. Lett. 81 (2002) 3648–3650. https://doi.org/10.1063/1.1518810.

[28]   P. Du, X. Huang, J.S. Yu, Facile synthesis of bifunctional Eu3+-activated NaBiF4 red-emitting nanoparticles for simultaneous white light-emitting diodes and field emission displays, Chem. Eng. J. 337 (2018) 91–100. https://doi.org/10.1016/j.cej.2017.12.063.

[29]   X. Liu, K. Pan, W. Li, D. Hu, S. Liu, Y. Wang, Optical and gas sensing properties of Al-doped ZnO transparent conducting films prepared by sol–gel method under different heat treatments, Ceram. Int. 40 (2014) 9931–9939. https://doi.org/10.1016/j.ceramint.2014.02.090.

[30]   L. Luo, M.D. Rossell, D. Xie, R. Erni, M. Niederberger, Microwave-Assisted Nonaqueous Sol–Gel Synthesis: From Al:ZnO Nanoparticles to Transparent Conducting Films, ACS Sustain. Chem. Eng. 1 (2013) 152–160. https://doi.org/10.1021/sc300073d.

[31]   M.-C. Jun, S.-U. Park, J.-H. Koh, Comparative studies of Al-doped ZnO and Ga-doped ZnO transparent conducting oxide thin films, Nanoscale Res. Lett. 7 (2012) 639. https://doi.org/10.1186/1556-276X-7-639.

[32]   Ü. Özgür, D. Hofstetter, H. Morkoç, ZnO Devices and Applications: A Review of Current Status and Future Prospects, Proc. IEEE. 98 (2010) 1255–1268. https://doi.org/10.1109/JPROC.2010.2044550.

[33]   D. Panda, T.-Y. Tseng, One-dimensional ZnO nanostructures: fabrication, optoelectronic properties, and device applications, J. Mater. Sci. 48 (2013) 6849–6877. https://doi.org/10.1007/s10853-013-7541-0.

[34]   S. Singh, P. Chakrabarti, Comparison of the structural and optical properties of ZnO thin films deposited by three different methods for optoelectronic applications, Superlattices Microstruct. 64 (2013) 283–293. https://doi.org/10.1016/j.spmi.2013.09.031.

[35]   H. Jeong, D.J. Park, H.S. Lee, Y.H. Ko, J.S. Yu, S.-B. Choi, D.-S. Lee, E.-K. Suh, M.S. Jeong, Light-extraction enhancement of a GaN-based LED covered with ZnO

nanorod arrays, Nanoscale. 6 (2014) 4371–4378. https://doi.org/10.1039/C3NR06584G.

[36] R. Bao, C. Wang, L. Dong, R. Yu, K. Zhao, Z.L. Wang, C. Pan, Flexible and Controllable Piezo-Phototronic Pressure Mapping Sensor Matrix by ZnO NW/p-Polymer LED Array, Adv. Funct. Mater. 25 (2015) 2884–2891. https://doi.org/10.1002/adfm.201500801.

[37] C. Wang, R. Bao, K. Zhao, T. Zhang, L. Dong, C. Pan, Enhanced emission intensity of vertical aligned flexible ZnO nanowire/p-polymer hybridized LED array by piezo-phototronic effect, Nano Energy. 14 (2015) 364–371. https://doi.org/10.1016/j.nanoen.2014.11.033.

[38] Y.-H. Lin, H. Faber, K. Zhao, Q. Wang, A. Amassian, M. McLachlan, T.D. Anthopoulos, High-Performance ZnO Transistors Processed Via an Aqueous Carbon-Free Metal Oxide Precursor Route at Temperatures Between 80–180 °C, Adv. Mater. 25 (2013) 4340–4346. https://doi.org/10.1002/adma.201301622.

[39] H. Bong, W.H. Lee, D.Y. Lee, B.J. Kim, J.H. Cho, K. Cho, High-mobility low-temperature ZnO transistors with low-voltage operation, Appl. Phys. Lett. 96 (2010) 2008–2011. https://doi.org/10.1063/1.3428357.

[40] Y.-H. Lin, S.R. Thomas, H. Faber, R. Li, M.A. McLachlan, P.A. Patsalas, T.D. Anthopoulos, Al-Doped ZnO Transistors Processed from Solution at 120 °C, Adv. Electron. Mater. 2 (2016) 1600070. https://doi.org/10.1002/aelm.201600070.

[41] B. Qi, S. Ólafsson, H.P. Gíslason, Vacancy defect-induced d0 ferromagnetism in undoped ZnO nanostructures: Controversial origin and challenges, Prog. Mater. Sci. 90 (2017) 45–74. https://doi.org/10.1016/j.pmatsci.2017.07.002.

[42] K. Jeyasubramanian, R. V William, P. Thiruramanathan, G.S. Hikku, M. Vimal Kumar, B. Ashima, P. Veluswamy, H. Ikeda, Dielectric and magnetic properties of nanoporous nickel doped zinc oxide for spintronic applications, J. Magn. Magn. Mater. 485 (2019) 27–35. https://doi.org/10.1016/j.jmmm.2019.04.032.

[43] P. Norouzzadeh, K. Mabhouti, M.M. Golzan, R. Naderali, Investigation of structural, morphological and optical characteristics of Mn substituted Al-doped ZnO NPs: A Urbach energy and Kramers-Kronig study, Optik (Stuttg). 204 (2020) 164227. https://doi.org/10.1016/j.ijleo.2020.164227.

[44] Gyulavári T. Zs., Enhancement of photocatalytic activity of titanium dioxide-based photocatalysts, Ph.D. Thesis, Univ. Szeged, Szeged, Hungary. (2020).

[45]   M. Mosca, R. Macaluso, F. Caruso, V. Lo Muzzo, C. Calì, The p-type doping of ZnO: Mirage or reality?, in: 2014: pp. 245–282.

[46]   K. Lott, S. Shinkarenko, T. Kirsanova, L. Türn, E. Gorohova, A. Grebennik, A. Vishnjakov, Zinc nonstoichiometry in ZnO, Solid State Ionics. 173 (2004) 29–33. https://doi.org/10.1016/j.ssi.2004.07.048.

[47]   A. Asadov, W. Gao, Z. Li, J. Lee, M. Hodgson, Correlation between structural and electrical properties of ZnO thin films, Thin Solid Films. 476 (2005) 201–205. https://doi.org/10.1016/j.tsf.2004.09.038.

[48]   Ü. Özgür, V. Avrutin, H. Morkoç, Chapter 16 - Zinc Oxide Materials and Devices Grown by Molecular Beam Epitaxy, in: M.B.T.-M.B.E. (Second E. Henini (Ed.), Elsevier, 2018: pp. 343–375. https://doi.org/10.1016/B978-0-12-812136-8.00016-5.

[49]   S. Majumder, S. Chatterjee, P. Basnet, J. Mukherjee, ZnO based nanomaterials for photocatalytic degradation of aqueous pharmaceutical waste solutions – A contemporary review, Environ. Nanotechnology, Monit. Manag. 14 (2020) 100386. https://doi.org/10.1016/j.enmm.2020.100386.

[50]   N. Nesakumar, B.L. Ramachandra, S. Sethuraman, U.M. Krishnan, J.B.B. Rayappan, Evaluation of Inhibition Efficiency for the Detection of Captan, 2,3,7,8-Tetrachlorodibenzodioxin, Pentachlorophenol and Carbosulfan in Water: An Electrochemical Approach, Bull. Environ. Contam. Toxicol. 96 (2016) 217–223. https://doi.org/10.1007/s00128-015-1705-3.

[51]   M. Samadi, M. Zirak, A. Naseri, M. Kheirabadi, M. Ebrahimi, A.Z. Moshfegh, Design and tailoring of one-dimensional ZnO nanomaterials for photocatalytic degradation of organic dyes: a review, Res. Chem. Intermed. 45 (2019) 2197–2254. https://doi.org/10.1007/s11164-018-03729-5.

[52]   S.S. Shinde, P.S. Shinde, C.H. Bhosale, K.Y. Rajpure, Zinc oxide mediated heterogeneous photocatalytic degradation of organic species under solar radiation, J. Photochem. Photobiol. B Biol. 104 (2011) 425–433. https://doi.org/10.1016/j.jphotobiol.2011.04.010.

[53]   H. Benhebal, M. Chaib, T. Salmon, J. Geens, A. Leonard, S.D. Lambert, M. Crine, B. Heinrichs, Photocatalytic degradation of phenol and benzoic acid using zinc oxide powders prepared by the sol–gel process, Alexandria Eng. J. 52 (2013) 517–523. https://doi.org/10.1016/j.aej.2013.04.005.

[54]   M.M. Ba-Abbad, A.A.H. Kadhum, A.B. Mohamad, M.S. Takriff, K. Sopian,

Photocatalytic degradation of chlorophenols under direct solar radiation in the presence of ZnO catalyst, Res. Chem. Intermed. 39 (2013) 1981–1996. https://doi.org/10.1007/s11164-012-0731-6.

[55]   F. Hosseini, A. Kasaeian, F. Pourfayaz, M. Sheikhpour, D. Wen, Novel ZnO-Ag/MWCNT nanocomposite for the photocatalytic degradation of phenol, Mater. Sci. Semicond. Process. 83 (2018) 175–185. https://doi.org/10.1016/j.mssp.2018.04.042.

[56]   R. Saleh, N.F. Djaja, UV light photocatalytic degradation of organic dyes with Fe-doped ZnO nanoparticles, Superlattices Microstruct. 74 (2014) 217–233. https://doi.org/10.1016/j.spmi.2014.06.013.

[57]   X. Chen, Z. Wu, D. Liu, Z. Gao, Preparation of ZnO Photocatalyst for the Efficient and Rapid Photocatalytic Degradation of Azo Dyes, Nanoscale Res. Lett. 12 (2017) 143. https://doi.org/10.1186/s11671-017-1904-4.

[58]   F. Liu, Y.H. Leung, A.B. Djurišić, A.M.C. Ng, W.K. Chan, Native Defects in ZnO: Effect on Dye Adsorption and Photocatalytic Degradation, J. Phys. Chem. C. 117 (2013) 12218–12228. https://doi.org/10.1021/jp403478q.

[59]   Q.I. Rahman, M. Ahmad, S.K. Misra, M. Lohani, Effective photocatalytic degradation of rhodamine B dye by ZnO nanoparticles, Mater. Lett. 91 (2013) 170–174. https://doi.org/10.1016/j.matlet.2012.09.044.

[60]   P. Veerakumar, A. Sangili, K. Saranya, A. Pandikumar, K.-C. Lin, Palladium and silver nanoparticles embedded on zinc oxide nanostars for photocatalytic degradation of pesticides and herbicides, Chem. Eng. J. 410 (2021) 128434. https://doi.org/10.1016/j.cej.2021.128434.

[61]   S.H. Khan, B. Pathak, Zinc oxide based photocatalytic degradation of persistent pesticides: A comprehensive review, Environ. Nanotechnology, Monit. Manag. 13 (2020) 100290. https://doi.org/10.1016/j.enmm.2020.100290.

[62]   J. Macan, M. Ivanko, I. Bukovčan, I. Grčić, A. Gajović, Stable hierarchical ZnO structures for photocatalytic degradation of 2,5-dihydroxybenzoic acid, Mater. Sci. Semicond. Process. 97 (2019) 48–55. https://doi.org/10.1016/j.mssp.2019.03.006.

[63]   R. Sabouni, H. Gomaa, Photocatalytic degradation of pharmaceutical micro-pollutants using ZnO, Environ. Sci. Pollut. Res. 26 (2019) 5372–5380. https://doi.org/10.1007/s11356-018-4051-2.

[64]   M. Tanveer, G.T. Guyer, G. Abbas, Photocatalytic degradation of ibuprofen in water using TiO2 and ZnO under artificial UV and solar irradiation, Water Environ. Res. 91

(2019) 822–829. https://doi.org/10.1002/wer.1104.

[65]   M.R. Hernández, A. de León Santillán, E. de Casas Ortiz, S.F. Tavizón, I. Moggio, E. Arias, C.A. Gallardo-Vega, J.A. Mercado Silva, E.D. Barriga-Castro, Hollow ZnO microspheres functionalized with electrochemical graphene oxide for the photodegradation of salicylic acid, RSC Adv. 9 (2019) 6965–6972. https://doi.org/10.1039/C8RA10113B.

[66]   V.H.-T. Thi, B.-K. Lee, Effective photocatalytic degradation of paracetamol using La-doped ZnO photocatalyst under visible light irradiation, Mater. Res. Bull. 96 (2017) 171–182. https://doi.org/10.1016/j.materresbull.2017.04.028.

[67]   S. Ahmed, M.G. Rasul, W.N. Martens, R. Brown, M.A. Hashib, Heterogeneous photocatalytic degradation of phenols in wastewater: A review on current status and developments, Desalination. 261 (2010) 3–18. https://doi.org/10.1016/j.desal.2010.04.062.

[68]   C.D. Chriswell, R.C. Chang, J.S. Fritz, Chromatographic determination of phenols in water, Anal. Chem. 47 (1975) 1325–1329. https://doi.org/10.1021/ac60358a005.

[69]   C. Tschersich, A. Murawski, G. Schwedler, E. Rucic, R.K. Moos, M. Kasper-Sonnenberg, H.M. Koch, T. Brüning, M. Kolossa-Gehring, Bisphenol A and six other environmental phenols in urine of children and adolescents in Germany – human biomonitoring results of the German Environmental Survey 2014–2017 (GerES V), Sci. Total Environ. 763 (2021) 144615. https://doi.org/10.1016/j.scitotenv.2020.144615.

[70]   T. Chen, Y. Zheng, J.M. Lin, G. Chen, Study on the Photocatalytic Degradation of Methyl Orange in Water Using Ag/ZnO as Catalyst by Liquid Chromatography Electrospray Ionization Ion-Trap Mass Spectrometry, J. Am. Soc. Mass Spectrom. (2008). https://doi.org/10.1016/j.jasms.2008.03.008.

[71]   B. Réti, G.I. Kiss, T. Gyulavári, K. Baan, K. Magyari, K. Hernadi, Carbon sphere templates for TiO2 hollow structures: Preparation, characterization and photocatalytic activity, Catal. Today. 284 (2017) 160–168. https://doi.org/10.1016/j.cattod.2016.11.038.

[72]   A. Khataee, R.D.C. Soltani, Y. Hanifehpour, M. Safarpour, H. Gholipour Ranjbar, S.W. Joo, Synthesis and characterization of dysprosium-doped ZnO nanoparticles for photocatalysis of a textile dye under visible light irradiation, Ind. Eng. Chem. Res. 53 (2014) 1924–1932. https://doi.org/10.1021/ie402743u.

[73] G. Kovács, S. Fodor, A. Vulpoi, K. Schrantz, A. Dombi, K. Hernádi, V. Danciu, Z. Pap, L. Baia, Polyhedral Pt vs. spherical Pt nanoparticles on commercial titanias: Is shape tailoring a guarantee of achieving high activity?, J. Catal. 325 (2015) 156–167. https://doi.org/10.1016/j.jcat.2015.02.008.

[74] M. Huang, Y. Yan, W. Feng, S. Weng, Z. Zheng, X. Fu, P. Liu, Controllable tuning various ratios of ZnO polar facets by crystal seed-assisted growth and their photocatalytic activity, Cryst. Growth Des. 14 (2014) 2179–2186. https://doi.org/10.1021/cg401676r.

[75] S.M. Mousavi, A.R. Mahjoub, R. Abazari, Green synthesis of ZnO hollow sphere nanostructures by a facile route at room temperature with efficient photocatalytic dye degradation properties, RSC Adv. 5 (2015) 107378–107388. https://doi.org/10.1039/c5ra19507a.

[76] M. Huang, S. Weng, B. Wang, J. Hu, X. Fu, P. Liu, Various facet tunable ZnO crystals by a scalable solvothermal synthesis and their facet-dependent photocatalytic activities, J. Phys. Chem. C. 118 (2014) 25434–25440. https://doi.org/10.1021/jp5072567.

[77] Y. Qu, X. Xu, R. Huang, W. Qi, R. Su, Z. He, Enhanced photocatalytic degradation of antibiotics in water over functionalized N,S-doped carbon quantum dots embedded ZnO nanoflowers under sunlight irradiation, Chem. Eng. J. 382 (2020) 123016. https://doi.org/10.1016/j.cej.2019.123016.

[78] T.S. Anirudhan, F. Shainy, A. Manasa Mohan, Fabrication of zinc oxide nanorod incorporated carboxylic graphene/polyaniline composite and its photocatalytic activity for the effective degradation of diuron from aqueous solutions, Sol. Energy. 171 (2018) 534–546. https://doi.org/10.1016/j.solener.2018.06.111.

[79] R. Liu, D. Zuo, C. Tan, Construction of C/ZnO/BiOI photocatalyst for enhanced degradation of carbaryl: Characterization, performance and mechanism, J. Alloys Compd. 911 (2022) 165023. https://doi.org/10.1016/j.jallcom.2022.165023.

[80] T. Gyulavári, V. Márta, Z. Kovács, K. Magyari, Z. Kása, G. Veréb, Z. Pap, K. Hernadi, Immobilization of highly active titanium dioxide and zinc oxide hollow spheres on ceramic paper and their applicability for photocatalytic water treatment, J. Photochem. Photobiol. A Chem. 427 (2022) 113791. https://doi.org/10.1016/j.jphotochem.2022.113791.

[81] M. Samadi, M. Zirak, A. Naseri, E. Khorashadizade, A.Z. Moshfegh, Recent progress

on doped ZnO nanostructures for visible-light photocatalysis, Thin Solid Films. 605 (2016) 2–19. https://doi.org/10.1016/j.tsf.2015.12.064.

[82]   W. Li, G. Wang, C. Chen, J. Liao, Z. Li, Enhanced Visible Light Photocatalytic Activity of ZnO Nanowires Doped with Mn2+ and Co2+ Ions, Nanomater. . 7 (2017). https://doi.org/10.3390/nano7010020.

[83]   J. Lahiri, M. Batzill, Surface Functionalization of ZnO Photocatalysts with Monolayer ZnS, J. Phys. Chem. C. 112 (2008) 4304–4307. https://doi.org/10.1021/jp7114109.

[84]   R.Y. Hong, J.H. Li, L.L. Chen, D.Q. Liu, H.Z. Li, Y. Zheng, J. Ding, Synthesis, surface modification and photocatalytic property of ZnO nanoparticles, Powder Technol. 189 (2009) 426–432. https://doi.org/10.1016/j.powtec.2008.07.004.

[85]   B. Liu, H. Yang, S. Liu, Photogenerated Charge Separation between Polar Crystal Facets Under a Spontaneous Electric Field, Adv. Opt. Mater. 9 (2021) 2001898. https://doi.org/10.1002/adom.202001898.

[86]   Z. Wang, H. Wang, X. Wang, X. Chen, Y. Yu, W. Dai, X. Fu, M. Anpo, Correlation between Photocorrosion of ZnO and Lattice Relaxation Induced by Its Surface Vacancies, J. Phys. Chem. C. 125 (2021) 3242–3255. https://doi.org/10.1021/acs.jpcc.0c11260.

[87]   Z. Wang, B. Wen, Q. Hao, L.-M. Liu, C. Zhou, X. Mao, X. Lang, W.-J. Yin, D. Dai, A. Selloni, X. Yang, Localized Excitation of Ti3+ Ions in the Photoabsorption and Photocatalytic Activity of Reduced Rutile TiO2, J. Am. Chem. Soc. 137 (2015) 9146–9152. https://doi.org/10.1021/jacs.5b04483.

[88]   M.D. McCluskey, S.J. Jokela, Defects in ZnO, J. Appl. Phys. 106 (2009) 71101. https://doi.org/10.1063/1.3216464.

[89]   L. Mädler, W.J. Stark, S.E. Pratsinis, Rapid synthesis of stable ZnO quantum dots, J. Appl. Phys. 92 (2002) 6537–6540. https://doi.org/10.1063/1.1518132.

[90]   X. Bai, B. Sun, X. Wang, T. Zhang, Q. Hao, B.-J. Ni, R. Zong, Z. Zhang, X. Zhang, H. Li, Defective crystal plane-oriented induced lattice polarization for the photocatalytic enhancement of ZnO, CrystEngComm. 22 (2020) 2709–2717. https://doi.org/10.1039/C9CE01966A.

[91]   K.D. Ngwashi, B.M.R. Cross, S. Paul, P.M. Andrian, A. Devi, High Mobility ZnO thin film transistors using the novel deposition of high-k dielectrics, MRS Online Proc. Libr. 1315 (2011) 618. https://doi.org/10.1557/opl.2011.721.

[92]   M. Machovsky, I. Kuritka, J. Sedlak, M. Pastorek, Hexagonal ZnO porous plates

prepared from microwave synthesized layered zinc hydroxide sulphate via thermal decomposition, Mater. Res. Bull. 48 (2013) 4002–4007. https://doi.org/10.1016/j.materresbull.2013.06.018.

[93] A. Sari, G. Stefani, G. Dra, Solvothermal synthesis of zinc oxide microspheres, 652 (2015) 91–99. https://doi.org/10.1016/j.jallcom.2015.08.200.

[94] Y. Sun, L. Chen, Y. Bao, Y. Zhang, J. Wang, M. Fu, J. Wu, D. Ye, The Applications of Morphology Controlled ZnO in Catalysis, Catal. . 6 (2016). https://doi.org/10.3390/catal6120188.

[95] A. Aboulaich, L. Balan, J. Ghanbaja, G. Medjahdi, C. Merlin, R. Schneider, Aqueous Route to Biocompatible ZnSe:Mn/ZnO Core/Shell Quantum Dots Using 1-Thioglycerol As Stabilizer, Chem. Mater. 23 (2011) 3706–3713. https://doi.org/10.1021/cm2012928.

[96] D. Vanmaekelbergh, L.K. van Vugt, ZnO nanowire lasers, Nanoscale. 3 (2011) 2783–2800. https://doi.org/10.1039/C1NR00013F.

[97] L. Lang, D. Wu, Z. Xu, Controllable fabrication of TiO2 1D-nano/micro structures: Solid, hollow, and tube-in-tube fibers by electrospinning and the photocatalytic performance, Chem. - A Eur. J. 18 (2012) 10661–10668. https://doi.org/10.1002/chem.201200378.

[98] J. Yan, G. Wu, N. Guan, L. Li, Z. Li, X. Cao, Understanding the effect of surface/bulk defects on the photocatalytic activity of TiO2: Anatase versus rutile, Phys. Chem. Chem. Phys. 15 (2013) 10978–10988. https://doi.org/10.1039/c3cp50927c.

[99] M. Maeng, S. Choi, N.K. Shahi, S. Dockko, Experimental approaches for identifying the impact of enhanced flotation technology using hollow microspheres, J. Environ. Manage. 253 (2020) 109690. https://doi.org/10.1016/j.jenvman.2019.109690.

[100] O. Friedl, C. Motz, H. Peterlik, S. Puchegger, N. Reger, R. Pippan, Experimental investigation of mechanical properties of metallic hollow sphere structures, Metall. Mater. Trans. B Process Metall. Mater. Process. Sci. 39 (2008) 135–146. https://doi.org/10.1007/s11663-007-9098-2.

[101] N. Parveen, Z. Khan, S.A. Ansari, S. Park, S.T. Senthilkumar, Y. Kim, H. Ko, M.H. Cho, Feasibility of using hollow double walled Mn2O3 nanocubes for hybrid Na-air battery, Chem. Eng. J. 360 (2019) 415–422. https://doi.org/10.1016/j.cej.2018.11.228.

[102] L. Zhou, H. Xu, H. Zhang, J. Yang, S.B. Hartono, K. Qian, J. Zou, C. Yu, Cheap and

scalable synthesis of α-Fe2O3 multi-shelled hollow spheres as high-performance anode materials for lithium ion batteries, Chem. Commun. 49 (2013) 8695–8697. https://doi.org/10.1039/c3cc43867h.

[103] L. Zhou, Z. Zhuang, H. Zhao, M. Lin, D. Zhao, L. Mai, Intricate Hollow Structures: Controlled Synthesis and Applications in Energy Storage and Conversion, Adv. Mater. 29 (2017). https://doi.org/10.1002/adma.201602914.

[104] T. Gyulavári, K. Kovács, Z. Kovács, E. Bárdos, G. Kovács, K. Baán, K. Magyari, G. Veréb, Z. Pap, K. Hernadi, Preparation and characterization of noble metal modified titanium dioxide hollow spheres – new insights concerning the light trapping efficiency, Appl. Surf. Sci. 534 (2020) 147327. https://doi.org/10.1016/j.apsusc.2020.147327.

[105] H.A. Borbón-Nuñez, D. Dominguez, F. Muñoz-Muñoz, J. Lopez, J. Romo-Herrera, G. Soto, H. Tiznado, Fabrication of hollow TiO2 nanotubes through atomic layer deposition and MWCNT templates, Powder Technol. 308 (2017) 249–257. https://doi.org/10.1016/j.powtec.2016.12.001.

[106] Z. Lou, Y. Wang, Y. Yang, Y. Wang, C. Qin, R. Liang, X. Chen, Z. Ye, L. Zhu, Carbon sphere template derived hollow nanostructure for photocatalysis and gas sensing, Nanomaterials. 10 (2020) 19–21. https://doi.org/10.3390/nano10020378.

[107] P. Song, Q. Wang, Z. Yang, Acetone sensing characteristics of ZnO hollow spheres prepared by one-pot hydrothermal reaction, Mater. Lett. 86 (2012) 168–170. https://doi.org/10.1016/j.matlet.2012.07.058.

[108] C. Jin, K. Zhu, G. Peterson, Z. Jian, G. Xu, Y. Wei, C. Ge, J. Li, Morphology Dependent Photocatalytic Properties of ZnO Nanostructures Prepared by a Carbon-Sphere Template Method, J. Nanosci. Nanotechnol. 18 (2018) 5234–5241. https://doi.org/10.1166/jnn.2018.15471.

[109] X. Wang, P. Hu, Y. Fangli, L. Yu, Preparation and characterization of ZnO hollow spheres and ZnO-carbon composite materials using colloidal carbon spheres as templates, J. Phys. Chem. C. 111 (2007) 6706–6712. https://doi.org/10.1021/jp070382w.

[110] S. Meephon, T. Rungrotmongkol, S. Puttamat, S. Praserthdam, V. Pavarajarn, Heterogeneous photocatalytic degradation of diuron on zinc oxide: Influence of surface-dependent adsorption on kinetics, degradation pathway, and toxicity of intermediates, J. Environ. Sci. (China). 84 (2019) 97–111.

https://doi.org/10.1016/j.jes.2019.04.016.

[111] Á. Kmetykó, K. Mogyorósi, P. Pusztai, T. Radu, Z. Kónya, A. Dombi, K. Hernádi, Photocatalytic H2 Evolution Using Different Commercial TiO2 Catalysts Deposited with Finely Size-Tailored Au Nanoparticles: Critical Dependence on Au Particle Size, Materials (Basel). 7 (2014) 7615–7633.

[112] K. Qi, B. Cheng, J. Yu, W. Ho, Review on the improvement of the photocatalytic and antibacterial activities of ZnO, J. Alloys Compd. 727 (2017) 792–820. https://doi.org/10.1016/j.jallcom.2017.08.142.

[113] C.B. Ong, L.Y. Ng, A.W. Mohammad, A review of ZnO nanoparticles as solar photocatalysts: Synthesis, mechanisms and applications, Renew. Sustain. Energy Rev. 81 (2018) 536–551. https://doi.org/10.1016/j.rser.2017.08.020.

[114] R. Georgekutty, M.K. Seery, S.C. Pillai, A highly efficient Ag-ZnO photocatalyst: Synthesis, properties, and mechanism, J. Phys. Chem. C. 112 (2008) 13563–13570. https://doi.org/10.1021/jp802729a.

[115] Y. Zhang, Q. Wang, J. Xu, S. Ma, Synthesis of Pd/ZnO nanocomposites with high photocatalytic performance by a solvothermal method, Appl. Surf. Sci. 258 (2012) 10104–10109. https://doi.org/10.1016/j.apsusc.2012.06.083.

[116] T.S. Tofa, F. Ye, K.L. Kunjali, J. Dutta, Enhanced visible light photodegradation of microplastic fragments with plasmonic platinum/zinc oxide nanorod photocatalysts, Catalysts. 9 (2019). https://doi.org/10.3390/catal9100819.

[117] Y. Wang, C. Yan, L. Chen, Y. Zhang, J. Yang, Controllable charge transfer in Ag-TiO2 composite structure for SERS application, Nanomaterials. 7 (2017) 1–11. https://doi.org/10.3390/nano7070159.

[118] X. Li, W. Feng, Y. Xiao, P. Sun, X. Hu, K. Shimanoe, G. Lu, N. Yamazoe, Hollow zinc oxide microspheres functionalized by Au nanoparticles for gas sensors, RSC Adv. 4 (2014) 28005–28010. https://doi.org/10.1039/c4ra02541e.

[119] Z.B. Yu, Y.P. Xie, G. Liu, G.Q. (Max) Lu, X.L. Ma, H.-M. Cheng, Self-assembled CdS/Au/ZnO heterostructure induced by surface polar charges for efficient photocatalytic hydrogen evolution, J. Mater. Chem. A. 1 (2013) 2773–2776. https://doi.org/10.1039/C3TA01476B.

[120] Z. Kovács, C. Molnár, U.L. Štangar, V.-M. Cristea, Z. Pap, K. Hernadi, L. Baia, Optimization Method of the Solvothermal Parameters Using Box–Behnken Experimental Design—The Case Study of ZnO Structural and Catalytic Tailoring,

Nanomaterials. 11 (2021). https://doi.org/10.3390/nano11051334.

[121] S.L.C. Ferreira, R.E. Bruns, H.S. Ferreira, G.D. Matos, J.M. David, G.C. Brandão, E.G.P. da Silva, L.A. Portugal, P.S. dos Reis, A.S. Souza, W.N.L. dos Santos, Box-Behnken design: An alternative for the optimization of analytical methods, Anal. Chim. Acta. 597 (2007) 179–186. https://doi.org/10.1016/j.aca.2007.07.011.

[122] H. Poortavasoly, M. Montazer, T. Harifi, Aminolysis of polyethylene terephthalate surface along with in situ synthesis and stabilizing ZnO nanoparticles using triethanolamine optimized with response surface methodology, Mater. Sci. Eng. C. 58 (2016) 495–503. https://doi.org/10.1016/j.msec.2015.08.065.

[123] J.A. Lopes Matias, I.B.T. Silva, A.O. da Silva, J.B.L. Oliveira, D. Ribeiro da Silva, M.A. Morales, (Bi13Co11)Co2O40–Co3O4 nanocomposites: Approach to different fuels in sol-gel combustion synthesis using the Box-Behnken design, Ceram. Int. 48 (2022) 481–494. https://doi.org/10.1016/j.ceramint.2021.09.124.

[124] J. Wojnarowicz, T. Chudoba, I. Koltsov, S. Gierlotka, S. Dworakowska, W. Lojkowski, Size control mechanism of ZnO nanoparticles obtained in microwave solvothermal synthesis, Nanotechnology. 29 (2018) 65601. https://doi.org/10.1088/1361-6528/aaa0ef.

[125] Z. Kovács, C. Molnár, T. Gyulavári, K. Magyari, Z.-R. Tóth, L. Baia, Z. Pap, K. Hernádi, Solvothermal synthesis of ZnO spheres: Tuning the structure and morphology from nano- to micro-meter range and its impact on their photocatalytic activity, Catal. Today. (2022). https://doi.org/10.1016/j.cattod.2022.03.004.

[126] A. Šarić, I. Despotović, G. Štefanić, G. Dražić, The Influence of Ethanolamines on the Solvothermal Synthesis of Zinc Oxide: A Combined Experimental and Theoretical Study, ChemistrySelect. 2 (2017) 10038–10049. https://doi.org/10.1002/slct.201701692.

[127] A. Gómez-Núñez, S. Alonso-Gil, C. López, P. Roura-Grabulosa, A. Vilà, From ethanolamine precursor towards ZnO—How N is released from the experimental and theoretical points of view, Nanomaterials. 9 (2019).

[128] Z. Kovács, V. Márta, T. Gyulavári, Á. Ágoston, L. Baia, Z. Pap, K. Hernadi, Noble metal modified (002)-oriented ZnO hollow spheres for the degradation of a broad range of pollutants, J. Environ. Chem. Eng. 10 (2022) 107655. https://doi.org/10.1016/j.jece.2022.107655.

[129] A. Khorsand Zak, W.H. Abd. Majid, M.E. Abrishami, R. Yousefi, X-ray analysis of

ZnO nanoparticles by Williamson-Hall and size-strain plot methods, Solid State Sci. 13 (2011) 251–256. https://doi.org/10.1016/j.solidstatesciences.2010.11.024.

[130] T.M. Project, Materials Data on ZnO by Materials Project, (2020). https://doi.org/10.17188/1196748.

[131] Y. Wang, W. Tang, L. Zhang, Crystalline Size Effects on Texture Coefficient, Electrical and Optical Properties of Sputter-deposited Ga-doped ZnO Thin Films, J. Mater. Sci. Technol. 31 (2015) 175–181. https://doi.org/10.1016/j.jmst.2014.11.009.

[132] X. Liu, L. Ye, S. Liu, Y. Li, X. Ji, Photocatalytic reduction of CO2 by ZnO micro/nanomaterials with different morphologies and ratios of {0001} facets, Sci. Rep. 6 (2016) 1–9. https://doi.org/10.1038/srep38474.

[133] T. Tasaki, T. Wada, K. Fujimoto, S. Kai, K. Ohe, T. Oshima, Y. Baba, M. Kukizaki, Degradation of methyl orange using short-wavelength UV irradiation with oxygen microbubbles, J. Hazard. Mater. 162 (2009) 1103–1110. https://doi.org/10.1016/j.jhazmat.2008.05.162.

[134] C. Pan, L. Dong, B. Qu, J. Wang, Facile synthesis and enhanced photocatalytic performance of 3D ZnO hierarchical structures, J. Nanosci. Nanotechnol. 11 (2011) 5042–5048. https://doi.org/10.1166/jnn.2011.3887.

[135] B.K. Körbahti, M.A. Rauf, Response surface methodology (RSM) analysis of photoinduced decoloration of toludine blue, Chem. Eng. J. 136 (2008) 25–30. https://doi.org/10.1016/j.cej.2007.03.007.

[136] R.S. Varga, A.J. Carpenter, Zeros of the partial sums of cos (z) and sin (z). I, Numer. Algorithms. 25 (2000) 363–375. https://doi.org/10.1023/A:1016648721367.

[137] E.P. Simonenko, N.P. Simonenko, I.A. Nagornov, A.S. Mokrushin, P.Y. Gorobtsov, I.S. Vlasov, I.A. Volkov, T. Maeder, A.A. Vasiliev, V.G. Sevastyanov, N.T. Kuznetsov, Nanocrystalline ZnO Obtained by the Thermal Decomposition of [Zn(H2O)(O2C5H7)2] in 1-Butanol: Synthesis and Testing as a Sensing Material, Russ. J. Inorg. Chem. 63 (2018) 1519–1528. https://doi.org/10.1134/S0036023618110189.

[138] R. Hayami, N. Endo, Y. Miyase, K. Yamamoto, T. Gunji, ZnO formation through decomposition of zinc bis(ethyl acetoacetate) by steaming treatment, J. Sol-Gel Sci. Technol. 91 (2019) 255–260. https://doi.org/10.1007/s10971-019-05043-x.

[139] R. Elshypany, H. Selim, K. Zakaria, A.H. Moustafa, S.A. Sadeek, S.I. Sharaa, P. Raynaud, A.A. Nada, Magnetic ZnO Crystal Nanoparticle Growth on Reduced

Graphene Oxide for Enhanced Photocatalytic Performance under Visible Light Irradiation, Mol. . 26 (2021). https://doi.org/10.3390/molecules26082269.

[140] A. Mclaren, T. Valdes-Solis, G. Li, S.C. Tsang, Shape and Size Effect of ZnO nanocrystals on Photocatalytic Activity Supporting Information, J. Am. Chem. Soc. (2009) 12540–12541. https://pubs.acs.org/doi/suppl/10.1021/ja9052703/suppl_file/ja9052703_si_001.pdf.

[141] J. Chang, E.R. Waclawik, Facet-controlled self-assembly of ZnO nanocrystals by non-hydrolytic aminolysis and their photodegradation activities, CrystEngComm. 14 (2012) 4041–4048. https://doi.org/10.1039/c2ce25154j.

[142] G. Thennarasu, A. Sivasamy, Metal ion doped semiconductor metal oxide nanosphere particles prepared by soft chemical method and its visible light photocatalytic activity in degradation of phenol, Powder Technol. 250 (2013) 1–12. https://doi.org/10.1016/j.powtec.2013.08.004.

[143] F. Kayaci, S. Vempati, C. Ozgit-Akgun, I. Donmez, N. Biyikli, T. Uyar, Transformation of polymer-ZnO core-shell nanofibers into ZnO hollow nanofibers: Intrinsic defect reorganization in ZnO and its influence on the photocatalysis, Elsevier B.V., 2015. https://doi.org/10.1016/j.apcatb.2015.04.036.

[144] J.H. Sun, S.Y. Dong, Y.K. Wang, S.P. Sun, Preparation and photocatalytic property of a novel dumbbell-shaped ZnO microcrystal photocatalyst, J. Hazard. Mater. 172 (2009) 1520–1526. https://doi.org/10.1016/j.jhazmat.2009.08.022.

[145] A. Mclaren, T. Valdes-Solis, G. Li, S.C. Tsang, Shape and Size Effects of ZnO Nanocrystals on Photocatalytic Activity, J. Am. Chem. Soc. 131 (2009) 12540–12541. https://doi.org/10.1021/ja9052703.

[146] Y. Wan, J. Li, J. Ni, C. Wang, C. Ni, H. Chen, Crystal-facet and microstructure engineering in ZnO for photocatalytic NO oxidation, J. Hazard. Mater. 435 (2022) 129073. https://doi.org/10.1016/j.jhazmat.2022.129073.

[147] P. Singh, R.K. Singh, R. Kumar, Journey of ZnO quantum dots from undoped to rare-earth and transition metal-doped and their applications, RSC Adv. 11 (2021) 2512–2545. https://doi.org/10.1039/D0RA08670C.

[148] C.F. Holder, R.E. Schaak, Tutorial on Powder X-ray Diffraction for Characterizing Nanoscale Materials, ACS Nano. 13 (2019) 7359–7365. https://doi.org/10.1021/acsnano.9b05157.

[149] A. Barnasas, N. Kanistras, A. Ntagkas, D.I. Anyfantis, A. Stamatelatos, V. Kapaklis,

N. Bouropoulos, E. Mystiridou, P. Poulopoulos, C.S. Garoufalis, S. Baskoutas, Quantum confinement effects of thin ZnO films by experiment and theory, Phys. E Low-Dimensional Syst. Nanostructures. 120 (2020) 114072. https://doi.org/10.1016/j.physe.2020.114072.

[150] R. Boppella, K. Anjaneyulu, P. Basak, S. V. Manorama, Facile synthesis of face oriented ZnO crystals: Tunable polar facets and shape induced enhanced photocatalytic performance, J. Phys. Chem. C. 117 (2013) 4597–4605. https://doi.org/10.1021/jp311443s.

[151] L. V. Trandafilović, D.J. Jovanović, X. Zhang, S. Ptasińska, M.D. Dramićanin, Enhanced photocatalytic degradation of methylene blue and methyl orange by ZnO:Eu nanoparticles, Appl. Catal. B Environ. 203 (2017) 740–752. https://doi.org/10.1016/j.apcatb.2016.10.063.

[152] A. Tiwari, I. Mondal, S. Ghosh, N. Chattopadhyay, U. Pal, Fabrication of mixed phase TiO2 heterojunction nanorods and their enhanced photoactivities, Phys. Chem. Chem. Phys. 18 (2016) 15260–15268. https://doi.org/10.1039/C6CP00486E.

[153] X. Wang, Q. Zhang, Q. Wan, G. Dai, C. Zhou, B. Zou, Controllable ZnO Architectures by Ethanolamine-Assisted Hydrothermal Reaction for Enhanced Photocatalytic Activity, J. Phys. Chem. C. 115 (2011) 2769–2775. https://doi.org/10.1021/jp1096822.

[154] J.E. Rodríguez-Paéz, A.C. Caballero, M. Villegas, C. Moure, P. Durán, J.F. Fernández, Controlled precipitation methods:Formation mechanism of ZnO nanoparticles, J. Eur. Ceram. Soc. 21 (2001) 925–930. https://doi.org/10.1016/S0955-2219(00)00283-1.

[155] Y. Inubushi, R. Takami, M. Iwasaki, H. Tada, S. Ito, Mechanism of formation of nanocrystalline ZnO particles through the reaction of [Zn(acac)2] with NaOH in EtOH, J. Colloid Interface Sci. 200 (1998) 220–227. https://doi.org/10.1006/jcis.1997.5354.

[156] S.C. Singh, Effect of oxygen injection on the size and compositional evolution of ZnO/Zn(OH)2 nanocomposite synthesized by pulsed laser ablation in distilled water, J. Nanoparticle Res. 13 (2011) 4143–4152. https://doi.org/10.1007/s11051-011-0359-2.

[157] P. Bindu, S. Thomas, Estimation of lattice strain in ZnO nanoparticles: X-ray peak profile analysis, J. Theor. Appl. Phys. 8 (2014) 123–134.

https://doi.org/10.1007/s40094-014-0141-9.

[158] R. Yogamalar, R. Srinivasan, A. Vinu, K. Ariga, A.C. Bose, X-ray peak broadening analysis in ZnO nanoparticles, Solid State Commun. 149 (2009) 1919–1923. https://doi.org/10.1016/j.ssc.2009.07.043.

[159] V. Mote, Y. Purushotham, B. Dole, Williamson-Hall analysis in estimation of lattice strain in nanometer-sized ZnO particles, J. Theor. Appl. Phys. 6 (2012) 2–9. https://doi.org/10.1186/2251-7235-6-6.

[160] B.Y. Shekunov, P. Chattopadhyay, H.H.Y. Tong, A.H.L. Chow, Particle size analysis in pharmaceutics: Principles, methods and applications, Pharm. Res. 24 (2007) 203–227. https://doi.org/10.1007/s11095-006-9146-7.

[161] A. Prakash, D. Bahadur, Chemically derived defects in zinc oxide nanocrystals and their enhanced photo-electrocatalytic activities., Phys. Chem. Chem. Phys. 16 (2014) 21429–21437. https://doi.org/10.1039/c4cp03583f.

[162] A.M. Al-Hamdi, M. Sillanpää, J. Dutta, Intermediate formation during photodegradation of phenol using lanthanum doped tin dioxide nanoparticles, Res. Chem. Intermed. 42 (2016) 3055–3069. https://doi.org/10.1007/s11164-015-2197-9.

[163] I.E. Wachs, S.P. Phivilay, C.A. Roberts, Reporting of Reactivity for Heterogeneous Photocatalysis, ACS Catal. 3 (2013) 2606–2611. https://doi.org/10.1021/cs4005979.

[164] C. Jaramillo-Páez, J.A. Navío, M.C. Hidalgo, M. Macías, High UV-photocatalytic activity of ZnO and Ag/ZnO synthesized by a facile method, Catal. Today. 284 (2017) 121–128. https://doi.org/10.1016/j.cattod.2016.11.021.

[165] J. Gupta, K.C. Barick, D. Bahadur, Defect mediated photocatalytic activity in shape-controlled ZnO nanostructures, J. Alloys Compd. 509 (2011) 6725–6730. https://doi.org/10.1016/j.jallcom.2011.03.157.

[166] C.A. Jaramillo-Páez, J.A. Navío, M.C. Hidalgo, M. Macías, ZnO and Pt-ZnO photocatalysts: Characterization and photocatalytic activity assessing by means of three substrates, Catal. Today. 313 (2018) 12–19. https://doi.org/10.1016/j.cattod.2017.12.009.

[167] E.-S. Jang, J. Won, S.-J. Hwang, J.-H. Choy, Fine Tuning of the Face Orientation of ZnO Crystals to Optimize Their Photocatalytic Activity, Adv. Mater. 18 (2006) 3309–3312. https://doi.org/10.1002/adma.200601455.

[168] Z. Kovács, C. Molnár, U.L. Štangar, V.M. Cristea, Z. Pap, K. Hernadi, L. Baia, Article optimization method of the solvothermal parameters using box–behnken

experimental design—the case study of zno structural and catalytic tailoring, Nanomaterials. 11 (2021). https://doi.org/10.3390/nano11051334.

[169] N. Justh, L.P. Bakos, K. Hernádi, G. Kiss, B. Réti, Z. Erdélyi, B. Parditka, I.M. Szilágyi, Photocatalytic hollow TiO2 and ZnO nanospheres prepared by atomic layer deposition, Sci. Rep. 7 (2017) 4337. https://doi.org/10.1038/s41598-017-04090-0.

[170] B. Réti, G.I. Kiss, T. Gyulavári, K. Baan, K. Magyari, K. Hernadi, Carbon sphere templates for TiO2 hollow structures: Preparation, characterization and photocatalytic activity, Catal. Today. 284 (2017) 160–168. https://doi.org/10.1016/j.cattod.2016.11.038.

[171] T. Gyulavári, K. Kovács, K. Magyari, K. Baán, A. Szabó, G. Veréb, Z. Pap, K. Hernadi, Unexpected Link between the Template Purification Solvent and the Structure of Titanium Dioxide Hollow Spheres, Catal. . 11 (2021). https://doi.org/10.3390/catal11010112.

[172] J. Yu, X. Yu, Hydrothermal Synthesis and Photocatalytic Activity of Zinc Oxide Hollow Spheres, 42 (2008) 4902–4907.

[173] Y. Zhang, E.W. Shi, Z.Z. Chen, B. Xiao, Fabrication of ZnO hollow nanospheres and "jingle bell" shaped nanospheres, Mater. Lett. 62 (2008) 1435–1437. https://doi.org/10.1016/j.matlet.2007.08.079.

[174] M. Rodr, S. Fern, I. Moggio, M. Silva, Hollow ZnO microspheres functionalized with electrochemical graphene oxide for the photodegradation of salicylic acid †, (2019) 6965–6972. https://doi.org/10.1039/c8ra10113b.

[175] Z. Bai, Y. Zhang, N. Fan, C. Guo, B. Tang, One-step synthesis of ZnO@C nanospheres and their enhanced performance for lithium-ion batteries, Mater. Lett. 119 (2014) 16–19. https://doi.org/10.1016/j.matlet.2013.12.060.

[176] S. Krishnamurthy, A. Esterle, N.C. Sharma, S. V. Sahi, Yucca-derived synthesis of gold nanomaterial and their catalytic potential, Nanoscale Res. Lett. 9 (2014) 1–9. https://doi.org/10.1186/1556-276X-9-627.

[177] M. Zhang, B. Zhou, K.T. Chuang, Catalytic deep oxidation of volatile organic compounds over fluorinated carbon supported platinum catalysts at low temperatures, Appl. Catal. B Environ. 13 (1997) 123–130. https://doi.org/10.1016/S0926-3373(96)00097-5.

[178] Z. Fu, J. He, J. Lu, Z. Fang, B. Wang, Investigation of dielectric relaxation and degradation behavior of two-step sintered ZnO varistors, Ceram. Int. 45 (2019)

21900–21909. https://doi.org/ 10.1016/j.ceramint.2019.07.201.

[179] A. Serrano, O. Caballero-Calero, M.Á. García, S. Lazić, N. Carmona, G.R. Castro, M. Martín-González, J.F. Fernández, Cold sintering process of ZnO ceramics: Effect of the nanoparticle/microparticle ratio, J. Eur. Ceram. Soc. 40 (2020) 5535–5542. https://doi.org/10.1016/j.jeurceramsoc.2020.05.059.

[180] T.K. Roy, D. Bhowmick, D. Sanyal, A. Chakrabarti, Sintering studies of nano-crystalline zinc oxide, Ceram. Int. 34 (2008) 81–87. https://doi.org/ 10.1016/j.ceramint.2006.08.015.

[181] B. Choudhury, A. Choudhury, Oxygen defect dependent variation of band gap, Urbach energy and luminescence property of anatase, anatase-rutile mixed phase and of rutile phases of TiO2 nanoparticles, Phys. E Low-Dimensional Syst. Nanostructures. 56 (2014) 364–371. https://doi.org/10.1016/j.physe.2013.10.014.

[182] A.B. Djurisic, Y. Leung, K. Tam, L. Ding, W. Ge, H.-Y. Chen, S. Gwo, Green, yellow, and orange defect emission from ZnO nanostructures: Influence of excitation wavelength, Appl. Phys. Lett. 88 (2006) 103107. https://doi.org/10.1063/1.2182096.

[183] A. Galdámez-Martinez, G. Santana, F. Güell, P.R. Martínez-Alanis, A. Dutt, Photoluminescence of zno nanowires: A review, Nanomaterials. 10 (2020). https://doi.org/10.3390/nano10050857.

[184] M. Zare, K. Namratha, S. Alghamdi, Y.H.E. Mohammad, A. Hezam, M. Zare, Q.A. Drmosh, K. Byrappa, B.N. Chandrashekar, S. Ramakrishna, X. Zhang, Novel Green Biomimetic Approach for Synthesis of ZnO-Ag Nanocomposite; Antimicrobial Activity against Food-borne Pathogen, Biocompatibility and Solar Photocatalysis, Sci. Rep. 9 (2019) 1–15. https://doi.org/10.1038/s41598-019-44309-w.

[185] M. aouicha Bouayed, N. Ameur, F. Taieb-Brahimi, T. Hidouri, S. Naser, H. Ghouas, S. Bedrane, B.M. Al-Shahri, R. Bachir, Investigation of novel titanate nanotubes modified with Ce, Fe, Zn and Zr for efficient dye degradation performance, inhibition of bacterial and fungal growth and anticorrosion activity in acid medium, React. Kinet. Mech. Catal. 134 (2021) 517–537. https://doi.org/10.1007/s11144-021-02068-8.

[186] C. Feng, Z. Chen, J. Jing, J. Hou, The photocatalytic phenol degradation mechanism of Ag-modified ZnO nanorods, J. Mater. Chem. C. 8 (2020) 3000–3009. https://doi.org/10.1039/c9tc05010h.

[187] S. Malato, J. Cáceres, A.R. Fernández-Alba, L. Piedra, M.D. Hernando, A. Agüera,

J. Vial, Photocatalytic Treatment of Diuron by Solar Photocatalysis: Evaluation of Main Intermediates and Toxicity, Environ. Sci. Technol. 37 (2003) 2516–2524. https://doi.org/10.1021/es0261170.

[188] Y. Wang, Y. Li, Z. Zhou, X. Zu, Y. Deng, Evolution of the zinc compound nanostructures in zinc acetate single-source solution, J. Nanoparticle Res. 13 (2011) 5193–5202. https://doi.org/10.1007/s11051-011-0504-y.

[189] A. Ismail, M.J. Abdullah, The structural and optical properties of ZnO thin films prepared at different RF sputtering power, J. King Saud Univ. - Sci. 25 (2013) 209–215. https://doi.org/10.1016/j.jksus.2012.12.004.

[190] F. Chowdhury, S.M. Firoz Hasan, M. Sahabul Alam, Morphological and optical properties of vacuum evaporated ZnO thin films, Turkish J. Phys. 36 (2012) 1–7. https://doi.org/10.3906/fiz-1104-6.
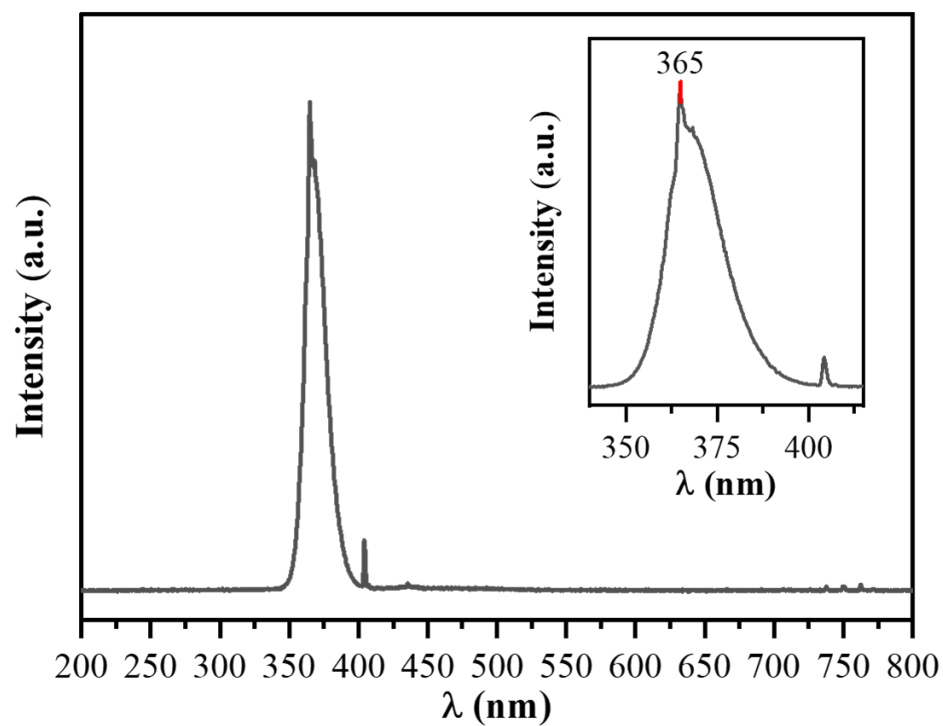
10. Appendix

Figure S1 Emission spectra of the used UV lamps with the inset of the wavelength region 350-425 nm.
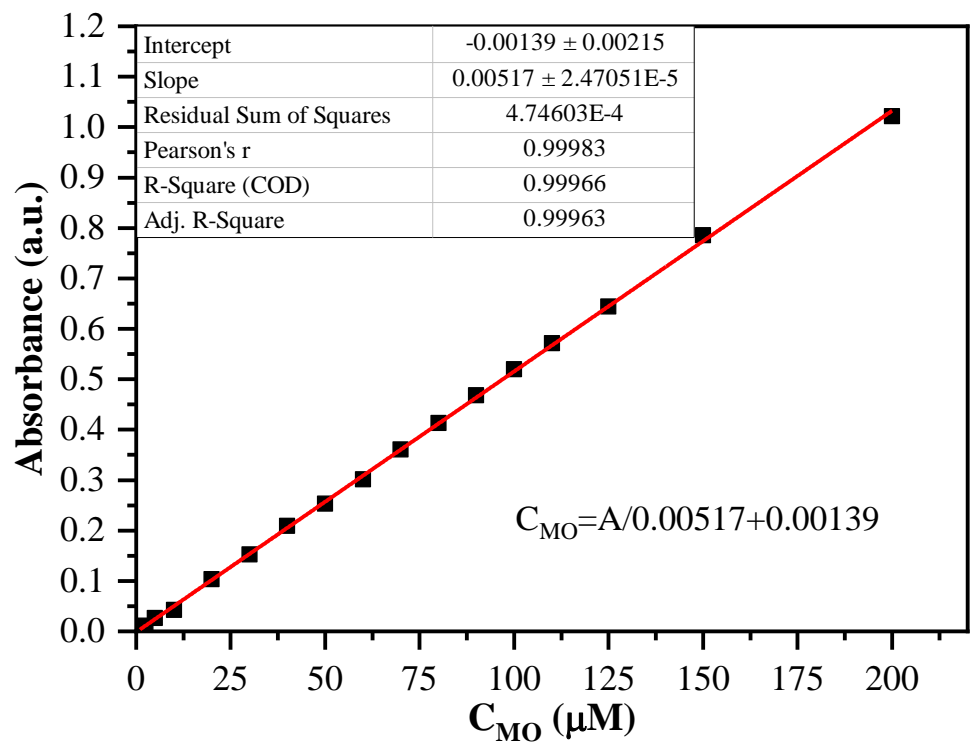
Figure S2 The calibration curve of methyl orange (MO) absorbance at 464 nm at different concentrations (1–200 µM) [120].
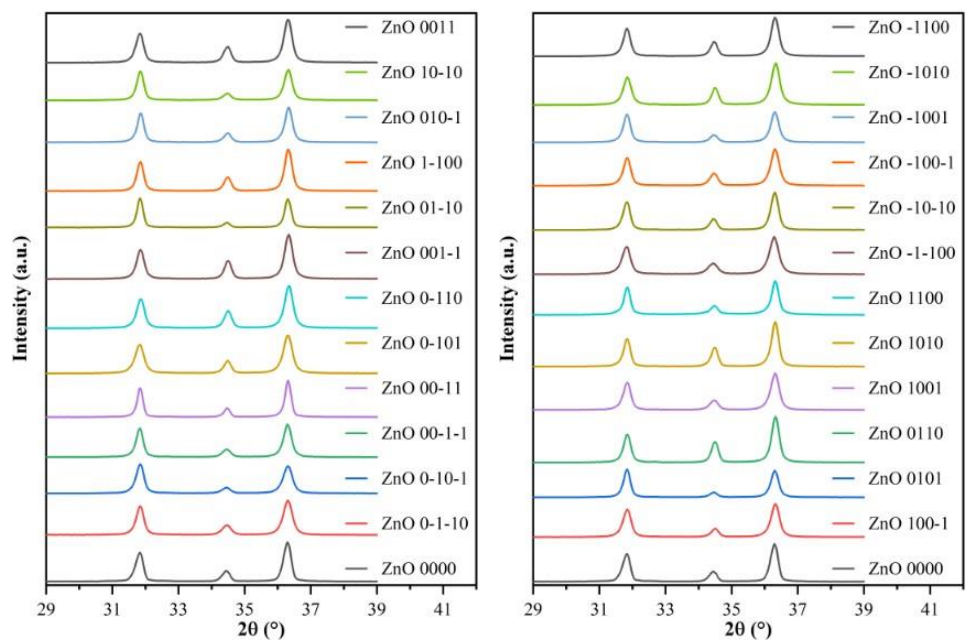

Figure S3 The X-ray diffractograms of all the synthesized samples according to the Box–Behnken This figure was taken from ref. [120].
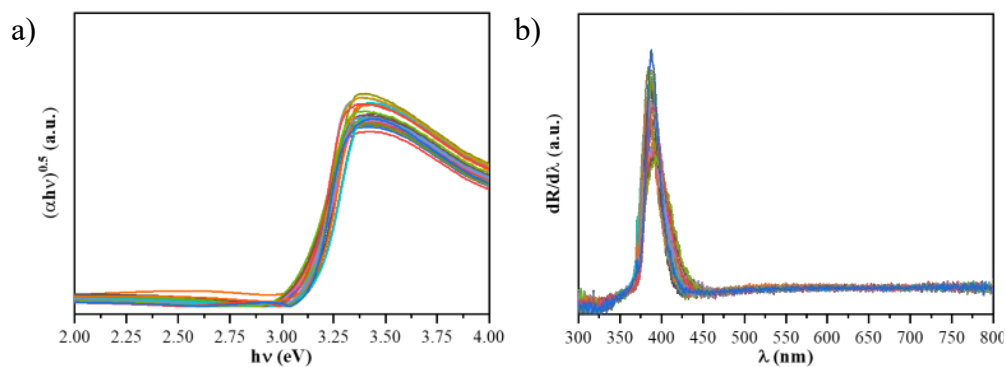
Figure S4 Tauc plot of the Kubelka-Munk transformations (a), respective the first derivative of diffuse reflectance spectra (b) of the ZnO samples prepared using BBD [120].

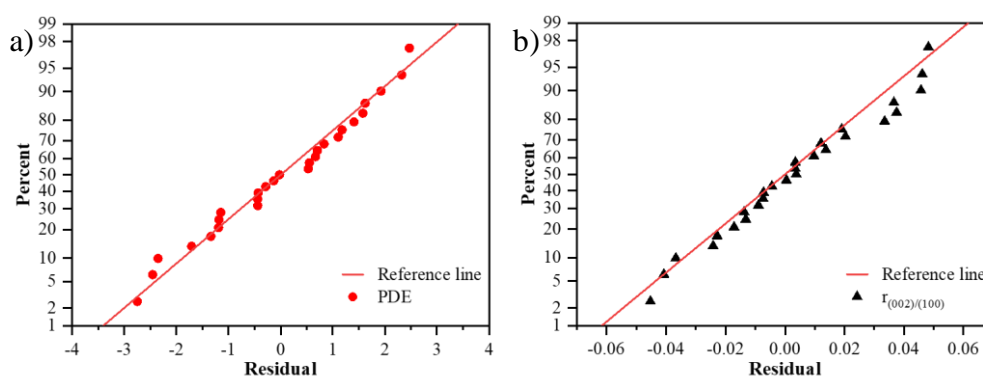**Figure S5 Normal probability plot of residuals: for PDE (a); for $r_{(002)/(100)}$ (b) [120].**
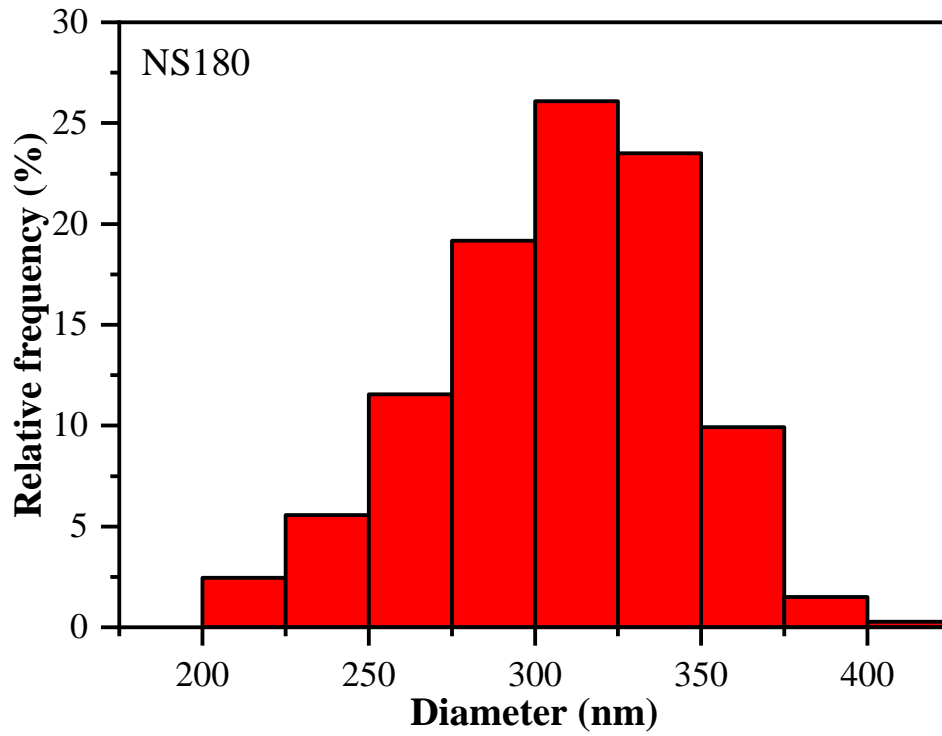
Figure S6 Diameter size distributions of the NS180 [125].
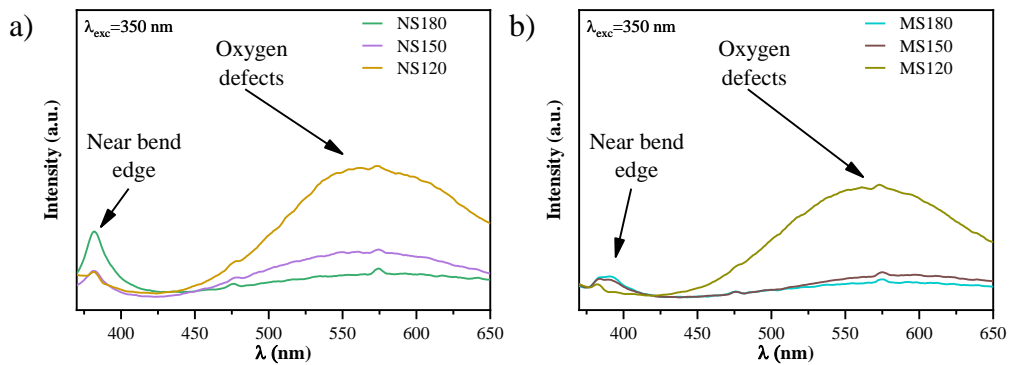
Figure S7 PL emission spectra of the samples prepared using pure ZnAA₂, respective ZnAc₂ at different synthesis temperatures, at 350 nm excitation wavelength. The near-bend edge and oxygen defect state emissions change according to the temperature [125].
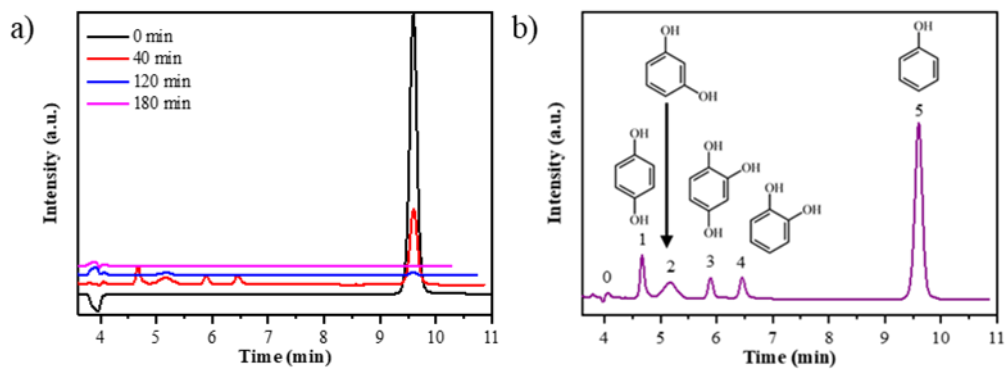
Figure S8 The chromatograms of the NS180 sample, during the degradation process of the phenol (a) and the identified intermediates at 40 min of the photodegradation tests (b) – 0 mark the eluent front, (1) hydroquinone, (2) resorcinol, (3) hydroxyquinol, (4) catechol and (5) phenol [125].
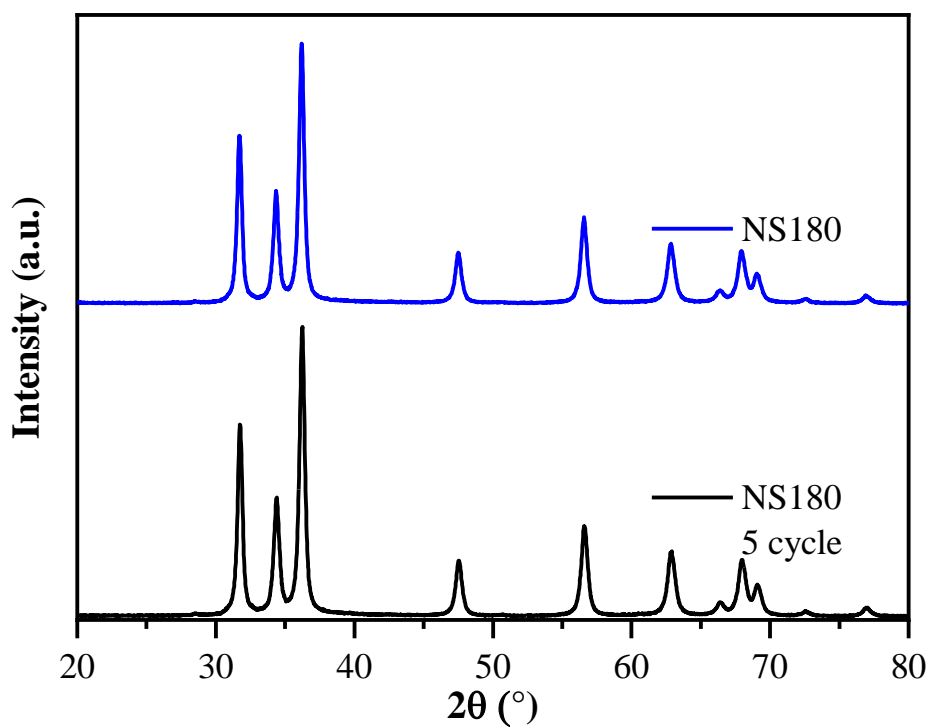
Figure S9 X-ray diffractograms of NS180 before and after 5 cycles of photodegradation test [125].
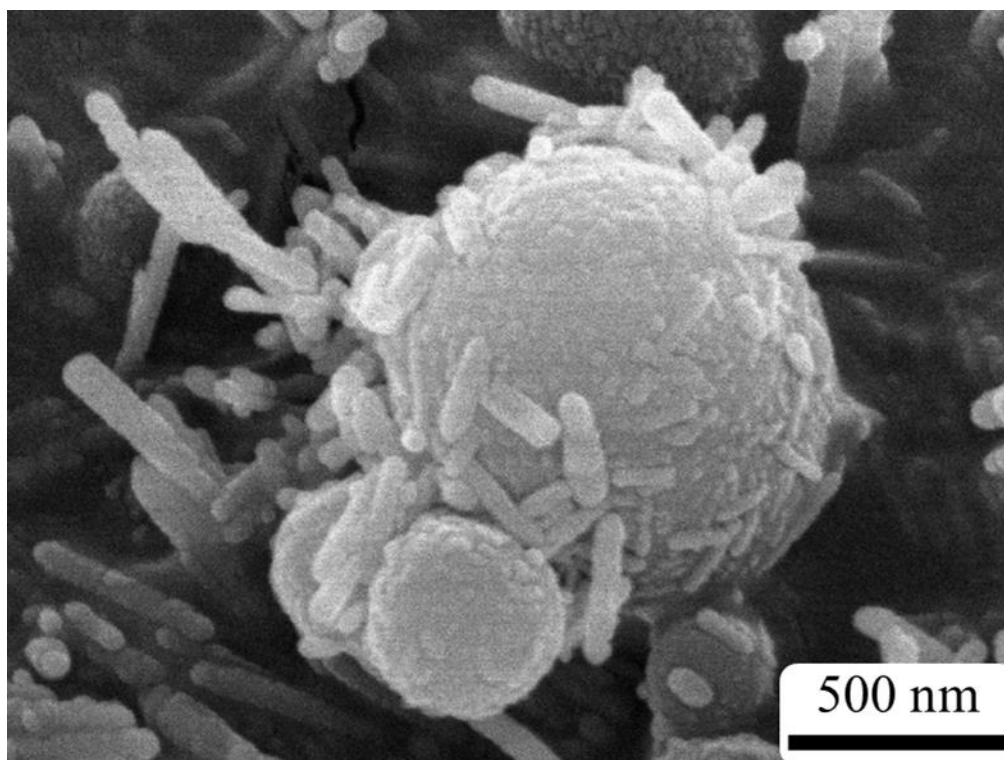
Figure S10 SEM micrograph of the sample synthesized with a solvothermal method using ZnAc$_2$ precursor. The small rod-like crystals are ZnO attached to carbon spheres [128].
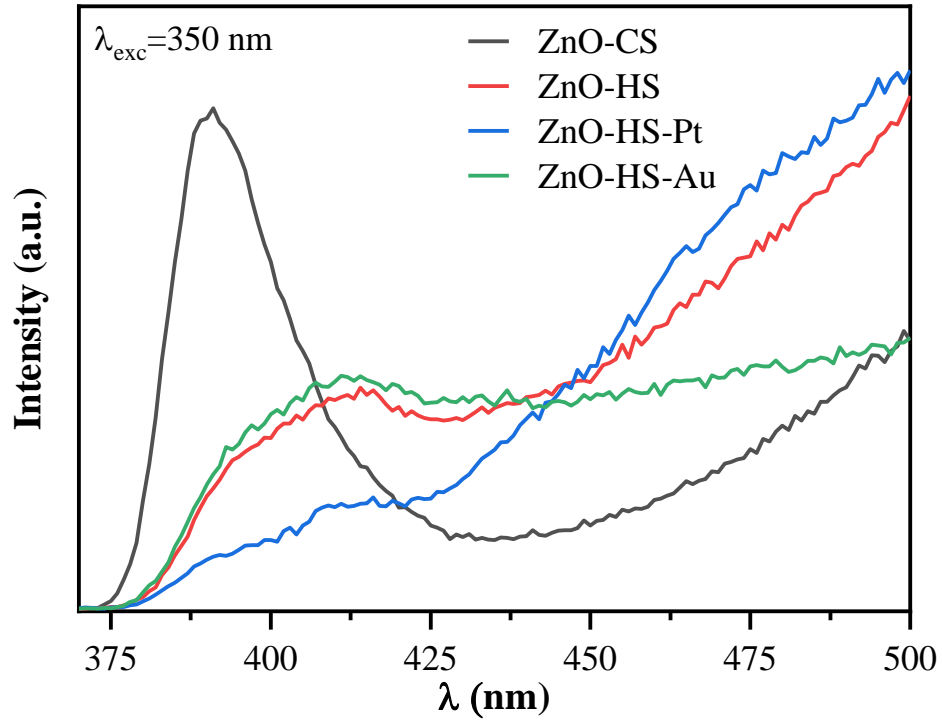
Figure S11 PL emission spectra of the as-prepared samples recorded at 350 nm excitation wavelength. ZnO-CS composite before calcination shows the specific intense near band edge emission at 391 nm, which is reduced in intensity after calcination and redshifted by noble metal deposition [128].

Figure S12 The XRD (a), SEM micrographs of before (b) and after phenol degradation experiments (d), respective the degradation curves of the three cycles (c) [128].

Table S1 ANOVA results for a quadratic model of ZnO using Box–Behnken design for photocatalytic measurements [120].

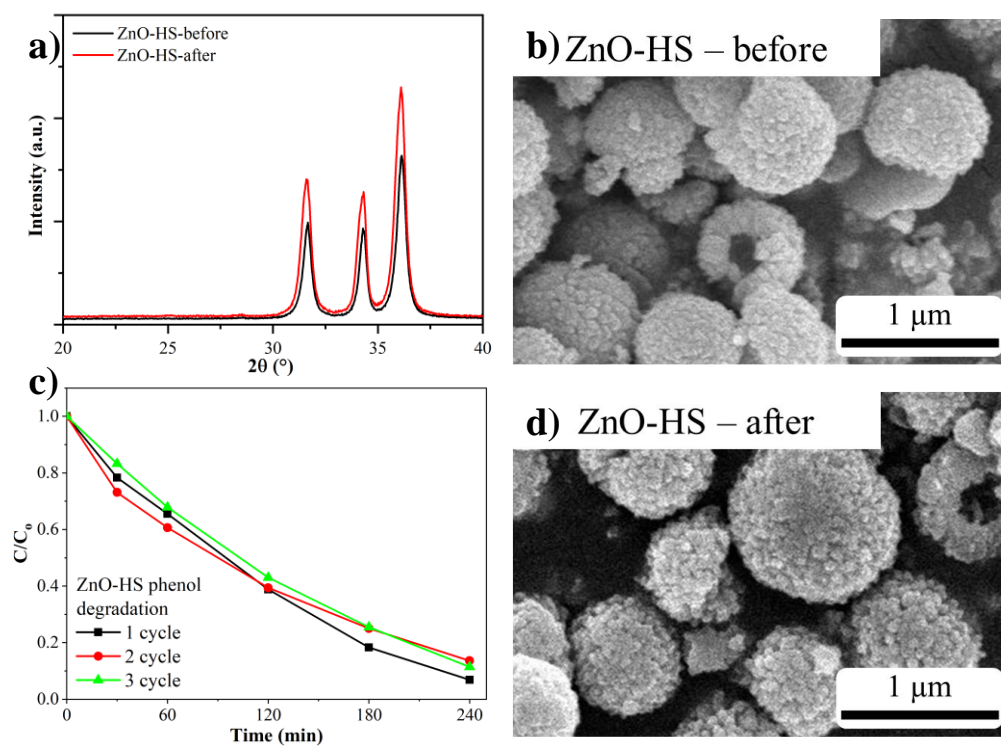| Analysis of Variance						
Source	**DF**	**Adj SS**	**Adj MS**	**F-Value**	**p-Value**	**VIF**
Model	14	6326.51	451.89	97.32	$<10^{-3}$*	
Linear	4	3443.08	860.77	185.37	$<10^{-3}$*	
X_1	1	55.04	55.04	11.85	$<10^{-3}$*	1
X_2	1	234.97	234.97	50.6	$<10^{-3}$*	1
X_3	1	3043.27	3043.27	655.37	$<10^{-3}$*	1
X_4	1	109.81	109.81	23.65	$<10^{-3}$*	1
Square	4	1657.47	414.37	89.23	$<10^{-3}$*	
X_1^2	1	1549.66	1549.66	333.72	$<10^{-3}$*	1.25
X_2^2	1	173.03	173.03	37.26	$<10^{-3}$*	1.25
X_3^2	1	134.45	134.45	28.95	$<10^{-3}$*	1.25
X_4^2	1	483.45	483.45	104.11	$<10^{-3}$*	1.25
2-Way Interaction	6	1225.96	204.33	44	$<10^{-3}$*	
X_1*X_2	1	46.92	46.92	10.1	$<10^{-3}$*	1
X_1*X_3	1	175.56	175.56	37.81	$<10^{-3}$*	1
X_1*X_4	1	29.7	29.7	6.4	$<10^{-3}$*	1
X_2*X_3	1	720.92	720.92	155.25	$<10^{-3}$*	1
X_2*X_4	1	46.92	46.92	10.1	$<10^{-3}$*	1
X_3*X_4	1	205.92	205.92	44.35	$<10^{-3}$*	1
Error	12	55.72	4.64		$<10^{-3}$*	
Lack-of-Fit	10	55.08	5.51	17.03	0.057**	
Pure Error	2	0.65	0.32			
Total	26	6382.23				

*significant ($p < 0.05$); **not significant; $\sigma = 1.83$, $R^2 = 0.9913$,

R^2(adj) = 0.9811, R^2(pred) = 0.9501.

Table S2 ANOVA results for a quadratic model of ZnO using Box–Behnken design for the ratio of intensities of X-ray diffraction peaks [120].

Analysis of Variance						
Source	**DF**	**Adj SS**	**Adj MS**	**F-Value**	**p-Value**	**VIF**
Model	14	0.693	0.050	32.5	$<10^{-3}$*	
Linear	4	0.557	0.139	91.31	$<10^{-3}$*	
X_1	1	0.001	0.001	0.38	0.551**	1
X_2	1	0.044	0.044	28.98	$<10^{-3}$*	1
X_3	1	0.506	0.506	331.72	$<10^{-3}$*	1
X_4	1	0.006	0.006	4.17	0.064**	1
Square	4	0.092	0.023	15.16	$<10^{-3}$*	
X_1^2	1	0.001	0.001	0.52	0.484**	1.25
X_2^2	1	0.009	0.009	5.98	$<10^{-3}$*	1.25
X_3^2	1	0.059	0.059	38.92	$<10^{-3}$*	1.25
X_4^2	1	0.006	0.006	4.09	0.066**	1.25
2-Way Interaction	6	0.044	0.007	4.85	$<10^{-3}$*	
X_1*X_2	1	0.010	0.010	6.56	$<10^{-3}$*	1
X_1*X_3	1	0.011	0.011	7.44	$<10^{-3}$*	1
X_1*X_4	1	0.014	0.014	9.45	$<10^{-3}$*	1
X_2*X_3	1	0.000	0.000	0.02	0.89**	1
X_2*X_4	1	0.000	0.000	0.01	0.91**	1
X_3*X_4	1	0.009	0.009	5.61	$<10^{-3}$*	1
Error	12	0.018	0.002		$<10^{-3}$*	
Lack-of-Fit	10	0.018	0.002	16.37	0.059**	
Pure Error	2	0.000	0.000			
Total	26	0.712				

*significant ($p < 0.05$); **not significant; $\sigma = 0.039$, $R^2 = 0.9743$,
$R^2(adj) = 0.9443$, $R^2(pred) = 0.8531$..

Table S3 Primary crystallite sizes calculated for the XRD peaks (100) and (002) of ZnOs by the Scherrer equation.

BBD sample code	Primary crystallite size (nm)		The ratio of crystallite sizes for (002) and (100)
	(100)	**(002)**	
ZnO 0000	30.24	30.09	1.00
ZnO 0-1-10	30.35	25.78	0.85
ZnO 0-10-1	29.63	28.21	0.95
ZnO 00-1-1	33.43	27.96	0.84
ZnO 00-11	40.50	39.46	0.97
ZnO 0-101	25.84	34.44	1.33
ZnO 0-110	29.12	31.86	1.09
ZnO 001-1	30.31	33.36	1.10
ZnO 01-10	38.15	34.62	0.91
ZnO 1-100	33.41	32.28	0.97
ZnO 010-1	35.00	32.41	0.93
ZnO 10-10	33.65	29.15	0.87
ZnO 0011	28.83	31.47	1.09
ZnO 100-1	28.29	31.87	1.13
ZnO 0101	34.16	30.24	0.89
ZnO 0110	31.60	33.94	1.07
ZnO 1001	29.97	27.56	0.92
ZnO 1010	33.71	34.67	1.03
ZnO 1100	35.94	30.27	0.84
ZnO -1-100	27.24	23.58	0.87
ZnO -10-10	31.66	32.97	1.04
ZnO -100-1	31.13	29.41	0.94

Table S4 The dissolved inorganic content of the Theodora® mineral water [128].

Ion	Concentration	
	mg·L^{-1}	mM
Na$^+$	32.0	1.4
K$^+$	10.0	0.3
Ca^{2+}	144.0	3.6
Mg^{2+}	34.4	1.4
F$^-$	1.4	0.1
SO$_4^{2-}$	144.0	1.5
HCO$_3^-$	487.0	8.0
Other inorganic ions	51.2	-